Electronic Transport Properties of Copper and Gold at Atomic Scale

Elektronische Transporteigenschaften von Kupfer und Gold auf atomarer Skala

To all lovely people in my life

Bibliographische Beschreibung

Referat

In der vorliegenden Arbeit werden die wesentlichen Faktoren, die die elektronischen Transporteigenschaften von Kontaktstrukturen atomarer Größe aus Kupfer bzw. Gold bestimmen, theoretisch untersucht. Untersuchungsgegenstand ist eine leitfähige Struktur zwischen zwei kristallinen Elektroden. Um Transportberechungen sowohl unter Gleichgewichts- als auch unter Nicht-Gleichgewichts-Bedingungen durchführen zu können, wird die Simulations-Software gDFTB, die auf dem Nicht-Gleichgewichts-Green-funktionenformalismus in Kombination mit der Dichtefunktional-Tight-Binding-Methode beruht, eingesetzt. Die elektronischen Eigenschaften der betrachteten atomaren Drähte werden nur sehr schwach von ihrer kristallinen Orientierung, ihrer Länge und der Elektrodenanordnung beeinflusst. Als effektivster geometrischer Faktor wurde der Leiterquerschnitt gefunden, weil dieser die Anzahl der Leitungskanäle bestimmt. Darüber hinaus werden die erhaltenen Leitfähigkeitsoszillationen und die linearen Strom-Spannungs-Kennlinien erklärt. Für eine detaillierte Analyse des Leitungsmechanismus werden bei den Ein-Atom-Kontakten aus Kupfer und Gold die Übertragungskanäle und ihre Aufspaltung in Atomorbitale betrachtet. Die präsentierten Ergebnisse bieten eine mögliche Erklärung für den Zusammenhang zwischen Leitfähigkeit und geometrischer Struktur. Die Resultate zeigen eine akzeptable Übereinstimmung mit den verfügbaren experimentellen und theoretischen Studien.

Stichworte

Abstract

The factors governing electronic transport properties of copper and gold atomic-size contacts are theoretically examined in the present work. A two-terminal conductor using crystalline electrodes is adopted. The non-equilibrium Green's function combined with the density functional tight-binding method is employed via gDFTB simulation tool to calculate the transport at both equilibrium and non-equilibrium conditions. The crystalline orientation, length, and arrangement of electrodes have very weak influence on the electronic characteristics of the considered atomic wires. The wire width is found to be the most effective geometric aspect determining the number of conduction channels. The obtained conductance oscillation and linear current-voltage curves are interpreted. To analyze the conduction mechanism in detail, the transmission channels and their decomposition to the atomic orbitals are calculated in copper and gold single point contacts. The presented results offer a possible explanation for the relation between conduction and geometric structure. Furthermore, the results are in good agreement with available experimental and theoretical studies.

Keywords

Acknowledgments

I owe my deepest gratitude to the following people:

- PROF. I. MERTIG, thesis referee, for the helpful discussion and her efficient comments which have had a remarkable influence on career of the present work.
- PROF. T. GESSNER, my supervisor, for believing in me and encouraging me, and for his important support throughout this work.
- DR. R. STREITER, for providing the great opportunity to spend my Ph.D. in Chemnitz University of Technology, for his great supports, expertise, kindness, and for all those are not possible to list here.
- DR. A. PECCHIA, the author of gDFTB, for the simulation tool, for his patience with me to answer my crazy questions, for the excellent advices, and for the welcome in Rome.
- PROF. S. E. SCHULZ and PROF. T. OTTO, for their favor and guidance.
- DR. R. ECKE, for her attempts in IRTG plans and for her kindness all the time.
- PROF. M. HIETSCHOLD, for the fruitful discussion on the conduction mechanism.
- PROF. A. DI CARLO, for introducing the calculation method.
- DR. T. NIEHAUS and DR. CH. KÖHLER, for providing the copper Slater-Koster parameters and the helpful discussions about DFTB method.
- DR. J. SCHUSTER, for reading the thesis and helpful discussions.
- DIPL.-PHYS. A. ZIENERT, for his great helps, fruitful discussions, and his favors.
- M.SC. K. MALEKIAN, for his helps to edit this work and for his kindness, him as well as DR. P. BELSKY.
- PROF. R. LIU, for his supports during the scholar in Fudan University in Shanghai; and M.SC. ZH. ZONG., for her welcome in China and for her attempts in the joint paper.
- My dear colleagues and friends, S. ROTTAU, S. LANGOS, K. TRÄBER, DR. H. WOLF, DR. M. VOGEL, A. MESSIG, DR. J. MARTIN, I. STREITER, J. GRUNERT, R. LUTNYK, DR. K. SCHULZE, DR. T. WÄCHTLER, J. HOMMEL, DR. N. NEMEC, and B. YEN, for their great kindness.
- My parents and my sister, for their endless love.

List of Commonly Used Abbreviations and Symbols

Commonly used abbreviations

Abbreviation	Meaning
DFTB	Density functional tight-binding
GEA	Gradient expansion approximation
GGA	General gradient approximation
HRTEM	High resolution transmission electron microscopy
IETS	Inelastic electron tunneling spectroscopy
KKB	Keldysh-Kadanoff-Baym model
LCAO	Linear combination of atomic orbitals
LDA	Local density approximation
MCBJ	Mechanically controllable break junctions
NEGF	Non-equilibrium Green's function method
PL	Principle layer
STM	Scanning tunneling microscopy
TB	Tight-binding model
TEM	Transmission electron microscopy
2DEG	Two-dimensional electron gas

Commonly used symbols

Symbol	Meaning
δn	Electronic density deviation
Δq	Deviation of the atomic charge from the neutral atom
ε	Energy of a free electron
λ_F	Fermi wavelength
μ_α	Chemical potential of the electrode α
ρ	Density operator
σ	Conductivity
$\Sigma^<$	Electrons in-scattering function (lesser self-energy)
$\Sigma^>$	Holes in-scattering function
Σ_α^a	Advanced self-energy
Σ_α^r	Retarded self-energy
τ	Relaxation time
τ_{el}	Collision time
τ_φ	Phase relaxation time
Υ	Nuclear part of system wave funtion
ϕ_i	Atomic orbitals localized around the atomic center
Φ	Many-body system wave function
ψ_i	Scattering states
Ψ	Electronic part of system wave function
D	Total density operator
D_α	Partial density operator of the contact α
e	Electron charge
E	System eigenvalue
E_{XC}	Exchange and correlation energy
f_α	Fermi distribution function of the electrode α
$F_{00}^i(\mathbf{r})$	Spherical s-like radial function
$g(\varepsilon)$	System density of states
g_α	Green's function of the Hamiltonian of the contact α
G	Conductance
G_0	Quantum conductance
$\mathcal{G}$	Green's function
$\mathcal{G}^<$	Green's function related to the density of occupied states
$\mathcal{G}^>$	Green's function related to the density of empty states
$\mathcal{G}^a$	Advanced Green's function
$\mathcal{G}^r$	Retarded Green's function

Symbol	Meaning
h	Planck's constant ($4.13566733 \times 10^{-15}$ eV s)
$\mathcal{H}$	Time-independent Hamiltonian operator
$\mathcal{H}_\alpha$	Hamiltonian of the contact α
$\mathcal{H}_D$	Hamiltonian of the device region
$\mathcal{H}^0$	Two-center TB Hamiltonian
I_S	Surface current
$\mathcal{J}_{nn'}$	Current flowing from the site n into the site n'
$\mathcal{J}_S$	Total electron current through the surface S
k_F	Fermi wave number
ℓ_{el}	Elastic mean free path
ℓ_φ	Phase coherence length
ℓ_ξ	Localization length
$\mathbf{L}$	System dimensions (L_x, L_y, L_z)
$n(\mathbf{r})$	Electron density
n^0	Reference electronic density
R	Reflection coefficient
R_c	Contact resistance
T	Transmission coefficient
T_s	Kohn-Sham kinetic energy
U_H	Classical electrostatic interaction energy (Hartree energy)
v_{eff}	Kohn-Sham potential
v_F	Fermi velocity
$\mathcal{V}$	Hamiltonian coupling the device region to the contacts
V_b	Bias voltage
V^0	Effective potential corresponding to the reference charge density

Contents

Inhaltsverzeichnis

14

Chapter 1.

Introduction

1.1. Background and motivation

The investigation of electron transport as a fundamental issue to describe the electronic devices demands further extentions for structures and systems with dimensions from tens of nano meters to the atomic scale introduced by nanotechnology. The conventional treatment of transport properties is based on the *Boltzmann equation* for electrons and other particles in ordinary metals and insulators [1]. The Boltzmann transport equation describes macroscopic phenomena, such as electrical conductivity, *Hall effect*, and diffusion processes using approximations and phenomenological approaches.

The basic principles of classical Boltzmann theory are not conserved when the scale of electronic devices approaches to dimensions comparable to the electron mean free path, in which the *size effects* come essentially into play [2]. In order to overcome deficiencies of the classical theory, the *relaxation time approximation* was proposed, leading to the *semi-classical transport approach* [3].

Despite the impressive successes of the semi-classical theory in delineating the electronic properties of conductors (e.g., in thin films and nanowires), modern transport techniques capture more of the microscopic picture including the *quantum nature* of the problem. The continuous scaling of microelectronics down to the atomic level introduces new intricacies and invites a rapidly growing interest in both experimental and theoretical study of the properties of atomic-sized contacts.

Atomic-scaled contacts have dimensions comparable with the Fermi wavelength and smaller than the elastic mean free path, so that they are classified in the *quantum ballistic transport regime*, and the *Landauer theory* is allocated to describe the quantum effects participated in the electron transport [4].

In this regard, metallic atomic-sized nanocontacts have attracted great attention due to the novel physical properties, such as quantized conductance and localization effects, leading to the investigations in quantum physics as well as in nanotechnology. Among

metals, copper is of particular interest because of its important role due to low electrical resistivity and high resistance to the electromigration. Compared with the wide application of copper in electronics and electrical engineering, only less effort has been put into research to explore the properties at atomic scale. In particular, the use for interconnects and functional layers with dimensions of a few nanometers in high speed integrated circuits has prompted to choose atomic-sized copper wires for examination. Rather availability of experimental data for gold atomic contacts has been a motivation to use gold as a reference to compare against copper.

Recent advances in experimental techniques, such as *scanning tunneling microscopy* (STM) [5, 6], *mechanically controllable break junctions* (MCBJ) [7–9], and *transmission electron microscopy* (TEM) [10–12], have given rise to fabricate wires at the atomic scale (i.e., short chains of atoms that conduct electricity between two electrodes).

Recently, Rodrigues et al. [11] generated gold nanowires on the atomic scale at room temperature observing defect-free and crystalline structures, which adopted three configurations: [100], [110], and [111]. Furthermore, the existence of pentagonal copper atomic wires, has been reported by Gonzáles et al. [13], confirming three possible atomic configurations, in which [100] and [111] are able to form the smallest neck as a bipyramidal contact. The [110] atomic wires are found to be rather brittle (i.e., they break when they are two- to three-atom-thick without forming atomic contacts).

The geometric structures are modeled based upon the experimental observations proposing rod-like atomic wires along the [100] and [110] directions, and the bipyramidal contacts are connected to the cognate [100] and [111] electrodes.

A fundamental question to be addressed in the present work is how the geometric structure governs the electronic transport properties in copper and gold atomic contacts. For this purpose, the role of each geometric characteristic is analyzed individually. In this respect, the total transmission coefficient (i.e., probability of transmitting electrons along the contact) is calculated as a function of both incident electron energy and applied bias voltage.

Based on transmission coefficients and using the Landauer formalism, the conductance and current-voltage characteristics are calculated. An extensive electron transport study, which can provide fundamental information for engineering small electronic devices, is done by considering the *single atom contacts*. According to the *scattering approach*, the electronic transport in these mesoscopic structures can be described in terms of independent conducting channels characterized by certain transmission coefficients varying between zero and one [14]. To completely characterize their transport properties, the individual channel transmissions, which are useful to interpret the conduction results, are calculated.

The formation of one-atom-thick copper and gold wires at low temperatures has been reported recently using MCBJ techniques [8, 15, 16]. In determining the transmission

channels for the first time, SCHEER et al. [17] confirmed that the conductance channel concept was not a theoretical abstract.

Present results including the conductance and linear current-voltage characteristics of copper and gold single point contacts fit well with the available experimental data and some theoretical studies [18–20]. More importantly, current study offers possible explanations for experimental observations, which are looking for factors governing the electron transport properties in copper and gold atomic-scale contacts.

1.2. Overview of methodology

Electrons in a solid exhibit quantum mechanical behavior. Solving the *Schrödinger equation* via the *many body wave function* is the traditional method used to key out electrons motion. *Density functional theory* based on the *Kohn-Sham* formalism is a known alternative solution to the Schrödinger equation [21–25], and adequate approximations (e.g., the *exchange-correlation* function can be constructed via the *local density approximation* [25]) are used to simplify the problem.

The standard density functional theory has fundamental limitations for applications in mesoscopic electronics. To overcome this problem, the *density functional tight-binding method* is suggested as a model proven to give a successful description of electron transport in metal atomic contacts [26–29]. With a system of atomic dimensions, it is natural to choose the atomic orbital basis in designing the tight-binding model. Furthermore, combination of the density functional tight-binding model with the *Green's function* technique provides an efficient way to obtain transport properties in terms of microscopic parameters [14, 30, 31]. The generalization to a more advanced theory, able to describe systems driven out of equilibrium by an applied bias voltage, is accommodated using the *non-equilibrium Green's function method* (NEGF method) [32–35]. This generalization distinguishes method employed in the present work from more simple transport calculations.

The gDFTB code, as an efficient simulation tool implementing the non-equilibrium Green's function density functional tight-binding method, is exploited [36]. To produce results within a reasonable time, a semi-empirical method is required to handle the large number of electrons in metal atomic-scale contacts. gDFTB therefore employs the empirical tight-binding model (i.e., based on the empirical *Slater-Koster* parameterization [37]) and uses an operative block-iterative algorithm to speed up computations, solving the *self-consistent* transport problem by assuming local *Dirichlet boundary conditions*. This approach has been tested widely for various organic and inorganic molecular-scale devices (e.g., CNTs [38], silicon nanowires [39], and molecular wires [36]) and is a suitable candidate for purposes of the present thesis.

1.3. Thesis outline

Chap. 2: Analytical Theory of Electronic Transport   A brief introduction to electron transport theory in materials ranging from macroscopic to mesoscopic scales is presented. This includes classical, semi-classical, and quantum mechanical approaches. The comparison of mesoscopic characteristic length scales leads to the electronic transport classification. The Landauer formalism is discussed to analytically derive the conductance based on the transmission eigenchannels in the ballistic transport regime.

Chap. 3: Electronic Transport Calculations   The method used in the present study for handling electrons in transport problem is introduced generally, including an overview of the tight-binding model moving towards the density functional theory in combination with the non-equilibrium Green's function formalism.

Chap. 4: gDFTB: A Tool for the NEGF Density Functional Tight-Binding Formalism   An efficient simulation tool for implementing the proposed method is described. The distinguishing features of the gDFTB tool are introduced. Based on the gDFTB, the energy band structure calculations for bulk copper compared to the experimental and theoretical studies are presented as a test case.

Chap. 5: Electronic Transport Properties of Metal Atomic Wires   The concept of atomic wire, formation techniques, and modeled geometries are presented. The effect of each characteristic, including orientation, length, width, non-mirrored electrodes, and temperature on electron transport is analyzed independently for copper and gold atomic wires at both equilibrium and external bias voltage conditions. An explanation is presented to indicate the oscillation of conductance with respect to the wire length. The non-linearity of current-voltage curves is interpreted, based on the charge neutrality. Furthermore, results are compared with those of available experimental and other theoretical investigations.

Chap. 6: Electron Transport in Single Point Contacts   Detailed information regarding modeled single point contacts is given. The transmission decomposition to the conduction channels and the contribution of each orbital in the conductance are examined. The conductance and current-voltage characteristics of copper and gold single point contacts of cognate [001] and [111] electrodes at liquid helium temperature are represented, including comparisons with previous experimental and theoretical approaches.

Chap. 7: Conclusions and Perspectives   Conclusions and perspectives on the whole thesis are presented, as well as some suggestions for the future works.

Einführung

Hintergrund und Motivation

Die Entwicklung der Nanotechnologie erfordert eine Ausdehnung der Untersuchung des Elektronentransports als Grundlage für die Beschreibung elektronischer Bauelemente auf Strukturen und Systeme mit Abmessungen von einigen zehn Nanometern bis hin zu atomaren Dimensionen. Die herkömmliche Behandlung von Transporteigenschaften in Metallen und Isolatoren basiert auf der Boltzmann-Gleichung für Elektronen und andere Teilchen [1]. Die *Boltzmann-Gleichung* beschreibt makroskopische Phänomene wie die elektrische Leitfähigkeit, den *Hall-Effekt* und Diffusionsprozesse unter Verwendung von Näherungen und phänomenologischen Ansätzen.

Die grundlegenden Prinzipien der klassischen Boltzmann-Theorie gelten nicht mehr, wenn die typischen Abmessungen elektronischer Bauelemente vergleichbar werden mit der mittleren freien Weglänge der Elektronen und der sogenannte *Size Effect* eine wesentliche Rolle zu spielen beginnt [2]. Um die Einschränkungen der klassischen Theorie zu überwinden wurde die *Relaxationszeit-Näherung* vorgeschlagen, die auf den *semiklassischen Transportansatz* führt [3].

Trotz des Erfolgs der semiklassischen Theorie bei der Beschreibung der elektronischen Eigenschaften von elektrischen Leitern (z. B. dünnen Filmen und Nanodrähten) fokussieren moderne, den Transport beschreibende Methoden mehr auf mikroskopische Vorstellungen einschließlich der Berücksichtigung der *Quanten-Natur* des Problems. Die kontinuierliche Skalierung in der Mikroelektronik bis auf atomare Ebene bringt neue Herausforderungen mit sich und führt zu einem schnell wachsenden Interesse sowohl an experimentellen als auch an theoretischen Untersuchungen der Eigenschaften von Kontaktstrukturen atomarer Größe.

Die Abmessungen atomarer Kontakte sind vergleichbar mit der Fermi-Wellenlänge und kleiner als die elastische mittlere freie Weglänge. Deshalb werden diese dem *quantenballistischen Transportregime* zugeordnet, welches durch die *Landauer Theorie* beschrieben wird, die Quanteneffekte beim Elektronentransport berücksichtigt [4].

Auf Grund von neu entdeckten physikalischen Phänomenen wie der quantisierten Leitfähigkeit und Lokalisierungseffekten haben atomare metallische Nanokontakte viel

Aufmerksamkeit auf sich gezogen, die zu Untersuchungen sowohl in der Quantenphysik als auch in der Nanotechnologie führten. Unter den Metallen ist Kupfer wegen seiner Rolle in der Elektronikindustrie auf Grund seines niedrigen elektrischen Widerstandes und seiner Elektromigrationsfestigkeit von besonderem Interesse. Verglichen mit der breiten Anwendung von Kupfer in der Elektronik wurde bisher wenig Forschungsaufwand getrieben, um die Eigenschaften auf atomarer Skala zu untersuchen. Insbesondere die Verwendung für Leitbahnen und als wenige Nanometer dünne Funktionsschichten in schnellen integrierten Schaltkreisen war Anlass, Kupferdrähte mit atomaren Abmessungen zu untersuchen. Umfangreiche experimentelle Daten von atomaren Goldkontakten waren hingegen Motivation, Gold zum Vergleich mit Kupfer als Referenz zu nutzen.

Die jüngsten Fortschritte bei experimentellen Techniken, wie der *Rastertunnelmikroskopie* (STM) [5, 6], *mechanisch kontrollierbaren Abrissübergängen* (MCBJ) [7–9], und der *Transmissionselektronenmikroskopie* (TEM) [10–12], haben dazu beigetragen, Drähte in atomarem Maßstab herzustellen (d. h. kurze Ketten von Atomen, die die Elektrizität zwischen zwei Elektroden leiten).

Rodrigues et al. [11] erzeugten kürzlich Gold-Nanodrähte im atomaren Maßstab bei Raumtemperatur und beobachteten dabei defektfreie kristalline Strukturen, die drei Kristallorientierungen angenommen hatten: [100], [110] und [111]. Darüber hinaus wurde von Gonzáles et al. [13] über die Existenz von pentagonal kristallisierten atomaren Kupferdrähten berichtet, womit die drei möglichen atomaren Konfigurationen bestätigt wurden, von denen die [100]- und die [111]-Konfigurationen in der Lage waren, den schmalsten Ansatz als bi-Pyramidenkontakt zu bilden. Die [110]-Drähte erwiesen sich als eher spröde. Sie brechen bei einer Dicke von zwei bis drei Atomlagen ohne die Bildung von atomaren Kontakten.

Die geometrischen Strukturen wurden basierend auf experimentellen Beobachtungen modelliert, die stäbchenförmige atomare Drähte entlang der [100]- und [110]-Richtungen nahe legen. Die bi-pyramidalen Kontakte sind dabei mit den entsprechenden [100]- bzw. [111]-Elektroden verbunden.

Eine grundlegende Frage, die in der vorliegenden Arbeit angesprochen werden soll, ist wie die geometrische Struktur die elektronischen Transporteigenschaften in atomaren Kupfer- und Goldkontakten beeinflusst. Zu diesem Zweck wird die Rolle aller geometrischen Merkmale analysiert. Hierfür wird der totale Transmissionskoeffizient (d. h. die Wahrscheinlichkeit der Übertragung von Elektronen über den Kontakt) als eine Funktion der Energie der einfallenden Elektronen und der angelegten Bias-Spannung berechnet für verschiedene Geometrien.

Auf der Grundlage der Transmissionskoeffizienten und unter Verwendung des Landauer-Formalismus werden Leitfähigkeit und Strom-Spannungs-Kennlinien bestimmt. Eine umfassende Studie zum Elektronentransport in *Ein-Atom-Kontakten*, die grundlegende Informationen für Entwicklung kleinster elektronischer Bauelemente

liefern kann, wurde durchgeführt. Entsprechend dem *Streuungsansatz* kann der elektronische Transport in solchen mesoskopischen Strukturen mit Hilfe von unabhängigen Leitungskanälen mit bestimmten Transmissionskoeffizienten, die Werte zwischen Null und Eins annehmen können, beschrieben werden. Zur vollständigen Charakterisierung ihrer Transporteigenschaften, werden die einzelnen Transmissionen in den Kanälen, die zur Interpretation nützlich sind, berechnet.

Kürzlich wurde die Herstellung von ein Atom dicken Kupfer- und Golddrähten bei niedrigen Temperaturen unter Verwendung der MCBJ-Technik vorgestellt [8, 15, 16]. Bei der erstmaligen Bestimmung der Transmissionskanäle bestätigten Scheer et al. [17], dass das Konzept der Leitfähigkeitskanäle nicht nur eine abstrakte Theorie ist, sondern dass diese auch experimentell beobachtet werden können.

Die vorliegenden Ergebnisse einschließlich der Leitfähigkeit und der linearen Strom-Spannungs-Kennlinien von Kupfer- und Gold-Ein-Atom-Kontakten passen gut zu den vorhandenen experimentellen Daten und einigen theoretischen Studien [18–20]. Weiterhin gibt die vorliegende Arbeit mögliche Erklärungen für experimentelle Beobachtungen, die bei der Untersuchung von Transport-eigenschaften von Elektronen in Kupfer- und Gold-Kontakten gemacht wurden.

Übersicht der Methodik

Elektronen im Festkörper zeigen quantenmechanisches Verhalten. Die Lösung der *Schrödinger-Gleichung* über die Vielteilchen-Wellenfunktion ist die traditionelle Methode, um die Elektronendynamik zu bestimmen. Die *Dichtefunktionaltheorie* basierend auf dem *Kohn-Sham-Formalismus* ist eine bekannte alternative Lösung der Schrödinger-Gleichung [21–25] und adäquate Näherungen werden zur Vereinfachung des Problems verwendet. So kann zum Beispiel die *Austausch-Korrelations-Funktion* über die lokale Dichtenäherung konstruiert werden [25]).

Die Standard-Dichtefunktionaltheorie besitzt grundsätzliche Einschränkungen hinsichtlich ihrer Anwendung in der mesoskopischen Elektronik. Um dieses Problem zu überwinden, wird die *Dichtefunktional-Tight-Binding-Methode* zur Beschreibung des Elektronentransports in atomaren Metallkontakten vorgeschlagen [26–29]. Bei einem System mit atomaren Dimensionen ist es sinnvoll, die atomare Orbitalbasis zur Entwicklung des Tight-Binding Models zu verwenden. Darüber hinaus verschafft die Kombination des Dichtefunktional-Tight-Binding Modells mit der *Green-Funktionen-Technik* einen effektiven Weg, um Transporteigenschaften in Form von mikroskopischen Parametern zu erhalten [14, 30, 31]. Die Verallgemeinerung zu einer verbesserten Theorie, die auch in der Lage ist, Systeme zu beschreiben, die durch eine angelegte Bias-Spannung aus dem Gleichgewicht gebracht wurden, wird mittels der

NichtGleichgewichts-Green-Funktionen-Methode (NEGF-Methode) realisiert [32–35]. Diese Verallgemeinerung unterscheidet die in der vorliegenden Arbeit angewandten Methoden von einfacheren Transportberechnungen.

Der hier genutzte gDFTB-Code ist ein effizientes Simulations-Werkzeug und implementiert die Nicht-Gleichgewichts-Green-Funktionen Dichtefunktional-Tight-Binding-Methode [36]. Um in vernünftigen Zeiträumen zu Ergebnissen zu gelangen und um die große Zahl von Elektronen in atomaren Metallkontakten behandeln zu können, ist eine solche semi-empirische Methode nötig. gDFTB nutzt deshalb das empirische Tight-Binding-Modell auf Grundlage empirischen *Slater-Koster* Parametrierung [37] und einen operativen Blockiterationsalgorithmus zur Beschleunigung der Lösung des *selbstkonsistenten* Transportproblems mit *Dirichlet-Randbedingungen*. Diese Näherung wurde umfassend bei verschiedenen organischen und anorganischen molekularen Objekten (z. B. CNTs [38], Silizium-Nanodrähten [39] und Moleculardrähten [36] getestet und ist für die Zwecke in der vorliegenden Arbeit geeignet.

Gliederung der Arbeit

Kap. 2: Analytische Theorie des elektronischen Transports Es wird eine kurze Einführung in die Elektronen-Transport-Theorie in Materialien von der makroskopischen bis zur mesoskopischen Skala gegeben. Dies umfasst klassische, semiklassische und quantenmechanische Ansätze. Der Vergleich der charakteristischen mesoskopischen Längenskalen führt auf die Klassifikation des elektronischen Transports. Der Landauer Formalismus wird diskutiert, um die Leitfähigkeit im ballistischen Transport-Regime analytisch auf Basis von Transmissions-Eigenkanälen abzuleiten.

Kap. 3: Berechnungen des elektronischen Transports In diesem Kapital wird die der vorliegenden Studie zugrunde liegende Methode zur Behandlung von Elektronen in Transportproblemen vorgestellt. Eingeschlossen ist ein Überblick über das Tight-Binding-Modell. Die Dichtefunktionaltheorie wird in Kombination mit dem Nicht-Gleichgewichts-Green-Funktionen-Formalismus entwickelt.

Kap. 4: gDFTB: Eine Software für den NEGF Dichtefunktional-Tight-Binding-Formalismus Die gDFTB-Software wird als effizientes Simulationswerkzeug für die Umsetzung der vorgeschlagenen Methode beschrieben und deren. Besonderheiten vorgestellt. Die mittels gDFTB-basierten Bandstrukturberechnungen für Bulk-Kupfer sind im Vergleich zu experimentellen und theoretischen Untersuchungen als Testfall dargestellt.

Kap. 5: Elektronische Transporteigenschaften atomarer Metalldrähte Das Konzept atomarer Drähte, experimentelle Techniken zu deren Herstellung sowie die

modellierten Geometrien werden vorgestellt. Der Einfluss aller geometrischen Parameter, einschließlich der Orientierung, der Länge, der Breite, die Rolle nicht spiegelsymmetrischer Elektroden sowie der Temperatur auf den elektronischen Transport wird für atomare Kupfer-und Golddrähte unter Gleichgewichtsbedingungen wie auch unter externer Bias-Spannung analysiert. Eine Erklärung für die Leitfähigkeitsoszillationen in Abhängigkeit von der Drahtlänge wird gegeben. Die Nichtlinearität der Strom-Spannungs-Kurven, die auf der Ladungsneutralität beruht, wird im Rahmen der verwendeten Methode interpretiert. Darüber hinaus werden die Ergebnisse mit verfügbaren experimentellen Daten und mit den Ergebnissen anderer theoretischer Untersuchungen verglichen.

Kap. 6: Elektronischer Transport in Ein-Atom-Kontakten Zunächst werden detaillierte Informationen über die modellierten Ein-Atom-Kontakte gegeben. Die Aufspaltung der Transmission in Leitungskanäle und der Beitrag der einzelnen Orbitale zur Leitfähigkeit werden untersucht. Die Leitfähigkeit und das Strom-Spannungs-Verhalten von Kupfer- und Gold-Ein-Atom-Kontakten der entsprechenden [001] und [111] Elektroden bei der Temperatur von flüssigem Helium werden vorgestellt und Vergleiche mit früheren experimentellen und theoretischen Ergebnissen verglichen.

Kap. 7: Schlussfolgerungen und Perspektiven Es werden Schlussfolgerungen und Perspektiven der vorliegenden Schrift präsentiert sowie Vorschläge für künftige Arbeiten unterbreitet.

Chapter 2.

Analytical Theory of Electronic Transport

2.1. Introduction

This chapter presents briefly the theory of electronic transport from macroscopic to the mesoscopic range. As device dimensions are shrinking down, the *classical Boltzmann transport theory* is not able to interpret physical phenomena rising from the *size effect*. Thus, it is generalized to the semi-classical theory through the adequate approximations.

In spite of successes of the semi-classical approach in describing size effects of mesoscopic devices, its defects in molecular-range, where the *quantum mechanics* comes out, are not negligible. Therefore, a clear classification of corresponding transport for different device scales is essential.

Samples of interest in this work are categorized in the ballistic transport regime. Hence, the *Landauer-Büttiker* formalism is employed to explain ballistic transport at atomic-scale structures for two-terminal one- and three-dimensional cases, assuming low temperatures and low applied voltages in the absence of magnetic fields and temperature gradients.

The present chapter is organized as follows: in Sec. 2.2, the necessity assumptions of the classic transport and its failures are explained. Comparison of system size with characteristic length scales are presented in Sec. 2.3, in order to categorize the respective transport regime. Landauer-Büttiker formalism is discussed in Sec. 2.4, which ends to the derivation of the conductance in terms of transmission channels.

2.2. Transport problem

Transport analysis in large macroscopic systems, like ordinary metal wires, is supported by the *Boltzmann transport equation* and its application to devices. The assumptions

usually made for studies are as follows: (i) scattering processes are local and occur at a single point in space; (ii) the scattering is instantaneous in time; (iii) the scattering is very weak and the fields are low, such that these two quantities form separate perturbations on the equilibrium system; (iv) the time scale is such that only events that are slow compared to the mean free time between collisions are of interest [40].

When the scale of interconnects approaches dimensions of the order of the electron mean free path, assumptions of the classical Boltzmann theory are no longer applicable. Theoretical investigations of the size effects date back to 1901, when J. J. Thomson [41] related the origin of high resistivity of metal thin films to the limitation of the electron mean free path and diffusive scattering at the surface of films. In 1938, Fuchs [42] derived an expression for the resistivity of thin films based on the semi-classical concept of relaxation time approximation.[1] An extra degree of confinement in the form of a wire was considered by Sondheimer [43]. Later on, this treatment within the appropriate boundary conditions was applied to the electrical resistivity calculation of thin wires with circular cross-section by Dingle [44], with square cross-section by McDonald and Sarginson [45], and with rectangular cross-section by Ditlefsen and Lothe [46].

Despite extensively testing the semi-classical transport theory against the experimental data, this approach fails in description of transport phenomena, when devices scale down to the further mesoscopic range, in which quantum effects arise from the wave nature of electrons. Replacing traditional theories by a quantum approach corrects the drawback of picturing transport in modern nanoscaled devices.

2.3. Characteristic lengths

To clarify the limit of each transport regime, an adequate comparison of device extension and characterized criteria should be considered. In this regard, some of the length scales relevant to the studied issue are introduced. Presented descriptions maintain main concepts used by S. Datta [14], Th. Heinzel [47], and P. A. Mello [48].

2.3.1. The Fermi wavelength (λ_F)

The *Fermi wavelength* is the *de Broglie wavelength* of conducting electrons at the Fermi energy that dominates electrical transport and is given by $\lambda_F = 2\pi/k_F$, where k_F is

---

[1]An electron experiences a collision with probability dt/τ, where the relaxation time, τ, depends on the position, wave vector, and bond index of the electron. In the relaxation-time approximation, it is assumed that some time after scattering the electron distribution does not depend on the non-equilibrium distribution just before the scattering. In other words, the information about the non-equilibrium state is completely lost due to the scattering processes and that the thermodynamic equilibrium corresponding to a local temperature is maintained through the scattering [3].

the Fermi wave number. Quantum size effects could take place at the length scale comparable to the Fermi wavelength. The Fermi wavelength strongly depends on the carrier density: higher carrier density, lower Fermi wavelength. Therefore, it is much shorter in metals than semiconductors (i.e., for copper λ_F = 0.46 nm as deduced from the electron density of bulk copper [49]).

2.3.2. The elastic mean free path (ℓ_{el})

In an electric conductor, an electron frequently interacts with perturbations. These scattering processes can reduce the electrons velocity and drastically the travelling direction. The average time between consecutive scatterings of arbitrary strength is known as *momentum relaxation time*, which is in fact weighting each scattering event with the scattering angle φ by the factor of $\left(1 - cos(\varphi)\right)$. The length scale related to the momentum relaxation time indicates the average distance that an electron travels destroying the initial momentum during individual collision. The momentum is not lost by a large scattering angle, and the electron moves between subsequent elastic and phase preserving scattering events through its elastic mean free path, which is represented in terms of collision time, τ_{el}, and the Fermi velocity of electron, v_F, at the Fermi energy as $\ell_{el} = v_F \tau_{el}$. The typical value of the Fermi velocity for copper is as 1.57×10^6 m/s [3].

2.3.3. The phase coherence length (ℓ_φ)

In analogy to the elastic mean free path, the *phase coherence length* is the average length an electron travels before suffering inelastic scattering and loosing the original phase state. The phase coherent length or phase relaxation length is connected to the phase relaxation time via the Fermi velocity as $\ell_\varphi = v_F \tau_\varphi$.

The phase coherence length can be tens of μm in a *two-dimensional electron gas* (2DEG) and up to several μm in regular metals. The ℓ_φ decreases generally with increasing the temperature, or increasing density of states at the Fermi energy due to the scattering events (e.g., electron-phonon or electron-electron collisions). These scatterings change the energy of the electron and randomize its quantum mechanical phase. Impurity scattering could be another source of changing electron phase state by an internal degree of freedom, such as magnetic impurities having an internal spin that fluctuates with time. Different paths of one electron can only interfere with each other, if the phases are preserved coherently.

2.3.4. The localization length (ℓ_ξ)

The average spatial length of a *localized quantum mechanical state* (i.e., wave function) in a disorder system is known as *localization length*. P. W. ANDERSON [50] was the first, who showed that certain states are localized due to disorder, and their localization crucially depends on the nature of disorder.

2.3.5. System dimensions (L)

Comparing the range of *device scale* with the other characteristic lengths indicates the relevant transport regime. Typically, system dimension may vary in different directions. As a simple example, consider a rectangular system of L_x, L_y, and L_z dimensions. Device classification is based on comparison of the system Fermi wavelength with its dimensions. Table 2.1 identifies the device classification according to the relation of λ_F with the system size.

Table 2.1.: Device classification based on the comparison of characteristic lengths [51].

Condition	Dimensionallity	Device Sample
$\lambda_F \ll L_z$	3D	bulk crystals
$\lambda_F \sim L_z$	quasi-2D	thin films
$L_z < \lambda_F \ll L_y$	2D	MOSFETs
$L_y \sim \lambda_F < L_x$	quasi-1D	quantum wires
$L_y < \lambda_F < L_x$	1D	atomic chains
$L_x < \lambda_F$	0D	quantum dots

The Fermi wavelength reduces with increasing the electron density of system. Taking the *Pauli exclusion* into account for electrons with spin degeneracy of 2, and within the effective mass approximation, the relation between λ_F and electron density for different dimensionality becomes as follows:

$$\lambda_F = 2^{3/2} \left(\frac{\pi}{3n}\right)^{1/3} . \tag{2.1}$$

The electronic density in three dimensions in terms of the Fermi wave vector is written as $n = k_F^3/3\pi^2$, and the number of non-interacting electrons in the considered sample is $N = V k_F^3/3\pi^2$, where the volume of sample,V, is assumed to be rather large compared to the Fermi wavelength. The density of states as the most important measure of

the number of states (i.e., states available for occupancy generally at the Fermi energy dominating the transport processes) has a general definition as follows:

$$g(\varepsilon)\, d\varepsilon = \frac{1}{V}\left[\textit{the number of allowed states}\right.$$
$$\left.\textit{in the energy range from } \varepsilon \textit{ to } d\varepsilon\right]. \tag{2.2}$$

The energy dispersion of a free electron in terms of $\boldsymbol{k}$ is $\varepsilon(k_x, k_y, k_z) = \hbar^2(k_x^2 + k_y^2 + k_z^2)/2m$ and $d\varepsilon = \boldsymbol{\nabla}\varepsilon \cdot d\boldsymbol{k}$, where $\boldsymbol{\nabla}$ is the gradient in k-space. The density of states, which can be expressed as:

$$g_{3D}(\varepsilon)\, d\varepsilon = \int g(\boldsymbol{k})\, d^3k, \tag{2.3}$$

gives the relation of:

$$
\begin{aligned}
g_{3D}(\varepsilon) &= \frac{2}{(2\pi)^3}\int d^3k\, \delta\Big(\varepsilon - \varepsilon(\boldsymbol{k})\Big) \\
&= \frac{2}{(2\pi)^3}\int d^3k\, \delta\Big(\varepsilon - \frac{\hbar^2 \boldsymbol{k}^2}{2m}\Big) \\
&= \frac{2}{(2\pi)^3}\frac{d}{d\varepsilon}\Big(\frac{4}{3}\pi\big(k(\varepsilon)\big)^3\Big) \\
&= \frac{1}{\hbar^3\pi^2}\sqrt{2m^3\varepsilon}.
\end{aligned}
\tag{2.4}
$$

The Fermi-surface of a $3D$ system is spherical, and the g_{3D} scales with $\sqrt{\varepsilon}$.

In a two-dimensional device confined in one direction for example L_z, the integral is the sum over allowed wave vectors of $k_z = 2n_z/L_z$, where n_z is an integer number, and corresponding energy is $\varepsilon_{n_z} = (\hbar\pi n_z)^2/2mL_z^2$. The density of states for a two-dimensional device is obtained as:

$$
\begin{aligned}
g_{2D}(\varepsilon) &= \frac{2}{(2\pi)^2}\int dk_x\, dk_y \sum_{n_z} \delta\Big(\varepsilon - \frac{\hbar^2}{2m}\Big[k_x^2 + k_y^2 + (\frac{\pi n_z}{L_z})^2\Big]\Big) \\
&= \frac{1}{2\pi^2}\sum_{n_z}\frac{d}{d\varepsilon}\Big(\pi\big[k(\varepsilon - \varepsilon_{n_z})\big]^2\Big) \\
&= \frac{m}{\pi\hbar^2}\sum_{n_z}\Theta\big(\varepsilon - \varepsilon_{n_z}\big),
\end{aligned}
\tag{2.5}
$$

where $\Theta(\varepsilon - \varepsilon_{n_z})$ denotes the *Heaviside step function*. In the $2D$ case, the Fermi-surface is a ring with radius of k_F, and g_{2D} is independent of energy.

Van Hove singularities [52] occur in the density of states if the extra restriction to the L_y is applied. In fact, the singularities appear when the gradient of ε vanishes, and hence the density of states diverges. The $g(\varepsilon)$ for a one-dimensional system is integrated as:

$$
\begin{aligned}
g_{1D}(\varepsilon) &= \frac{2}{2\pi} \int \mathrm{d}k_x \sum_{n_y, n_z} \delta\left(\varepsilon - \frac{\hbar^2}{2m}\left[k_x^2 + \left(\frac{\pi n_y}{L_y}\right)^2 + \left(\frac{\pi n_z}{L_z}\right)^2\right]\right) \\
&= \frac{1}{\pi} \sum_{n_y, n_z} \frac{\mathrm{d}}{\mathrm{d}\varepsilon}\left(2k\left(\varepsilon - \varepsilon_{n_y} - \varepsilon_{n_z}\right)\right) \\
&= \frac{\sqrt{2m}}{\pi\hbar} \sum_{n_y, n_z} \left(\varepsilon - \varepsilon_{n_y} - \varepsilon_{n_z}\right)^{-1/2},
\end{aligned}
\tag{2.6}
$$

and the Fermi-surface is two points at $\pm k_F$.

In a zero-dimensional structure, the electron is confined in all three spatial directions in a quantum box without any free motion. Consequently, there is no k-space available which could be filled up with electrons. All available states exist at discrete energies, and the density of states is represented by a δ function:

$$
\begin{aligned}
g_{0D}(\varepsilon) &= 2 \sum_{n_x, n_y, n_z} \delta\left(\varepsilon - \frac{\hbar^2}{2m}\left[\left(\frac{\pi n_x}{L_x}\right)^2 + \left(\frac{\pi n_y}{L_y}\right)^2 + \left(\frac{\pi n_z}{L_z}\right)^2\right]\right) \\
&= 2 \sum_{n_x, n_y, n_z} \delta\left(\varepsilon - \varepsilon_{n_x} - \varepsilon_{n_y} - \varepsilon_{n_z}\right).
\end{aligned}
\tag{2.7}
$$
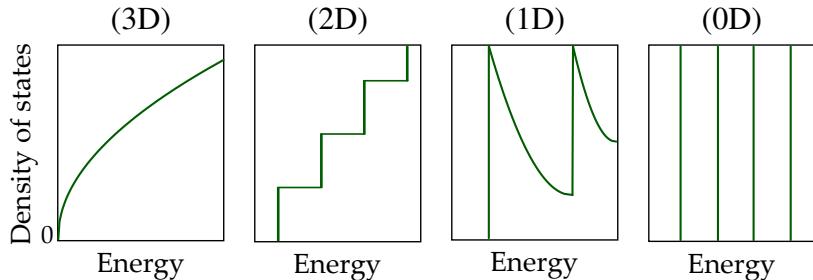
Figure 2.1.: Energy-dependent density of states for a three- to zero-dimensional system.

Although talking about Fermi-surface for a zero-dimensional structure is confusing due to the discrete nature of the spectrum, there is still an energy separating the occupied states from the unoccupied ones when the system is in the ground state. Fig. 2.1 illustrates energy dependent density of states in systems of different dimensionalities. Systems of two, one, and zero degrees of freedom are referred to as quantum wells, quantum wires, and quantum boxes, respectively.

2.3.6. Transport classification

Comparing the length scales discussed in the previous sections with system size leads to the classification of electronic transport regimes in the *absence of magnetic fields and temperature gradients*. A comparison of characteristic lengths and attributed transport regimes are shown briefly in Table 2.2. For mesoscopic structures, the length *L*, and width *W*, of the system are considered to be comparable with characteristic lengths.

Table 2.2.: A comparison of transport regimes.

Condition	Transport regimes
$\lambda_F, \ell_{el}, \ell_\varphi \ll L$	classic
$\ell_{el} \ll L$	diffusive
$\ell_{el} \gg L$	ballistic
$W < \ell_{el} < L < \ell_\xi$	quasi-ballistic
$\ell_\varphi \gtrsim L$	coherent
$\ell_\varphi \ll L$	incoherent
$\ell_\xi \ll L$	strong localization
$\ell_\xi \sim L$	weak localization

The electron transport is *diffusive* through a device, when the mean free path is much smaller than the system size. Electrons undergo numerous scattering events, when they travel along the device, and the conduction is dominated by electrons scattering within the device due to phonons, boundary scattering, and structural defects.

If the phase coherence length is also much smaller than the device size, transport is known as *incoherent*, and the scattering sources contribute *ohmically* as in a classical conductors. In contrary, for *coherent* regime the resistance grows exponentially with the length. Since electrons pass the sample coherently, the complex interference effects are expected.

The *ballistic transport* occurs, when the mean free path is large compared to the relevant sample length. Ballistic transport phenomena are usually observed in very short quantum wires, where the wave propagates through the sample without any elastic or phase breaking scattering. The canonical example is the point contact; the impurity scattering can be neglected, and electron scattering occurs only at the boundaries. In this regime, any local quantity has lost its meaning, so only conductance plays a role, not conductivity. If $\ell_{el} \gg L$, the resistance of a system, like a quantum wire, would be independent of *L* and arises from the interfaces between the conductor and contacts. Furthermore, the size quantization occurs, when the contact size decreases down to the *atomic scale* in the range of Ångstrom comparable with the Fermi wavelength, which

is sorted in quantum ballistic regime. *Coulomb blockade* or *resonant tunneling* is the typical effect of this regime.

The special case of $W < \ell_{el} < L < \ell_{\xi}$, for which boundary and the internal scattering have the same importance, can be called the *quasi-ballistic* regime. A schematic view of diffusion, ballistic, and quasi-ballistic transports is illustrated in Fig. 2.2.
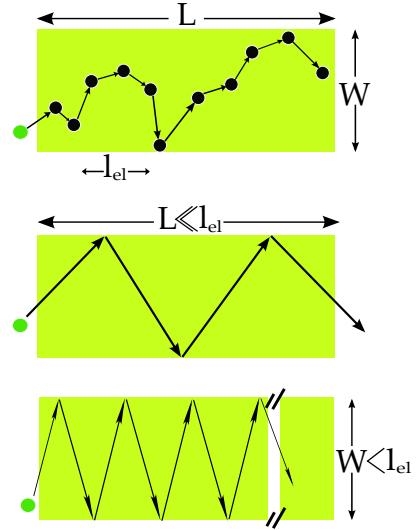
Figure 2.2: Schematic description of three transport mechanisms. Top to down: diffusive, ballistic, and quasi-ballistic transport regimes.

In the regime of condition $\ell_{\xi} \ll L$, *strong localization regime*, the resistance grows exponentially with the size. When the system length is comparable with the localization length, *weak localization* is supposed.

2.4. Theory of conductance: from macroscopic to atomic scale

Since the conductance is the most natural quantity in description of electron transport through the metal contacts, it would be used instead of resistance. The conductance of a typical macroscopic contact, which is in diffusive transport regime, obeys the Ohm's law as $G = I/V$. For a rod shape contact with cross-sectional area A, length L, and conductivity σ, the Ohm's law gives $G = \sigma A/L$. In spite of the universality of the Ohm's law, the derived simple relation for conductance is not applicable for mesoscopic structures of coherent transport regime, where the *scattering theory* of quantum mechanics is recovered. In classical mechanics, collisions of two particles are entirely determined by their velocities and impact parameter (i.e., the distance at which particles would pass without interacting).

In quantum mechanics, assuming all ingoing particles as wave packets after scattering on a localized potential, the outgoing wave packets are presented as the transmission probability. In the ballistic transport condition (see Sec. 2.3.6), scattering in the interior of the contact is neglected and electrons move ballistically through the contact. Ballistic constrictions with the size quantization result a current in terms of the transmission probability of standing waves formed by electrons, and the measured conductance is in fact quantized in multiple integers of the *quantum conductance* in units of $G_0 = 2e^2/h$. A useful phenomenological approach proposed by LANDAUER [4] is described in next section in order to study the mesoscopic transport taking quantum effects into account.

2.4.1. Landauer-Büttiker formalism: two-terminal 1D and 3D cases

According to the *Landauer theory*, the conductance of a piece of one-dimensional conductor is addressed as a problem in the barrier tunneling characterized by the transmission probability and the *single channel case*, where only one *transmission channel* is occupied. In a *two-terminal conductor* (i.e., two electrodes acting as reservoirs), assuming thermally equilibrium conditions, chemical potential of both reservoirs is equal. A scheme of the two-terminal one- and multi-channel conductor is shown in Fig. 2.3.
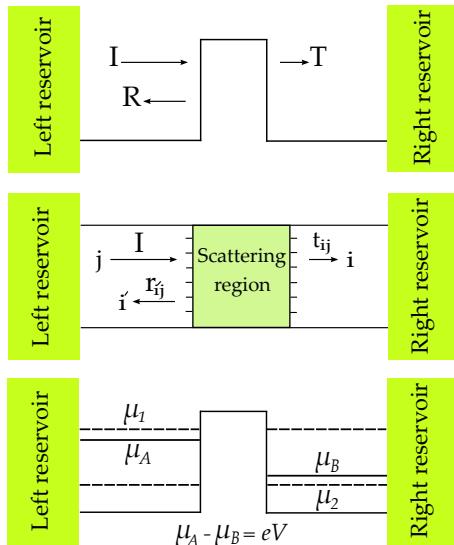
Figure 2.3: Top to down: illustration of the barrier model of a two-terminal one-dimensional conductor, transmission and reflection of a two-terminal multi-channel system, and its barrier model after applying a bias voltage to the reservoirs.

By changing the chemical potential at the right side, $(\mu_L > \mu_R)$, electrons will move to the right, resulting in a current to the left. The current carried by electrons with velocity of $v(k) = \hbar^{-1} d\varepsilon/dk$ is written as an integral over the flux:

$$I = \frac{2e}{2\pi}\left[\int_0^\infty dk\, v(k)\, f_L(k)\, T(\varepsilon) - \int_0^\infty dk'\, v(k')\, f_R(k')\, T(\varepsilon')\right], \qquad (2.8)$$

where the constant is the one-dimensional density of states in k-space with the factor 2 originating from spin degeneracy, $T(\varepsilon)$ is the transmission coefficient, and f_L and f_R are the *Fermi distribution functions* of left and right reservoirs, respectively. Considering low temperatures (i.e., the thermal activation of electrons is negligible), electrons are injected up to energy μ. Converting to integrals over energy, the current becomes:

$$
\begin{aligned}
I &= \frac{2e}{h} \left[\int d\varepsilon \, T(\varepsilon) \left(f(\varepsilon - \mu_L) - f(\varepsilon - \mu_R) \right) \right] \\
&= \frac{2e}{h} \left[\int d\varepsilon \, T(\varepsilon) \left(-\frac{\partial f}{\partial \varepsilon} \right) \right] (\mu_L - \mu_R).
\end{aligned}
\tag{2.9}
$$

In addition, the linear transmission is expected by assuming small applied voltage. In other words, the energy dependency of $T(\varepsilon)$ is negligible and can be calculated at the Fermi energy. At zero temperature, the current is obtained as a simple relation:

$$
I = \frac{2e}{h} T (\mu_L - \mu_R).
\tag{2.10}
$$

The voltage between reservoirs, $\mu_L - \mu_R$, is greater than the actual voltage drop across the scattering area defined as $eV = (\mu_A - \mu_B)$. After connecting the system to reservoirs, μ_A and μ_B levels are formed. These levels are determined by making equal number of occupied states (electrons) above $\mu_A(\mu_B)$ with empty states (holes) below $\mu_A(\mu_B)$. The number of states occupied above μ_B on the right side due to injection from the left is $TD(\varepsilon)(\mu_L - \mu_B)$, where $D(\varepsilon)$ is the density of states. Likewise, the number of unoccupied states below μ_B is given by $(2 - T) D(\varepsilon)(\mu_B - \mu_R)$. According to the previous discussion, it is possible to write as:

$$
T (\mu_L - \mu_B) = (2 - T)(\mu_B - \mu_R).
\tag{2.11}
$$

Similarly, for the left side, it can be defined as:

$$
(1 + R)(\mu_L - \mu_A) = \left(2 - [1 + R] \right)(\mu_A - \mu_L),
\tag{2.12}
$$

where R is the reflection probability related to T by $R = 1 - T$. Combining two equations gives:

$$
\mu_A - \mu_B = (1 - T)(\mu_L - \mu_R).
\tag{2.13}
$$

Substituting Eq. 2.13 into Eq. 2.10 gives the current as:

$$
I = \left(\frac{2e}{h} \right) \frac{T}{1 - T} (\mu_A - \mu_B).
\tag{2.14}
$$

By considering the quantum conductance (i.e., one quantum conductance corresponds to a resistance of 12.907 kΩ) introduced in Sec. 2.4, the conductance is found as:

$$G = \frac{I}{V} = \frac{2e^2}{h} \frac{T}{1-T} = G_0 \frac{T}{R}, \tag{2.15}$$

which is the *single-channel Landauer formula* and gives the ideal conductance as T approaches one. In practice, in a two-terminal measurement in addition to the voltage drop across the scattering area, a contact voltage drop across the ideal reservoirs is measured, which is known as the result of self-consistent charge at the interface of reservoirs. Therefore, based on the overall voltage drop, $eV = (\mu_L - \mu_R)$, the practical form of the *Landauer formula* for a two-terminal one-dimensional conductance developed by BÜTTIKER [53] is simply given by:

$$G = \frac{2e^2}{h} T = G_0 T, \tag{2.16}$$

which has a finite value for the total transmission as $T = 1$ due to the *contact resistance*, $R_c = 2e^2/h$.

The single-channel case of the *Landauer-Büttiker formalism* must be generalized to the multichannel case, when the sample has a finite cross-section area. In the $3D$ model illustrated in Fig. 2.3, there are discrete energies due to quantization in the transverse direction. Hence, a complete set of N channels, where all of which may contribute to the current, are considered. Supposing a simple multichannel case, two similar reservoirs have the equal number of channels, N. The transmission probability for incoming wave from the channel i on the left side into the channel j on the right is defined as $T_{ji} = \left| t_{ji}^2 \right|$.

Similarly, the reflection probability is given by $R_{ji} = \left| r_{ji}^2 \right|$. To describe the relation between incoming and outgoing waves, the $2N \times 2N$ *scattering matrix* is constructed based on the transmission and reflection amplitudes from left to right, t and r, and right to left, t' and r', respectively:

$$S = \begin{pmatrix} r & t' \\ t & r' \end{pmatrix}. \tag{2.17}$$

Using the same single-channel current argument from Eq. 2.9 for multichannel case results:

$$I = \frac{2e}{h} \left[\int d\varepsilon \sum_i T_i(\varepsilon) \left(-\frac{\partial f}{\partial \varepsilon} \right) \right] (\mu_L - \mu_R). \tag{2.18}$$

Correspondingly, the conductance between the outside reservoirs is given by:

$$G = \frac{eI}{\mu_L - \mu_R} = \begin{cases} \frac{2e^2}{h} \int d\varepsilon \left(-\frac{\partial f}{\partial \varepsilon} \right) \sum_i T_i(\varepsilon), & T \neq 0\ K \\[2mm] \frac{2e^2}{h} \sum_i T_i(\varepsilon_F), & T = 0\ K \end{cases}, \tag{2.19}$$

where the sum over T_i, which is the eigenchannel transmission probability of the channel i, is written in terms of the transmission submatrices as:

$$\sum_{i=1}^{N} T_i = \sum_{i,j=1}^{N} T_{ij} = \sum_{i,j=1}^{N} \left| t_{ij}^2 \right| = \sum_{i,j=1}^{N} t_{ij} t_{ji}^* = \mathrm{Tr}\left[tt^\dagger \right], \quad (2.20)$$

so the conductance at zero temperature, $G = G_0 \, \mathrm{Tr}\left[tt^\dagger \right]$, is simplified to the three-dimensional conductance Landauer-Büttiker formula:

$$G = G_0 \sum_i T_i. \quad (2.21)$$

2.4.2. The concept of eigenchannels

To describe electron transport in a contact with the size comparable to the Fermi wavelength, the Landauer-Büttiker formalism was explained in the previous section. According to this theory, the two-terminal three-dimensional conductance is expressed in terms of the transmission probabilities of single, independent channels, so-called *transverse modes* or *eigenchannels*, which are actually measured experimentally and are not only mathematical abstractions [17]. System properties such as *conductance fluctuations, the shot noise, dynamical Coulomb blockade, and the supercurrent* are predicted based on the eigenchannels, T_i's.

Necessarily, eigenchannels carrying the current are determined by the number of available valence orbitals of the considered atom and hence differ for metallic elements in different series of the periodic table. In spite of the conductance quantization in quantum point contacts in 2DEG predicted in the Landauer-Büttiker formula, it does not occur for the metallic atomic-scale contacts due to dependency of the transmission of each channel on the material forming the contact, detailed atomic arrangement, and applied stresses. Consequently, these valence channels are not always fully open (i.e., the conductance is not always the integer multiple of quantum conductance). They may even be completely closed or only some partially open channels contribute to the conductance. For instance, the channel transmission has been demonstrated experimentally in monatomic gold wires showing only one conducting channel of sp_z character, which is contributed to the conductance with a value of about $1G_0$, and its variations about 10%–15% are observed during the measurement [54].

Chapter 3.

Electronic Transport Calculations

3.1. Introduction

The theory of electronic transport has been discussed in the previous chapter. The present chapter takes a look at the methodology of transport calculations closely following the presentation flows in the work by A. Pecchia [35].

The motion of electrons in a solid is described through the *many-body wave functions* addressing quantum mechanical behavior. These wave functions are obtained by solving the well known *time-independent Schrödinger equation*, which is an impossible task for systems with a huge number of electrons, and appropriate approximations and formalisms are needed to treat the potential of simultaneous interacting electrons. This purpose is supported from several approaches, where the density functional based method is of interest in the present study. In order to overcome the limits of density functional method formulated by Kohn and Sham, it is mixed with *tight-binding model* to handle the huge number of carriers in metals. Furthermore, combination of the density functional tight-binding model with the *Green's function* technique provides an efficient way to obtain transport properties for the mesoscopic systems, and the *non-equilibrium Green's function method* is involved in order to consider the biased devices.

This chapter is organized as follows: the many-body problem and Schrödinger equation are presented briefly in Sec. 3.2. Density functional theory and related approximations are described in Sec. 3.3. A short introduction on tight-binding model and the combination with density functional theory are presented in Sec. 3.4. In Sec. 3.5, setup of the system under study is given in order to deduce the quantum transport formula related to the employed method. The Green's function technique is introduced in Sec. 3.6, and its development to the non-equilibrium case is discussed in Sec. 3.7.

3.2. The many-body problem

Electrons in a solid are considered as a system of identical particles, for which methods of *many-body problems* are applied.[1] To describe completely the quantum mechanical behavior of electrons in solids, it is strictly necessary to calculate the many-electron wave functions. This purpose is obtained from the *time-independent Schrödinger equation*:

$$\mathcal{H}\,\Phi\,(\mathbf{r},\mathbf{R}) \;=\; E\,\Phi\,(\mathbf{r},\mathbf{R})\,, \tag{3.1}$$

where $\mathcal{H}$ is the time-independent Hamiltonian operator, which acts on the spatial part of the system wave function, Φ, and yields the system eigenvalues, E. $\mathbf{R}$ and $\mathbf{r}$, indicate the position vectors of nuclei and electrons, respectively.

In a system composed of N_e electrons and N_n nuclei interacting via the *Coulombic forces*, the *many-body Hamiltonian* is written as:

$$\mathcal{H} = \sum_i^{N_e} \frac{\mathbf{P}_i^2}{2m_i} + \sum_I^{N_n} \frac{\mathbf{P}_I^2}{2M_I}$$
$$+ \frac{e^2}{4\pi\varepsilon_0}\left[\frac{1}{2}\sum_i^{N_e}\sum_{j\neq i}^{N_e} \frac{1}{|\mathbf{r}_i - \mathbf{r}_j|} + \frac{1}{2}\sum_I^{N_n}\sum_{J\neq I}^{N_n} \frac{Z_I\,Z_J}{|\mathbf{R}_I - \mathbf{R}_J|} - \sum_i^{N_e}\sum_I^{N_n} \frac{Z_I}{|\mathbf{r}_i - \mathbf{R}_I|} \right], \tag{3.2}$$

where indices i and j run over the electronic degrees of freedom, and I and J run over those of the nuclei. M is mass of the nuclei, m that of the electron, and $\mathbf{P}_I$ and $\mathbf{P}_i$ are the ionic and electronic momentum operators, respectively. Rest terms denote the Coulomb potential of nuclei, electrons, and nuclei-electrons, respectively. The factor of 1/2 appeared in terms of electron-electron and nuclei-nuclei interactions is included in order to avoid double counting of terms.

While writing the many-body Hamiltonian in Eq. 3.2, the SI units have been employed. As a result of this, each term includes certain cumbersome combination of fundamental constants: h, m, e, and ε_0. A more natural unit system to employ for this problem is the *atomic unit system*. In atomic units, the fundamental length and energy are measured in terms of *Bohr radius* and *Hartree*, respectively.[2]

---

[1]Two particles are identified if they possess the same intrinsic properties (i.e., properties do not depend on the dynamical states of particles).

[2]The Bohr radius is the mean radius of the orbit of an electron around the nucleus of a hydrogen atom at its ground state, and a Hartree is the ground state energy of that electron, respectively are written as:

$$a_0 \;=\; \frac{4\pi\varepsilon_0\hbar^2}{m_e e^2} \quad and \quad E_H \;=\; \frac{\hbar^2}{m_e a_0^2} \;=\; \frac{e^2}{4\pi\varepsilon_0}.$$

The rescaling of quantities outlined above is equivalent with setting $\hbar = m_e = e = 1/4\pi\varepsilon_0 = 1$.

In theory, the kinetic energy term is the sum of kinetic energies of electrons and nuclei. However, because the ions are several tens of thousands of times heavier than the electrons, their contribution to the kinetic energy is usually neglected. This is called the *Born-Oppenheimer approximation*. In light of the Born-Oppenheimer approximation, only electrons have a quantum mechanical identity in the problem at hand. Thus, apart from a constant term brought around by the Coulombic interaction between nuclei, the eigenfunctions of the Hamiltonian depend only on the electronic variables. In other words, according to the Born-Oppenheimer approximation, the total wave function is written as a product of a nuclear part, $\Upsilon(\mathbf{R})$, and an electronic part, $\Psi(\mathbf{r}\,;\,\mathbf{R})$, where the semicolon represents the fact that the nuclear coordinates are static parameters:

$$\Phi(\mathbf{r}\,,\,\mathbf{R}) \,=\, \Psi(\mathbf{r}\,;\,\mathbf{R})\,\Upsilon(\mathbf{R})\,. \tag{3.3}$$

By separating this problem into an electron problem parametric in the nuclei coordinates and a nuclei part, the Hamiltonian describing electrons motion would consist of the electronic kinetic energy, the electronic Coulomb repulsive potential energy, and the effective potential from static nuclei as:

$$\mathcal{H}_{el} \,=\, \sum_i^{N_e} \frac{\mathbf{P}_i^2}{2m_i} + \frac{1}{2}\sum_i^{N_e}\sum_{j\neq i}^{N_e} \frac{1}{\left|\mathbf{r}_i - \mathbf{r}_j\right|} - \sum_i^{N_e}\sum_I^{N_n} \frac{Z_I}{\left|\mathbf{r}_i - \mathbf{R}_I\right|}\,. \tag{3.4}$$

Although the many-body Hamiltonian in Eq. 3.4 seems very straightforward, the exact solution is an impossible task for the systems having more than a few electrons. Several methods have been devised to find the accurate approximations. Two broad classes of methods are *wave function-based* and *density-based*, and each of these classes is further subdivided into the different approaches:

1. **Wave function-based methods:** An explicit form for wave function is defined for calculating the observables. The method is classified as follows:

   - Perturbational: *Møller-Plesset perturbation theory* [55],

   - Variational: *Hartree-Fock theory* based on the *variational principle* [56],

2. **Density-based methods:** The focus is shifted from the wave function to the electronic density, which is described further. Examples are *Thomas-Fermi approximation* [21] and *density-functional theory* [22, 23].

The last method is of interest in the present work due to its computational efficiency.[3] Hence, the density functional theory and corresponding approximations are explained in the next section.

---

[3]The formal scaling behavior of density-based methods has been noted to be no worse than N^3, where N is the number of basis functions. This scaling is better than the wave function-based methods by a factor of N [57]

3.3. The density functional theory

3.3.1. The Hohenberg-Kohn theory

Density functional theory is an alternative to solve the non-relativistic time-independent Schrödinger equation in terms of the density and is based on two theorems from HOHEN-BERG-KOHN [24] and KOHN-SHAM [25]. Hohenberg and Kohn suggested that the many-electron wave function is too complicated to deal with as the fundamental variable in a variational approach. Instead, they chose to use the electron density by considering the ground state of the system to be defined by that electron density distribution minimizing the total energy. The *Hohenberg-Kohn theorem* can be expressed as: *the ground state density, $n(\mathbf{r})$, of a bound system of interacting electrons in some external potential, $v(\mathbf{r})$, determines this potential uniquely.*

3.3.2. The Kohn-Sham equations

In order to make a practical treatment of Hohenberg-Kohn theory, Kohn and Sham introduced a simple form of the Hamiltonian equation derived from the variational approach to handle the kinetic and interaction energy terms. The so-called *Kohn-Sham equation* is similar in form to the time-independent Schrödinger equation, except that the potential experienced by the electrons is formally expressed as a function of the electron density. In this approach, the functional energy is considered in the following term:

$$E\left[n(\mathbf{r})\right] = T_s\left[n(\mathbf{r})\right] + U_H\left[n(\mathbf{r})\right] + E_{XC}\left[n(\mathbf{r})\right] + \int n(\mathbf{r})\, v_{ext}(\mathbf{r})\, d\mathbf{r}. \tag{3.5}$$

The functional $T_s\left[n(\mathbf{r})\right]$, which is called the Kohn-Sham kinetic energy, is just a particular case of the non-interacting electron gas written in terms of the non-interacting orbitals as:

$$T_s\left[n(\mathbf{r})\right] = -\frac{1}{2}\sum_{i=1}^{N}\int \Psi_i^*(\mathbf{r})\,\nabla^2\Psi_i(\mathbf{r})\, d\mathbf{r}. \tag{3.6}$$

The U_H stands for the classical electrostatic interaction energy or Hartree energy, describing the direct Coulomb interaction between an electron and the average electron distribution and is given by:

$$U_H = \frac{1}{2}\int\int \frac{n(\mathbf{r})\,n(\mathbf{r}')}{\left|\mathbf{r}-\mathbf{r}'\right|}\, d\mathbf{r}\, d\mathbf{r}', \tag{3.7}$$

because the numerical integration is complicated, the equivalent differential *Poisson's equation* is required. The new energy term, E_{XC}, represents the electron-electron interaction due to the *exchange* and *correlation effects*. The exchange potential arises as

a direct consequence of including the *Pauli exclusion principle* through the use of an anti-symmetrized wave function, and the correlation energy is the additional energy obtained in a real system due to the mutual avoidance of the interacting electrons. Hence, the kinetic energy of the interacting system can be a part of E_{XC}. In general, the form of exchange-correlation energy is unknown and needs to be approximated. The last term of energy arises from an external potential, which is usually the electrostatic potential of the nuclei and is taken to be fixed in space according to the Born-Oppenheimer approximation. Only this potential is easy to treat, since it is a multiplicative operator. Minimizing Eq. 3.5 with respect to the density yields the ground state energy. Because T_s is an orbital functional, it is not possible to minimize directly as:

$$\begin{aligned} 0 = \frac{\partial E\left[n(\mathbf{r})\right]}{\partial n(\mathbf{r})} &= \frac{\partial T_s\left[n(\mathbf{r})\right]}{\partial n(\mathbf{r})} + \frac{\partial U_H\left[n(\mathbf{r})\right]}{\partial n(\mathbf{r})} + \frac{\partial E_{XC}\left[n(\mathbf{r})\right]}{n(\mathbf{r})} + \frac{\partial V_{ext}\left[n(\mathbf{r})\right]}{\partial n(\mathbf{r})} \\ &= \frac{\partial T_s\left[n(\mathbf{r})\right]}{\partial n(\mathbf{r})} + v_H(\mathbf{r}) + v_{XC}(\mathbf{r}) + v_{ext}(\mathbf{r}). \end{aligned} \tag{3.8}$$

In order to indirect minimization, Kohn and Sham proposed a system consists of the non-interacting particles with minimization condition of:

$$0 = \frac{\partial E\left[n(\mathbf{r})\right]}{\partial n(\mathbf{r})} = \frac{\partial T_s\left[n(\mathbf{r})\right]}{\partial n(\mathbf{r})} + \frac{\partial V_{eff}\left[n(\mathbf{r})\right]}{\partial n(\mathbf{r})} = \frac{\partial T_s\left[n(\mathbf{r})\right]}{\partial n(\mathbf{r})} + v_{eff}(\mathbf{r}). \tag{3.9}$$

The Eq. 3.9 is an *Euler equation* [58], which needs density $n_{eff}(\mathbf{r})$ to be solved. Both energy minimization equations would have the same solutions as $n_{eff}(\mathbf{r}) = n(\mathbf{r})$ by accepting the *Kohn-Sham potential* as the following definition:

$$v_{eff}(\mathbf{r}) = v_H(\mathbf{r}) + v_{XC}(\mathbf{r}) + v_{ext}(\mathbf{r}). \tag{3.10}$$

In other words, density calculations of interacting many-body system through the many-body Schrödinger equation can be performed by the non-interacting single-body system in potential $v_{eff}(\mathbf{r})$ given by:

$$\left[-\frac{1}{2}\nabla^2 + v_{eff}(\mathbf{r})\right]\Psi_i(\mathbf{r}) = \varepsilon_i\Psi_i(\mathbf{r}). \tag{3.11}$$

Solving Eq. 3.11 gives orbitals reproducing the density $n(\mathbf{r})$ of the original system via:

$$n(\mathbf{r}) = n_{eff}(\mathbf{r}) = \sum_i^N f_i\left|\Psi_i(\mathbf{r})\right|^2, \tag{3.12}$$

where f_i is the occupation number of the orbital i.

The *celebrated Kohn-Sham equations*, Eqs. 3.10–3.12, provide theoretically an exact method to find the ground state energy of the interacting system by reducing the

problem to the single non-interacting Schrödinger equation, which should be solved self-consistently due to dependency of the Kohn-Sham potential on the density. The solution is started with an initial guess for $n(\mathbf{r})$, calculating the $v_{eff}(\mathbf{r})$, and then solving the differential Eq. 3.11 to find the $\Psi_i(\mathbf{r})$. Using Eq. 3.12, the new density is obtained, and the process is restarted until a reasonable convergence is reached.

3.3.3. Construction of exchange-correlation functionals

As mentioned before, the form of exchange-correlation energy is unknown generally, and its exact value has been calculated just for a few simple systems. The simplest density functional approximation for the exchange-correlation energy, which describes it as a function of local charge is known as the *local density approximation* (LDA) [25]. The general idea in LDA is approximating the E_{XC} by the exchange-correlation energy of an electron in an homogeneous electron gas of the same density $n(\mathbf{r})$, that is:

$$E_{XC}\left[n(\mathbf{r})\right] = \int \varepsilon_{XC}\left(n(\mathbf{r})\right) n(\mathbf{r}) \, \mathrm{d}\mathbf{r}, \qquad (3.13)$$

here $\varepsilon_{XC}\left(n(\mathbf{r})\right)$ is the exchange-correlation energy per particle assumed to be purely local as:

$$\varepsilon_{XC}\left(n(\mathbf{r})\right) = \varepsilon_{XC}^{hom}\left(n(\mathbf{r})\right). \qquad (3.14)$$

The most accurate data for the exchange-correlation energy of a homogeneous electron gas, $\varepsilon_{XC}^{hom}\left(n(\mathbf{r})\right)$, is from *quantum Monte Carlo calculations*. The most common parameterization has been computed by PERDEW and ZUNGER [59] based on the quantum Monte Carlo calculations of CEPERLEY and ALDER [60] on homogenous electron gases at various densities.

According to the Kohn-Sham theory [25], the LDA could be applied to the limited cases with slowly varying and very high densities. Despite the remarkable success of the LDA within the density functional theory over methods such as Hartree-Fock [56] (i.e., Hartree-Fock method may determine many experimentally relevant physical properties to a useful level of accuracy), an accurate description of chemical bonding is not expected, and limitations mean that care must be taken in its application.

An obvious approach to improve the LDA is to extend the exchange-correlation functional with terms containing gradients of the electron density. The corresponding approximation, which is called the *gradient expansion approximation* (GEA) [61], is valid for systems of slowly varying density.

A correction to the GEA by making more general functions of density and its gradients produces *general gradient approximation* (GGA) [62], giving a considerable

improvement over LDA. General form of exchange-correlation energy under GGA is written as:

$$E_{XC}^{GGA}\left[n(\mathbf{r})\right] = \int f_{XC}\left(n(\mathbf{r}), \nabla n(\mathbf{r})\right) \, d\mathbf{r}, \tag{3.15}$$

where f_{XC} is a correction chosen to satisfy limits for E_{XC}.

In order to determine the f_{XC}, several approaches have been proposed from LANGRETH and MEHL [63], PERDEW [64] BECKE [65], PERDEW and WANG [66, 67]. In comparison to LDA, GGA gives reliable results for chemical bonds, but fails for *van der Waals* or *dispersion interactions*.

3.4. The tight-binding model

In this section, the *tight-binding model* (TB) as an extensively used method predicting optical and electronic properties of nanostructures is described. This approach is introduced as a convenient approximation to the Schrödinger equation written in terms of the continuous real-space coordinates.

In the original TB model, the Hamiltonian is represented in terms of a basis set of atomic-like orbitals, $\Psi_\alpha(\mathbf{r} - \mathbf{R}_n)$, of site index n for an atom in position $\mathbf{R}_n$. The symmetry-related index α describes angular momentum and spin quantum number of the atomic orbitals on that site. The system wave function can be an extension of *linear combination of atomic orbitals* (LCAO), which in *Dirac notation* have the form of:

$$\left|\Psi\right\rangle = \sum_{n\alpha} c_{n\alpha} \left|n\alpha\right\rangle, \tag{3.16}$$

where $c_{n\alpha}$ cites the corresponding coefficient. Therefore, the Schrödinger equation in the TB scheme can be written as:

$$\sum_{n'\alpha'} \left[\mathcal{H}_{n\alpha, n'\alpha'} - E\, \mathcal{S}_{n\alpha, n'\alpha'} \right] c_{n'\alpha'} = 0, \tag{3.17}$$

where $\mathcal{H}_{n\alpha, n'\alpha'}$ denotes the Hamiltonian matrix element, and $\mathcal{S}_{n\alpha, n'\alpha'}$ is the overlap matrix between the atomic-like orbitals, respectively are written as:

$$\mathcal{H}_{n\alpha, n'\alpha'} = \left\langle n\alpha \left| \mathcal{H} \right| n'\alpha' \right\rangle \tag{3.18}$$

and

$$\mathcal{S}_{n\alpha, n'\alpha'} = \left\langle n\alpha \left| n'\alpha' \right\rangle. \tag{3.19}$$

The Eq. 3.17 can be formulated as the Kohn-Sham equations presented in Sec. 3.3.2, where the exact many-body Hamiltonian is replaced with a parameterized Hamiltonian matrix needed to be evaluated to solve the secular problem of Eq. 3.17.

Based on the Slater and Koster work as the initial point of the TB method [37], and further works of Ashcroft and Mermin [3], Mehl and Papacostantopoulos [68], the TB model can be categorized conditionally according to the *orthogonality of basis set*,[4] type of the matrix elements,[5] and the fact that the method of evaluating the matrix elements is *empirical, semi-empirical*, and or *ab-initio formulations*.

3.4.1. The TB scheme: from empirical to ab-initio approach

A pronounced advantage of the TB method is its capability to be ranged from a totally empirical approach, which is preferred for the large systems like nanostructure devices containing several thousand to one million atoms, to the fully ab-initio methods applicable to the systems with a few hundred atoms mostly used in material science.

Under empirical TB approach, the Hamiltonian and overlap matrix elements are evaluated as fitting parameters of quantities such as the band structure or the total energy of system. The desired accuracy for the application of interest is achieved by the parameterization treatment considering different interaction range (i.e., number of the nearest neighbors) [70, 71].

In spit of the computational efficiency and accuracy of the empirical TB approach, its limitations (e.g., parameterization, distance dependency of matrix elements, and transferability to the different scales) could be reduced by semi-empirical and ab-initio approaches using the first local orbital expansion of the eigenstates within the Hartree-Fock formulation [56] or density functional theory [22, 23].

3.4.2. TB model moving towards density functional theory

The standard density functional theory deals with a significant number of fundamental limitations when it comes to the quantitative applications. The main problem of the density functional theory is related to the description of the unknown exchange-correlation potential, usually approximated to be locally given by that of a free electron gas of equal density. This tends to overestimate the conductivity of the molecular states, producing among the others, and an underestimation of the Fermi energy with relevant consequences. Moreover, density functional theory is a ground-state theory, which provides

---

[4]In order to preserve the symmetry of basis functions and the hermeticity of the Hamiltonian, the basis set can be orthogonalized applying the *Löwdin orthogonalization procedure*, which produces wave functions with longer range than a few nearest neighbor distances. In contrast, range of the interaction in the non-orthogonal matrix elements is kept locally around each atom [69].

[5]The TB method is classified depending on how atomic wave functions and the potential are centered on sites (e.g., in two-center approach, the location of potential is the same as the location of one of the wave functions, while the other wave function is at a separate location).

at most an exact electronic density, but it is not meant to compute exact wave functions and single particle energy levels, both necessary ingredients of tunneling calculations. In order to obtain not only quantitative prediction of tunneling currents, but also correct quantitative trends, it is necessary to go beyond the density functional theory.

The empirical TB methods have been used commonly in solid-state physics due to their simplicity. In most cases even neglecting self-consistency, they more easily address the size problems. There have been numerous successful applications to a broad range of materials and systems [72, 73]. Additional developments take advantage of the strongly localized character of electronic interactions in the model (usually restricted to the nearest neighbors only) and together with so-called order-N methods [74–76], provide techniques for simulating structures with several hundred or even thousand atoms over a short time. Although the TB approach is based on the quantum mechanics, it lacks reliability and transferability due to the parameterization of the electronic Hamiltonian with respect to a finite set of equilibrium structures and properties. Additionally, there is serious weakness in having no well-defined procedure for constructing the required data from an atomic basis (wave functions and potentials) in a way, which could include any desired chemical element.

Therefore, during the last decade a strong effort has been put into the development of approximate methods, which try to merge the spirit and reliability of the density functional theory with the simplicity and efficiency of the TB model. The combination method as *density functional tight-binding* (DFTB) approach presents a second order approximation to density functional theory that is not only highly computationally efficient and well suited to large systems, but also it leads to the overcoming some of problems. DFTB is applicable to molecules, clusters, surfaces, bulks, and recently nanostructure devices [26–29].

What distinguishes this approach used in the present study from the fully empirical methods is the explicit calculation of the basis wave functions allowing deeper physical insight and better control of the applied approximations. This purpose is obtained by solving self-consistent Kohn-Sham equations using a *Mulliken charge projection* [77].

In this respect, the electronic density is expanded as a sum of a reference density, $n^0(\mathbf{r})$, and a deviation, $\delta n(\mathbf{r})$, given by:

$$n(\mathbf{r}) = n^0(\mathbf{r}) + \delta n(\mathbf{r}), \tag{3.20}$$

where the reference density is usually chosen as the superposition of neutral atomic density. The total energy of the system expanded up to the second order of local density fluctuations is written as:

$$E_{tot}\left[n\right] = \sum_k n_k \left\langle \Psi_k \middle| \mathcal{H}^0 \middle| \Psi_{k'} \right\rangle + E_{rep}\left[n^0\right] + E^{(2)}\left[n\right], \tag{3.21}$$

where k stands for the wave vector of eigenstates. The first term of Eq. 3.21 can be written in terms of a two-center TB Hamiltonian given by:

$$\mathcal{H}^0_{\mu\nu} = \begin{cases} \varepsilon^{free-atom}_{\mu\nu} & \mu = \nu \\ \\ \langle \phi_\mu | T + v_{eff}[n^0_i + n^0_j] | \phi_\nu \rangle & \mu \in i \quad \nu \in j \end{cases}, \tag{3.22}$$

where ϕ_μ and ϕ_ν are the atomic orbitals localized around the atomic centers i and j, respectively. T denotes the kinetic energy operator, and v_{eff} is the effective one-particle potential depending on the density of the two-atomic centers. $E_{rep}[n^0(\mathbf{r})]$ denotes the repulsive energy between the nuclei. This energy is short-ranged because of neutrality of the reference density and can be expressed as a summation over atomic pair contributions as follows [78]:

$$E_{rep}[n^0] = \frac{1}{2} \sum_{\alpha\beta} U_{\alpha\beta}(n^0_\alpha, n^0_\beta). \tag{3.23}$$

The third term in Eq. 3.22 as the second order correction to the Hartree potential and the exchange-correlation potential is given by:

$$E^{(2)}[\delta n] = \frac{1}{2} \int \int \left[\frac{1}{|\mathbf{r} - \mathbf{r}'|} + \frac{\delta^2 E_{XC}}{\delta n(\mathbf{r})\delta n(\mathbf{r}')} \right] \delta n(\mathbf{r}) \, \delta n(\mathbf{r}') \, d\mathbf{r} \, d\mathbf{r}'. \tag{3.24}$$

The quantity $E^{(2)}[\delta n(\mathbf{r})]$ is greatly simplified by retaining the monopole term in the radial expansion of the atom-centered density fluctuations written as:

$$\delta n_i(\mathbf{r}) \approx \Delta q_i \, n_i\left(|\mathbf{r} - \mathbf{R}_i|\right), \tag{3.25}$$

where n_i is the normalized atomic charge density, and $\Delta q_i = q_i - q^0_i$ is the deviation of the atomic charge from the neutral atom, which is obtained well using Mulliken charge analysis consisting a simple projection of the eigenstates on the local orbitals as [77]:

$$\Delta q_i = \sum_k n_k \sum_{\mu \in i} \sum_\nu \mathrm{Re}\left[c^*_{k\mu} c_{k\nu} S_{\mu\nu}\right] - q^0_i. \tag{3.26}$$

Thus, the second order correction can be written as:

$$E^{(2)} = \sum_{i,j} \delta q_i \, \Delta q_j \, \gamma_{ij}, \tag{3.27}$$

where γ_{ij} is defined as:

$$\gamma_{ij} = \int \int \Gamma[\mathbf{r}, \mathbf{r}', n^0] \, n_i(\mathbf{r}') \, n_j(\mathbf{r}) \, d\mathbf{r}' \, d\mathbf{r}. \tag{3.28}$$

In further simplifications of the exchange-correlation contribution within the LDA, the term $\Gamma\left[\mathbf{r}, \mathbf{r}', n^0\right]$ becomes the usual *Green's function* of the Coulomb potential, $1/\left|\mathbf{r} - \mathbf{r}'\right|$, with vanishing boundary conditions at infinity. In standard DFTB, γ_{ij} is approximated by the *Hubbard parameters* given by the first derivation of the atomic energy with respect to the electronic occupation [28].

Applying the variational principle to the energy functional of Eq. 3.21, and using Eqs. 3.26 and 3.27, the modified Hamiltonian for the Kohn-Sham equations is obtained as follows:

$$\mathcal{H}_{\mu\nu} = \mathcal{H}^0_{\mu\nu} + \frac{1}{2} \mathcal{S}_{\mu\nu} \sum_l \left(\gamma_{il} + \gamma_{jl}\right) \Delta q_l \qquad \forall \mu \in i \quad \nu \in j. \qquad (3.29)$$

Based on the previous discussion, due to dependency of the atomic charge and wave function on each other, a self-consistent procedure is required to solve Eq. 3.29.

3.5. Setup for the quantum transport problem

According to the Landauer theory (see Sec. 2.4.1), the *contacts* must be considered besides the *device region* in the electron transport description. Thus, the type of systems under study is subdivided into two important parts, as shown in Fig. 3.1:

- the contacts, C_1 and C_2,
- the device region, D.

The contacts represent semi-infinite leads ending at the device region with an assumption that their properties coincide with those of bulk systems, and no constraint is imposed on the dimensionality, transverse size, and transverse shape of the leads. They can be one-dimensional atomic chains, two-dimensional planar atomic strips, or three-dimensional wires of arbitrary cross-section. In order to ensure that, the regions C_1 and C_2 are considered to be bulk-like and a portion of surfaces of conducting leads, S_1 and S_2, is included in the device region, as shown in Fig. 3.1. The device region can be any kind of atoms collection, such as the active part of an inorganic device, a single molecule, or a metallic connective neck, representing a nanoscale construction. Therefore, the lead-device-lead assembly could represent an STM junction, with or without an adsorbate, or the sample may be an insulating barrier. Device and leads may all have the same uniform cross-section if the lead-device-lead system constitutes a single continuous piece of a wire with uniform thickness.

The only definite assumption that is made about the structure of the system is that far away from the sample region, each lead is a perfect defect-free, crystalline conductor with a defined unit cell. It is assumed that at any instant in time, the electrons in the
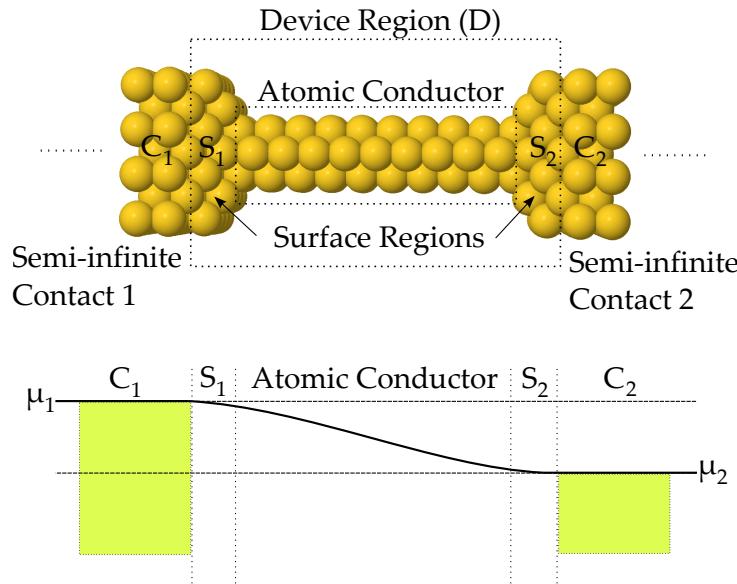
Figure 3.1.: Schematic view of a two-terminal conductor: the semi-infinite contacts ($C_{1/2}$) and the device region made up of the surface regions ($S_{1/2}$) and the atomic conductor sandwiched in between under non-equilibrium condition shown in the potential diagram. Deep in the contacts, average potential (thick line) is assumed to be constant ($\mu_{1/2}$) dropping in the device region and joining smoothly to the bulk values along the surface regions.

system see a frozen, static set of atomic positions. In other words, only elastic electron scattering is allowed. The justification for this approximation is that in many cases the inelastic electron mean free path is much longer than the typical dimension of the sample region. Thus, as far as the motion of the electrons in that region is concerned, the electron-phonon scattering is ignored.

The next assumption is that at infinity each lead is connected through a smooth contact to a macroscopic conductor as reservoir. Electrons in reservoirs are supposed to be in thermodynamic equilibrium, and the state occupation is described by the Fermi distribution function. Last assumption requires that the conducting bridge must offer the largest source of resistance to the flowing current. Under this condition, the potential drops across the device region, whilst the contacting leads are in equilibrium at two different constant potentials, as shown in Fig. 3.1. The applied bias, V_b, affects the Fermi distribution of one reservoir with respect to the other. The electrochemical potential of reservoir 2 is lowered relative to that of reservoir 1 by an amount $-eV_b$, such that $\mu_2 = \mu_1 - eV_b$. Each reservoir injects electrons into the respective lead, resulting in a net flow of electrons from lead 1 into lead 2. The bias voltage difference can be sustained by an external battery of voltage V_b. Because of the sign convention of the electronic charge, the application of a positive bias to a contact corresponds to a lower-

ing in energy by an amount $-eV_b$. In this respect, the mesoscopic system plays the role of a large resistance in analogy to conventional electronics.

3.5.1. The open boundary condition

Only an open system, which has the traveling eigenstates, is able to carry the net current. In the electron transport problem, appropriate open boundary conditions are required to be employed.

Injecting electrons from reservoirs in the identical states, *scattering states*, occurs according to the Fermi statistics. The scattering theory describes these scattering states, which mathematically yield the transmission probability associated to the current flowing through the device. To achieve this, among several existed techniques (e.g., transfer matrix [79], its generalizations, and Green's function approaches [14, 30]), the Green's function techniques extended to the *statistical non-equilibrium theory* is used in the present work. This approach is described in details in the following.

3.6. The Green's function technique

In order to construct the scattering states, open boundary conditions are applied in the Kohn-Sham equations (see Sec. 3.3.2) within the Green's function formalism. Deep in the leads, the propagating states are *Bloch's waves* due to the periodic boundary condition [3]. The waves are scattered at the lead-device interface dividing into the reflected and transmitted parts. The Hamiltonian of the entire system is written as:

$$\mathcal{H} = \mathcal{H}_D + \mathcal{H}_1 + \mathcal{H}_2 + \mathcal{V}, \tag{3.30}$$

where $\mathcal{H}_D$, $\mathcal{H}_1$, and $\mathcal{H}_2$ are the Hamiltonian of the device, the first contact, and the second contact, respectively. $\mathcal{V}$ denotes the Hamiltonian coupling the device region to the contacts, which can be treated as a perturbation.

The relationship between scattering states can be expressed in terms of the *Lippmann-Schwinger equation* [80] given by:

$$\left| \psi_1 \right\rangle = \left| \phi_1 \right\rangle + \mathcal{G}^r \mathcal{V} \left| \phi_1 \right\rangle, \tag{3.31}$$

where $\mathcal{G}^r$ is the *retarded Green's function* of the system linking the exact scattering states, $\left| \psi_1 \right\rangle$, to the unperturbed states, $\left| \phi_1 \right\rangle$. The states $\left| \psi_1 \right\rangle$ represent the states originating deep in the lead 1 and propagate from lead 1 to 2. Similarly, one can define the propagating states from lead 2 to 1 as $\left| \psi_2 \right\rangle$.

The Green's function of the system is constructed exploiting the *Dyson's equation* and by constructing the appropriate contact self-energies [14]. Assuming that contacts do not interact directly, the Hamiltonian of the whole two-terminal system in form of the TB block matrix is written as:

$$\mathcal{H} = \begin{pmatrix} \mathcal{H}_D & \mathcal{V}_{D1} & \mathcal{V}_{D2} \\ \mathcal{V}_{D1}^\dagger & \mathcal{H}_1 & 0 \\ \mathcal{V}_{D2}^\dagger & 0 & \mathcal{H}_2 \end{pmatrix}. \tag{3.32}$$

The Green's operator is defined by the usual relation $(E - \mathcal{H})\, \mathcal{G} = 1$. In order to have a direct relationship between the Green's function matrices and the density matrix, the dual basis is defined in the form of $\langle \phi_\mu \,|\, \phi_\nu \rangle = \delta_{\mu\nu}$. In this way, the Green's function is expanded in terms of the local basis sets as:

$$G^r(\mathbf{r}, \mathbf{r}', E) = \sum_{\mu\nu} G^r_{\mu\nu}\, \phi_\mu(\mathbf{r})\, \phi_\nu^*(\mathbf{r}'), \tag{3.33}$$

where the matrix G^r satisfies the matrix equation $\left[(E + i\delta)\mathcal{S} - \mathcal{H}\right] \times G^r = \mathcal{I}$, and the $G^r_{\mu\nu}(E)$ is written as:

$$G^r_{\mu\nu}(E) = \sum_k \frac{c_{k\mu}\, c_{k\nu}^*}{E - E_k - i\delta}, \tag{3.34}$$

where $\mathcal{I}$ cites the identity matrix.

The complete Green's function of the system can be expressed as [14]:

$$G^r_D = \left[(E + i\delta)\mathcal{S}_D - \mathcal{H}_D - \Sigma^r \right]^{-1}, \tag{3.35}$$

where Σ^r stands for the *total self-energy of the two contacts* and plays the role of an embedding potential given by:

$$\Sigma^{r,a}_\alpha = \left[(E + i\delta)\mathcal{S}_{D\alpha} - \mathcal{V}_{D\alpha} \right] g^{r,a}_\alpha \left[(E + i\delta)\mathcal{S}^\dagger_{D\alpha} - \mathcal{V}^\dagger_{D\alpha} \right], \tag{3.36}$$

where $g^{r,a}_\alpha$ defines the retarded (r) and the advanced (a) Green's functions related to the Hamiltonian of the contact α as:

$$g^{r,a}_\alpha = \left[(E \pm i\delta)\mathcal{S}_\alpha - \mathcal{H}_\alpha \right]^{-1}. \tag{3.37}$$

The self-energy can be calculated easily by exploiting the fact that the Hamiltonian describing the interaction between the device region and contacts involves a *finite number of atoms close to the junctions*. Therefore, in the matrix product of Eq. 3.36, only the matrix block of the contact Green's function close to the interface needs to be evaluated. This so-called *surface Green's function* can be calculated using for example the *decimation technique*, which is a powerful recursive algorithm suitable for the TB matrix representations [31].

3.6.1. The terminal currents

In order to determine the net current flowing across the device, the operator $\mathcal{J}_S$ as the *total electron current* through the surface S is defined:

$$\mathcal{J}_S = \frac{e}{i\hbar} \sum_{n' \in L, n \in R} \mathcal{J}_{n',n}, \tag{3.38}$$

where L and R designate the regions to the left and to the right of surface S, respectively, and $\mathcal{J}_{nn'}$ is the current flowing from the site n into the site n'. Expressing in the positional basis set, $\mathcal{J}_S$ contains only a finite number of terms namely the terms that involve sites bonded across the surface S by the TB Hamiltonian.

The observed current can be calculated as a statistical expectation value, which is obtained by evaluating the trace of the current operator with an appropriate density matrix:

$$I_{n'n} = \text{Tr} \left[\mathcal{J}_{n'n} \rho(V_b) \right] \tag{3.39}$$

with:

$$\mathcal{J}_S = \text{Tr} \left[\mathcal{J}_s \rho(V_b) \right], \tag{3.40}$$

where V_b denotes the bias voltage.

According to the scattering theory discussed in Sec. 3.6, the states originating deep in the contacts are in thermodynamical equilibrium with chemical potentials of μ_1 and μ_2 and populate following the Fermi distribution functions $f_1(E)$ and $f_2(E)$. It is assumed that the states traveling from lead 1 into 2, $\left|\psi_1\right\rangle$, are reflected only once through the lead 2 or the lead-reservoir contact. Similarly, this is assumed for the traveling states from lead 2 into 1, $\left|\psi_2\right\rangle$. This assumption allows to define the unique chemical potential of μ_1 for all the waves injected from lead 1 and the chemical potential μ_2 for injected waves from lead 2. Consequently, the density operator in the lead-device-lead setup can be written as:

$$\rho(V_b) = \int \left[f_1(E) D_1(E) + f_2(E) D_2(E) \right] dE, \tag{3.41}$$

where $D_1(E)$ and $D_2(E)$ are the *partial density operators* with the states incoming from lead 1 and lead 2, respectively given as follows:

$$D_1(E) = \sum_1 \left|\psi_1\right\rangle \delta(E - E_1) \left\langle\psi_1\right| \tag{3.42}$$

and

$$D_2(E) = \sum_2 \left|\psi_2\right\rangle \delta(E - E_2) \left\langle\psi_2\right|. \tag{3.43}$$

The total density of states, $D(E) = D_1(E) + D_2(E)$, is related to the system Green's function as:

$$D(E) = \frac{i}{2\pi}\left[\mathcal{G}^r - \mathcal{G}^a\right],\tag{3.44}$$

where $\mathcal{G}^r$ and $\mathcal{G}^a$ are the *retarded* and the *advanced Green's functions*, respectively.

The net current along the device is zero under zero bias limitation, and Eqs. 3.39 and 3.40 can be rewritten as follows:

$$I_{n'n} = \int \left[f_1(E) - f_2(E)\right] \mathrm{Tr}\left[\mathcal{J}_{n'n} D_1(E)\right] \, \mathrm{d}E \tag{3.45}$$

and

$$I_S = \int \left[f_1(E) - f_2(E)\right] \mathrm{Tr}\left[\mathcal{J}_S D_1(E)\right] \, \mathrm{d}E,\tag{3.46}$$

where I_S is the *surface current*, and S can be any arbitrary surface cutting the device region due to the current continuity. Based on the relationship of [81]:

$$\mathrm{Tr}\left[\mathcal{J}_S D_1(E)\right] = \frac{e}{h}\,\mathrm{Tr}\left[\Gamma_2\,\mathcal{G}_D^r\,\Gamma_1\,\mathcal{G}_D^a\right] = \frac{e}{h}\,\mathrm{Tr}\left[\Gamma_1\,\mathcal{G}_D^r\,\Gamma_2\,\mathcal{G}_D^a\right],\tag{3.47}$$

where $\Gamma_{1,2}$ are defined as:

$$\Gamma_\alpha = i\left[\Sigma_\alpha^r - \Sigma_\alpha^a\right],\tag{3.48}$$

the Eq. 3.40 becomes:

$$I = \frac{2e}{h}\int \mathrm{Tr}\left[\Gamma_1\mathcal{G}_D^r\Gamma_2\mathcal{G}_D^a\right]\left[f_1(E) - f_2(E)\right]\,\mathrm{d}E,\tag{3.49}$$

where Γ describes the coupling with the contact leads, and the advanced self-energy, Σ_α^a, is the *Hermitian conjugate* of the retarded self-energy, Σ_α^r. In Eq. 3.49, the factor of 2 denotes the *spin degeneracy*. The physical meaning of $\mathrm{Tr}\left[\Gamma_1\mathcal{G}_D^r\Gamma_2\mathcal{G}_D^a\right]$ can be interpreted as the transmission per energy channel between contacts 1 and 2. The Green's function $\mathcal{G}^a$ describes the dynamics of the electrons inside the device system taking the effect of the leads into account through the self-energy Σ_α^a. Eq. 3.49 recovers the standard Landauer formula as in Eq. 2.9, where the transmission function has the form of $\mathrm{Tr}\left[\Gamma_1\mathcal{G}_D^r\Gamma_2\mathcal{G}_D^a\right]$ and can be generalized for systems with more than two contacts.

3.7. The non-equilibrium Green's function technique

The obtained formalism for current was under the condition of zero-bias voltage. To overcome this restriction, generalization to much more involved theory is required being able to handle properties of the system driven out of equilibrium by an applied bias. This

is provided by the *non-equilibrium Green's function method* (NEGF method). Despite its mathematical complexity, the NEGF has gained a great popularity in recent years mostly because of the versatility and numerical stability of the method for quantum transport calculations, in contrast to the wave function or transfer matrix approaches.

The quantum transport theory within the NEGF formulation was introduced by KELDYSH [32], and developed by several authors [33, 34]. To achieve relevant quantities, the NEGF formalism is presented briefly. The time-ordered zero-temperature single-particle Green's function is defined as:

$$\mathcal{G}(x, t, x', t') = \frac{-i}{\hbar} \frac{\langle \psi_0 | \mathcal{T}[\psi_H(x, t) \psi_H^\dagger(x', t')] | \psi_0 \rangle}{\langle \psi_0 | \psi_0 \rangle}, \tag{3.50}$$

where $|\psi_0\rangle$ is the exact many-body ground-state, and ψ_H is the *Heisenberg representation of system wave function* [82]. $\mathcal{T}$ is the transition operator or simply $\mathcal{T}$-matrix. The central quantity in constructing the perturbation theory of the Green's function is the $\mathcal{S}$-matrix or scattering matrix introduced in Sec. 2.4.1. The general assumption is that at time $-\infty$, the ground-state is that of non-interacting particles, $|\phi_0\rangle$. The interactions are switched on adiabatically, and the wave function evolves into the interacting ground-state $|\psi_0\rangle = \mathcal{S}(0, -\infty)|\phi_0\rangle$ [83]. Similarly, $\langle \psi_0| = \langle \phi_0|\mathcal{S}(\infty, 0)$.
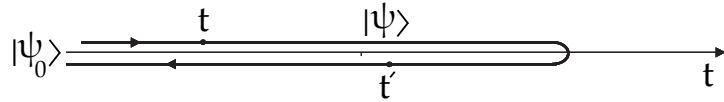

Figure 3.2.: Complex time contour used to define the NEGF [35].

Since under non-equilibrium conditions, there is no guarantee that the system returns to its initial state for asymptotically large time, a *contour-ordered Green's function* is introduced. The contour-ordered Green's function is defined similar to the Eq. 3.50, except that the time ordering operator is substituted by a contour ordering operator $\mathcal{T}_C$. The time contour, which is illustrated in Fig. 3.2, starts at an infinitely remote time and goes back to that time. The time contour can be divided into two branches (upper and lower), and the turn-point can be placed at any arbitrary time. When the two times t and t' of Eq. 3.50 fall in the same time-branch, the quantities of the standard equilibrium theory are recovered. When the two times fall in opposite branches, the time of the lower branch will always be later with respect to the time of the upper branch along the contour, and the correlation function as:

$$\mathcal{G}^<(\mathbf{r}, t, \mathbf{r}', t') = i \langle \psi_0 | \psi_H(\mathbf{r}, t) \psi_H^\dagger(\mathbf{r}', t') | \psi_0 \rangle \tag{3.51}$$

is obtained. The charge density, $n(\mathbf{r}, t)$, and the current density, $j(\mathbf{r}, t)$ can be obtained in terms of $\mathcal{G}^r(\mathbf{r}, t, \mathbf{r}', t')$ as:

$$n(\mathbf{r}, t) = -i\mathcal{G}^<(\mathbf{r}, t, \mathbf{r}', t') \tag{3.52}$$

and

$$j(\mathbf{r}, t) \; = \; \lim_{\mathbf{r}' \to \mathbf{r}} (\nabla' - \nabla) \, \mathcal{G}^<(\mathbf{r}, t, \mathbf{r}', t'). \tag{3.53}$$

In steady state, the Green's functions only depend on the time difference $t - t'$, which can be interpreted as *Fourier-transformed* to the energy. The density of occupied electronic states can be related to the quantity $\mathcal{G}^<(E)$ as:

$$n(\mathbf{r}) \; = \; \frac{1}{2\pi i} \int_{-\infty}^{+\infty} \mathcal{G}^<(\mathbf{r}, E) \, \mathrm{d}E. \tag{3.54}$$

Physically, $\mathcal{G}^<(E)$ and $\mathcal{G}^>(E)$ represent respectively the density of occupied and empty states. In steady state, the occupation depends on the scattering itself, which is controlled by the lesser self-energy, $\Sigma^<(E)$, known as the electron in-scattering function. The same function also controls the in-scattering of electrons from the leads into the device region. The dynamics of the occupation, due to the inelastic scattering processes from one energy channel to the other is provided by the KELDYSH-KADANOFF-BAYM equation (KKB equation) [84], also known as kinetic equation. Within the TB matrix representation, the KKB equation is expressed in terms of matrices [85]:

$$\mathcal{G}^<(E) \; = \; \mathcal{G}^r(E) \, \Sigma^<(E) \, \mathcal{G}^a(E), \tag{3.55}$$

where $\mathcal{G}^a = \mathcal{G}^{r\dagger}$. The lesser self-energy associated to the contacts is written as [81, 85]:

$$\Sigma^< \; = \; i f(E - \mu_1) \Gamma_1 + i f(E - \mu_2) \Gamma_2, \tag{3.56}$$

and the lesser Green's function of the system can be obtained by substituting Eq. 3.55 into Eq. 3.56 as:

$$\mathcal{G}^< \; = \; i f(E - \mu_1) \mathcal{G}^r \Gamma_1 \mathcal{G}^a + i f(E - \mu_2) \mathcal{G}^r \Gamma_2 \mathcal{G}^a. \tag{3.57}$$

The current flowing in the system can be computed starting from Eq. 3.53. It is convenient to define a current operator in terms of $\mathcal{G}^<(E)$, whose diagonal elements give the divergence of the current [14, 33, 85]:

$$I_{op}(\mathbf{r}, \mathbf{r}', E) \; = \; \frac{2e}{h} \left[\mathcal{G}^<(\mathbf{r}, \mathbf{r}', E) \mathcal{H}_D(\mathbf{r}') - \mathcal{H}_D(\mathbf{r}) \mathcal{G}^<(\mathbf{r}, \mathbf{r}', E) \right], \tag{3.58}$$

where factor of 2 is due to considering spin degenerate eigenstates. The trace of current operator gives the net outflow of current per unit energy across an imaginary surface enclosing the device region:

$$\mathrm{Tr}\left[I_{op}\right] \; = \; \int \nabla \cdot \mathcal{J}(\mathbf{r}, E) \, \mathrm{d}\mathbf{r}. \tag{3.59}$$

Using Eqs. 3.33, 3.57, and 3.58 as the TB representation of the Green's function matrix, the total outflow of current at a specific energy can be written as:

$$I_{tot} = -\frac{2e}{h} \, \text{Tr} \left[\Sigma^<(E) \left(\mathcal{G}^r(E) - \mathcal{G}^a(E) \right) - \mathcal{G}^<(E) \left(\Sigma^r(E) - \Sigma^a(E) \right) \right], \qquad (3.60)$$

which can also be rewritten in a more symmetric form using the relationships:

$$\mathcal{G}^r - \mathcal{G}^a = \mathcal{G}^> - \mathcal{G}^< \qquad (3.61)$$

and

$$\Sigma^r - \Sigma^a = \Sigma^> - \Sigma^<, \qquad (3.62)$$

the total current becomes:

$$I_{tot} = -\frac{2e}{h} \, \text{Tr} \left[\Sigma^<(E) \mathcal{G}^>(E) - \Sigma^>(E) \mathcal{G}^<(E) \right]. \qquad (3.63)$$

The quantity $\mathcal{G}^>$ is associated to the hole propagation, while $\mathcal{G}^<$ denotes the electronic propagation. Similarly, $\Sigma^>$ represents the in-scattering of holes into the device region, and $\Sigma^<$ indicates the in-scattering of electrons.

Using the expression for the total self-energy from Eq. 3.56, it is possible to identify the terminal current contribution to the total current:

$$I_\alpha(E) = \frac{2e}{h} \, \text{Tr} \left[\Sigma_\alpha^<(E) \mathcal{G}^>(E) - \Sigma_\alpha^>(E) \mathcal{G}^<(E) \right] \qquad (3.64)$$

Expression 3.64 represents the net inflow of current from the contact α into the device region. Current conservation ensures that when there are two contacts and no scattering, the net inflow of electrons at one contact balances the outflow at the other contact. Hence, the knowledge of one terminal current is sufficient to determine the total current flowing in the lead-device-lead system. In other words, Eq. 3.64 expresses a balance for incoming electrons from the contact α into the empty states distributed according to the $\mathcal{G}^>$ and the in-coming holes (equivalent to the outcoming electrons) into the filled states distributed according to the $\mathcal{G}^<$. It can be considered as a generalization to the quantum current expressed by the Landauer formalism, Eq. 3.49, to case of the non-equilibrium transport. When sources of incoherent scattering are presented, their effect must be consistently considered in the transport properties of the system under study. The natural sources of the incoherence transport in the Landauer formalism are the contacts, in which electrons relax the energy and lose the phase memory.

Although the NEGF formalism is very powerful and suited for the systematic treatment of the incoherence due to its ability to encompass the full many-body quantum theory, one should note that this formalism is not strictly necessary when the incoherent

processes are neglected. However, the theory provides a versatile formalism for the development of a completely consistent density functional theory description of the quantum transport in devices under bias condition. Indeed, such method provides the solution of the Kohn-Sham equations consistent with the open boundary conditions imposed by the semi-infinite contacts, and the definition of the density functional Hamiltonian consistent with the electronic density found within the device under non-equilibrium conditions.

3.7.1. Implementations of the NEGF method

Self-consistent formulations of the non-equilibrium quantum-transport problem have been implemented by several authors [85–91]. These implementations share most of the ingredients such as density functional theory for description of the electronic states and the *Landauer-Keldysh formalism* for transport. They differ on the details of the numerical implementations, resulting in different computational efficiencies and prediction power. In the local orbitals representation, the central quantity is the density matrix as:

$$\rho = \frac{1}{2\pi i} \int_{-\infty}^{+\infty} \mathcal{G}^{<}(E) \, \mathrm{d}E = \frac{1}{2\pi} \int_{-\infty}^{+\infty} \left[f_1 \mathcal{G}^r \Gamma_1 \mathcal{G}^a + f_2 \mathcal{G}^r \Gamma_2 \mathcal{G}^a \right] \mathrm{d}E. \qquad (3.65)$$

Since the integration along the real axis will be very close to the van Hove singularities of $\mathcal{G}^r$ and $\mathcal{G}^a$, which characterize the $\mathcal{G}^{<}$ via Eq. 3.55, it is convenient to manipulate the Eq. 3.65 to allow for a complex contour deformation [87, 88]. Eq. 3.65 is usually transformed by adding and subtracting $f_1 \mathcal{G}^r \Gamma_2 \mathcal{G}^a$ and using:

$$\mathcal{G}^r \left[\Gamma_1 + \Gamma_2 \right] \mathcal{G}^a = i \left[\mathcal{G}^r - \mathcal{G}^a \right] \qquad (3.66)$$

to obtain:

$$\rho = -\frac{1}{\pi} \int_{-\infty}^{+\infty} f_1(E) \, \mathrm{Im}\{\mathcal{G}^r(E)\} \, \mathrm{d}E + \frac{1}{2\pi} \int_{-\infty}^{+\infty} \left(f_2(E) - f_1(E) \right) \mathcal{G}^r \Gamma_2 \mathcal{G}^a \, \mathrm{d}E, \quad (3.67)$$

where the first term represents the usual equilibrium density matrix in terms of $\mathcal{G}^r$. Since the poles of $\mathcal{G}^r$ lie below the real axis, it is possible to perform the integration on the equivalent contour obtained by deformation, as shown in Fig. 3.3. The integration contour can be deformed away from the real axis in the upper half-plane, where $\mathcal{G}^r$ does not have singularities [92].

In actual computations, the integration can start at an energy E_{low}, well-below the lowest eigenstate of the system, where the density of states vanishes. For zero temperature, the Fermi function is a step function, and the integration contour can stop at μ_1.
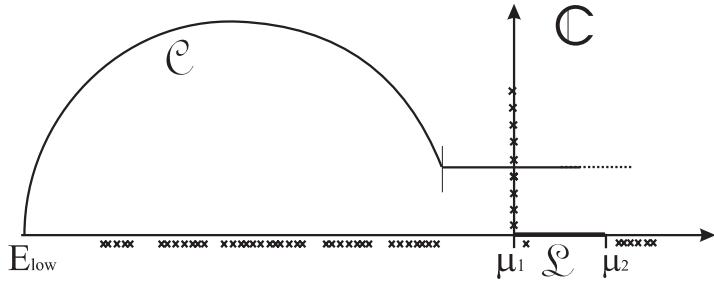
Figure 3.3.: Diagram showing the integration path in the complex plane needed to evaluate the non-equilibrium Green's function. The crosses below the real axis represent the poles of $G^r(z)$, and those on the imaginary axis the poles of the Fermi function [35].

For $T > 0$, it is also necessary to consider the poles of the Fermi function laying at the points $z_n = \mu_1 + i(1 + 2n)\pi k_B T$ [93]. Although the contour is deformed away from the real axis, a number of the additional residues, $G^r(z_n)$, must be included for a correct calculation [88].

The second integration depends on both G^r and G^a, and the path cannot be deformed in any way. However, the scheme above restricts the difficult part of the energy integration to a much smaller energy interval, whose extension depends on the applied bias, which is usually of the order of a few volts. This is much smaller than the energy band-width, which can be greater than 20 eV. The integration along the real axis should be performed by *Gaussian quadratures*. Ideally, a self-adaptive iteration should be invoked in order to reach a given degree of accuracy. Unfortunately, the evaluation of the Green's function particularly for large systems is not cheap. The complex contour integration usually requires about 20 points, and the real axis integration needs at least 10 points eV^{-1} [88]. However, this computation can easily be performed in parallel and has a nearly perfect linear scaling up to the evaluation of 2 points per processor. A rather delicate point is the calculation of the Fermi functions of the contact leads. In practice, it is better to compute the Fermi levels of the contacts for the device at equilibrium directly with Eq. 3.67 by imposing the condition of charge neutrality for the device. The self-consistent procedure can be summarized in the diagram of Fig. 3.4.

The density matrix can be used to compute the real-space charge density, which is used to update the density functional Hamiltonian. This step is accomplished by solving for the Hartree potential (electrostatic potential) usually obtained as a solution of the Poisson equation, which needs to be solved with appropriate boundary conditions given by the contact potentials. The open boundary conditions for the Kohn-Sham potential can be solved by making the observation that deep inside a solid the Kohn-Sham potential approaches the bulk potential. This fact leads to the screening approximation, which provides natural boundary conditions for the potential of the open system. There-

```
┌─────────────────────────┐
│  precalculate the       │
│  bulk Hamiltonians      │
│  of contacts            │
└─────────────────────────┘

        ┌─────────────────────────┐
        │  guess input density    │
        └─────────────────────────┘

              ┌─────────────────────────────┐
              │  solve the Poisson equation │
              │  with the proper boundary   │
              │  conditions for the external│
              │  potential, resulting the   │
              │  Hartree potential          │
              └─────────────────────────────┘

┌──────────────────────┐   ┌─────────────────────────┐
│  self-consistent loop│   │  Hartree potential + XC │
└──────────────────────┘   └─────────────────────────┘

              ┌─────────────────────────────┐
              │  compute the Hamiltonian    │
              │  of the device and load the │
              │  contact Hamiltonians       │
              └─────────────────────────────┘

              ┌─────────────────────────────┐
              │  solve for the NEGF of the  │
              │  system and compute the     │
              │  density matrix             │
              └─────────────────────────────┘
```

Figure 3.4.: The self-consistent loop for the solution of the non-equilibrium transport problem [35].

fore, the Kohn-Sham potential should match the bulk potential at some planes placed sufficiently deep inside the electrodes. The matching planes coincide with the interfaces between contacts and the device region have been described in Fig. 3.1. The choice of how deep to place such planes should be checked for converged results. This criterion introduces some computational difficulties, since in a well-screening metal the matching plane can place just after the first two- or three-atomic layers. However, in a poorly screening material a substantial portion of contact surface needs to be simulated.

Chapter 4.

gDFTB: A Tool for the NEGF Density Functional Tight-Binding Formalism

4.1. Introduction

In the present chapter, the latest developments of approach to quantum transport calculations based on the DFTB scheme is reported. This approach, named as gDFTB, has been extended to the non-equilibrium Green's function theory for the computation of the electronic transport in open devices under an external bias voltage.

In order to calculate the quantum electronic states of copper and gold structures as big as what proposed in this study (i.e., hundreds atoms), a semi-empirical method is necessary to produce results within a reasonable time. Using gDFTB tool gives an option to achieve this purpose through the empirical TB formalism. In other words, the Slater-Koster parameters as the initial requirements must be prepared [37]. One should notice that such a TB calculation and its results clearly depend on the parametrization scheme, so the transferability to different systems is rather limited.

The great advantage of the Green's function technique could be treating the coherent and incoherent transport within a unified mathematical framework. But the major advances presented by gDFTB consist in the implementation of an efficient *block-iterative algorithm* to speed up the Green's function calculations, the *possibility to solve the self-consistent transport problem*, and the implementation of the *local Dirichlet boundary conditions*. Furthermore, the gDFTB gives an efficient simulation tool to compute the electronic transport in organic and inorganic molecular-scale devices and can allow very large systems to be treated. Indeed, the gDFTB is a technique designed for applications in nanotechnology; applications that are pertinent to systems having components that are both intrinsically molecular in nature, requiring treatment by quantum chemical techniques, and intrinsically macroscopic in nature, requiring treatment of integrated solid state electronics [89, 94].

This chapter is organized as follows: the Poisson solver used to calculate the Hartree potential in the device region is described in Sec. 4.2. The Slater-Koster parameterization used in TB model is given in Sec. 4.3. The block-iterative scheme used to make the Green's functions computationally efficient is illustrated in Sec. 4.4. A test case to compare gDFTB results with other theoretical and experimental results is presented in Sec. 4.4.1. The presented chapter follows closely a review by A. Pecchia et al. [36], the author of gDFTB simulator.

4.2. The Poisson equation

As mentioned in Sec. 3.3.2, the Hartree potential needed for the self-consistent iteration of the Kohn-Sham equations is computed by solving the Poisson equation with appropriate boundary conditions imposed by the contact potentials. The total electronic density, $n(\mathbf{r})$, can be split into a reference density of neutral atoms and a density fluctuation as:

$$n(\mathbf{r}) = \sum_i \left[n_i^0(\mathbf{r}) + F_{00}^i(\mathbf{r}) \Delta q_i \right], \tag{4.1}$$

where $n_i^0(\mathbf{r})$ indicates the atomic reference density, $F_{00}^i(\mathbf{r})$ is the *spherical s-like radial function*, and Δq_i represents the *Mulliken charges* [77]. The Poisson equation for the mean field electrostatic potential is written as:

$$\nabla^2 V = 4\pi \sum_i \left[n_i^0(\mathbf{r}) + F_{00}^i(\mathbf{r}) \Delta q_i \right] + \textit{boundary conditions}. \tag{4.2}$$

In DFTB approach, the self-consistent potential is related to the electronic density fluctuations, whereas the effective potential, V^0, corresponding to the reference charge density is included in $\mathcal{H}^0$ [29, 95]. By linearity, the Eq. 4.2 is split into two equations: one part corresponds for the reference density and the other for the *self-consistent correction* written as:

$$\nabla^2 V_{el}^{(1)} = 4\pi \sum_i F_{00}^i(\mathbf{r}) \Delta q_i. \tag{4.3}$$

Using the common boundary condition, which is vanishing the potential at infinity, the Eq. 4.3 is solved, and the Hartree potential is obtained as:

$$V_{el}^{(1)}(\mathbf{r}) = \sum_i \Delta q_i \int \frac{F_{00}^i(\mathbf{r}')}{\left\| \mathbf{r} - \mathbf{r}' \right\|} \, d\mathbf{r}'. \tag{4.4}$$

The Hartree potential can be projected on the atom centers using:

$$V_j = \int V_{el}^{(1)}(\mathbf{r}) \, F_{00}^j(\mathbf{r}) \, d\mathbf{r}. \tag{4.5}$$

In gDFTB, Eq. 4.3 is solved with the boundary conditions arising from the natural requirement that deep inside contacts, the effective potential for the Kohn-Sham equations must correspond to the bulk electrochemical potentials. Hence, at the boundaries between the device region and contacts, the potential must match the intrinsic effective bulk potential, which originates from any equilibrium charge density shifted by the applied bias. At the device-contact interfaces, C_α/S_α, the potential must satisfy the relation:

$$V_{S_\alpha}^{(1)}(\mathbf{r})\big|_{C_\alpha/S_\alpha} \; = \; V_{C_\alpha,bulk}^{(1)}(\mathbf{r})\big|_{C_\alpha/S_\alpha} \; + \; \Delta V_\alpha, \tag{4.6}$$

where ΔV_α is the external potential applied to the contact α.

The decoupling of Eq. 4.2 is actually a good approximation, since the reference density is taken as that of the *neutral atoms* and therefore is canceling with the ionic charges. On the contrary, the excess density produces a *long-range Coulomb field*, that should respect the boundary conditions imposed by the device. For instance, the charge accumulated on the contact surface must be consistent with the applied bias voltage.

Within the gDFTB approach, the Poisson equation is solved in the *real space* using a three-dimensional multi-grid algorithm applied to a general linear, non-separable, and *elliptical partial differential equation* [96]. The Poisson equation is just a particular case of this kind of equations with the form of:

$$\sum_{i=x,y,z} c_{ii}(\mathbf{r})\,\partial_i^2 V(\mathbf{r}) \; + \; \sum_{i=x,y,z} c_i(\mathbf{r})\,\partial_i V(\mathbf{r}) \; + \; c(\mathbf{r})\,V(\mathbf{r}) \; = \; \rho(\mathbf{r}). \tag{4.7}$$

If the coefficients are taken such that at all the points of $\mathbf{r}$:

$$c_i(\mathbf{r}) = c(\mathbf{r}) = 0 \tag{4.8}$$

and

$$c_{ii}(\mathbf{r}) = -1/4\pi, \tag{4.9}$$

the Poisson equation is obtained in the *three-dimensional Poisson box*, in which the equation itself is discretized. The possibility of setting the coefficients to different values in different regions of the solution space allows to impose Dirichlet boundary conditions on the arbitrary shaped three-dimensional surfaces, such as planar or cylindrical contacts, and handle easily even four-terminal geometries.

The mesh is usually chosen as a trade-off between accuracy and computational speed. The usual spherically symmetric form used in the DFTB approach for the atomic charge density [28], gives quite smooth functions, and usually convergent results are obtained with a mesh spacing of 0.5 atomic units.

4.3. Slater-Koster parameterization for TB model

To manage the huge amount of carriers in cooper and gold structures under study, the empirical Slater-Koster parameterization is employed in TB model of the gDFTB (see Sec. 3.4). This method includes overlap terms and matrix elements that are not restricted to the first neighbors. Moreover, all the valance states are considered.

Within the two-center approximation, the Hamiltonian matrix element is written as:

$$\left\langle \phi_\mu(\mathbf{r}) \right| - \frac{1}{2}\nabla^2 + v_{eff}\big[n_\alpha(\mathbf{r})\big] + v_{eff}\big[n_\beta(\mathbf{r} - \mathbf{r}_0)\big] \left| \phi_\nu(\mathbf{r} - \mathbf{r}_0) \right\rangle \quad \mu \in \alpha \,, \; \nu \in \beta, \quad (4.10)$$

where n_α and n_β are atomic densities located in sites α and β, respectively, and v_{eff} denotes the effective potential introduced in Kohn-Sham equations. Similarly, the overlap matrix element is given by:

$$\left\langle \phi_\mu(\mathbf{r}) \,\middle|\, \phi_\nu(\mathbf{r} - \mathbf{r}_0) \right\rangle \quad \mu \in \alpha \,, \; \nu \in \beta. \quad (4.11)$$

For both Hamiltonian and overlap integrals, the direction of $\mathbf{r}_0$ is chosen to align the relevant orbitals μ and ν in the appropriate orientations for different kinds of bonding such as σ, π, δ, and etc.

In case of the copper Slater-Koster parameterization produced in Bremen (BCCMS),[1] the 5α exponents have been used in the potential superposition. In order to treat the exchange-correlation energy, a maximum order of 3 LDA of Perdew-Wang has been employed. The reference atomic configuration has been set to $3d\,4s$, that for gold Slater-Koster parameters developed in Rome (OLABs)[2] has been set to the configuration of $5d\,6s\,6p$. The repulsive potential of copper parameterization has been fitted to the dimer, whereas for gold has been fitted against the bulk calculations. For bulk copper the results based on mentioned parameterization are comparable to the experimental data of JONA [97]. The parameterization of gold has been applied to the small clusters with a certain degree of success [98].

4.4. The block-iterative algorithm

In the local basis representation, the Hamiltonian and overlap matrices have a sparse structure because of the short interatomic interactions. In a quasi-one-dimensional system, the atoms can be arranged in layers such that the matrices $\mathcal{H}$ and $\mathcal{S}$ take the block

---

[1]The copper Slater-Koster parameterization has been set by Prof. Frauenheim's group in the Bremen Center for Computational Materials Science (BCCMS): *www.bccms.uni-bremen.de*.

[2]The extended calculations on the gold Slater-Koster parameters has been performed by A. PECCHIA from OLAB research group at the Department of Electronics Engineering of the University of Rome *Tor Vergata*: *www.optolab.uniroma2.it*.

tridiagonal form represented in Fig. 4.1. The diagonal blocks can have different sizes, but must have all a square shape. The corresponding layers are called *principle layers* (PLs) and have the properties that the interaction of each PL is restricted to *two nearest neighbor PLs*. This structure is exploited by devising an efficient computation of the Green's function.
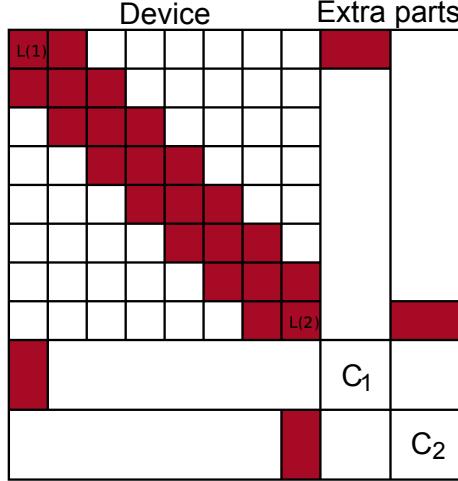

Figure 4.1.: Block tridiagonal structure of $\mathcal{H}$ and $\mathcal{S}$ for a quasi-one-dimensional system with two contacts assumed to interact with the first and the last PLs [36].

Indeed, the direct inversion of the whole Hamiltonian is an extremely time-consuming task in large structures. The equation defining the Green's function:

$$\sum_k \left(E\, \mathcal{S}_{i,k} - \mathcal{H}_{i,k} \right) \mathcal{G}_{k,j} = \delta_{ij} \tag{4.12}$$

can be written in terms of a tridiagonal Hamiltonian. The gDFTB defines conveniently the off-diagonal terms as:

$$T_{L,L+1} = E\, \mathcal{S}_{L,L+1} - \mathcal{H}_{L,L+1}. \tag{4.13}$$

In general, the Green's function does not preserve the block tridiagonal structure, but only sub-blocks, where the matrix $\mathcal{S}$ is non-vanishing, are actually needed to compute the Mulliken charges in Eq. 3.26.

The device comprised N layers is interacting with two contacts. It is assumed that the contacts interact with the device at layer 1 and at layer N. As a preliminary step, the contact self-energies are computed according to expression:

$$\Sigma_\alpha = T_{L(\alpha),\alpha}\, g_{\alpha,\alpha}\, T_{\alpha,L(\alpha)}, \tag{4.14}$$

where $L(\alpha)$ is the layer of the device interacting with contact α, and $g_{\alpha,\alpha}$ is the *surface Green's function* of contact α. The latter is computed assuming that the contact Hamiltonian can also be represented in a block tridiagonal form with all diagonal blocks, and interactions are the same. The self-energies are added to the corresponding diagonal blocks of the Hamiltonian, $\mathcal{H}_{L(\alpha),L(\alpha)}$.

The first part of the iterative scheme consists of the computation of the surface partial Green's functions $g_{L,L}^R$, which are obtained by removing the interaction blocks $T_{L-1,L}$ and $T_{L,L-1}$. Similarly, $g_{L,L}^L$ are obtained by removing the interactions $T_{L,L+1}$ and $T_{L+1,L}$. In practice, $g_{L,L}^L$ are the exact surface Green's functions of a system cut at layer L interacting only with the left part of the system. Correspondingly, $g_{L,L}^R$ are the surface Green's functions of a system cut at layer L interacting only with the right part of the system. These Green's functions obey the following recursive relations:

$$g_{L,L}^R = \left[E\,\mathcal{S}_{L,L} - \mathcal{H}_{L,L} - T_{L,L+1}\,g_{L+1,L+1}^R\,T_{L+1,L}\right]^{-1} \tag{4.15}$$

and

$$g_{L,L}^L = \left[E\,\mathcal{S}_{L,L} - \mathcal{H}_{L,L} - T_{L,L-1}\,g_{L-1,L-1}^L\,T_{L-1,L}\right]^{-1}. \tag{4.16}$$

Surface Green's functions $g_{L,L}^R$ are computed by iterating upward, starting from layer N up to layer 1, whereas surface Green's functions $g_{L,L}^L$ are computed by iterating downward starting from layer 1.

In the present implementation, the surface partial Green's functions $g_{L,L}^R$ are computed, then computing the complete Green's functions iterating downward started from layer 1 is performed:

$$\mathcal{G}_{1,1} = \left[E\,\mathcal{S}_{1,1} - \mathcal{H}_{1,1} - \Sigma_{1,1} - T_{1,2}\,g_{2,2}^R\,T_{2,1}\right]^{-1}, \tag{4.17}$$

further, all subsequent layers down to N are considered by using:

$$\mathcal{G}_{L,L} = g_{L,L}^R + g_{L,L}^R\,T_{L,L-1}\,\mathcal{G}_{L-1,L-1}\,T_{L-1,L}\,g_{L,L}^R. \tag{4.18}$$

The off-diagonal blocks can be obtained from expressions:

$$\mathcal{G}_{L-1,L} = -\mathcal{G}_{L-1,L-1}\,T_{L-1,L}\,g_{L,L}^R \tag{4.19}$$

and

$$\mathcal{G}_{L,L-1} = -g_{L,L}^R\,T_{L,L-1}\,\mathcal{G}_{L-1,L-1}. \tag{4.20}$$

All the expressions derived so far are valid for $\mathcal{G}^r$ or $\mathcal{G}^a$, which are sufficient to compute the density matrix in equilibrium. In order to derive the correct expressions for the non-equilibrium case, the matrix multiplication in Eq. 3.55 is required to carry out explicitly. Only the tridiagonal blocks of the matrices $\mathcal{G}^{<,\alpha} = \mathcal{G}^r\,\Gamma_\alpha\,\mathcal{G}^a$ are needed written as:

$$\mathcal{G}_{L,L}^{<,\alpha} = \mathcal{G}_{L,L(\alpha)}^r\,\Gamma_\alpha\,\mathcal{G}_{L(\alpha),L}^a = \mathcal{G}_{L,L(\alpha)}^r\,\Gamma_\alpha\,\mathcal{G}_{L,L(\alpha)}^{r\dagger}, \tag{4.21}$$

$$\mathcal{G}^{<,\alpha}_{L-1,L} = \mathcal{G}^{r}_{L-1,L(\alpha)} \, \Gamma_\alpha \, \mathcal{G}^{a}_{L(\alpha),L} = \mathcal{G}^{r}_{L-1,L(\alpha)} \, \Gamma_\alpha \, \mathcal{G}^{r\dagger}_{L,L(\alpha)}, \tag{4.22}$$

and

$$\mathcal{G}^{<,\alpha}_{L,L-1} = \mathcal{G}^{r}_{L,L(\alpha)} \, \Gamma_\alpha \, \mathcal{G}^{a}_{L(\alpha),L-1} = \mathcal{G}^{r}_{L,L(\alpha)} \, \Gamma_\alpha \, \mathcal{G}^{r\dagger}_{L-1,L(\alpha)}. \tag{4.23}$$

This set of equations shows that the computation of $\mathcal{G}^{<,\alpha}_{L,L}$ requires the computation of the column-blocks $\mathcal{G}^{r}_{L,L(\alpha)}$ corresponding to the layer $L(\alpha)$. Referring back to Eq. 3.67, it is observed that for a system of N contacts, the computation of $N-1$ columns is needed. These column-blocks can be obtained using the recursive formula:

$$\mathcal{G}_{j,L(\alpha)} = -g^{R}_{j,j} \, T_{j,j-1} \, \mathcal{G}_{j-1,L(\alpha)}, \tag{4.24}$$

valid for $j > L(\alpha)$ and

$$\mathcal{G}_{j-1,L(\alpha)} = -g^{L}_{j-1,j-1} \, T_{j-1,j} \, \mathcal{G}_{j,L(\alpha)}, \tag{4.25}$$

valid for $j < L(\alpha)$.

A further complication in the computation of the Mulliken charges is the non-zero overlap between device and contact atoms. As a consequence of Eq. 3.26, the density matrix needs to be computed on extra blocks outside the device corresponding to the overlap between device and contacts, as shown in Fig. 4.1.

Concerning $\mathcal{G}^{r}$, the calculation of these blocks is simple and can be derived in analogy to the Eq. 4.19 as:

$$\mathcal{G}^{r}_{L(\alpha),\alpha} = -\mathcal{G}^{r}_{L(\alpha),L(\alpha)} \, T_{L(\alpha),\alpha} \, g^{r}_{\alpha,\alpha}. \tag{4.26}$$

With lengthy algebra, it is possible to obtain the general expressions:

$$\mathcal{G}^{<,\alpha}_{L(\alpha),\alpha} = -i\mathcal{G}^{r}_{L(\alpha),L(\alpha)} \, T_{L(\alpha),\alpha} \left(g^{r}_\alpha - g^{a}_\alpha \right) - \mathcal{G}^{r}_{L(\alpha),L(\alpha)} \, \Gamma_\alpha \, \mathcal{G}^{a}_{L(\alpha),L(\alpha)} \, T_{L(\alpha),\alpha} \, g^{a}_\alpha \tag{4.27}$$

and

$$\mathcal{G}^{<,\alpha}_{L(\beta),\beta} = -\mathcal{G}^{r}_{L(\beta),L(\alpha)} \, \Gamma_\alpha \, \mathcal{G}^{a}_{L(\alpha),L(\beta)} \, T_{L(\beta),\beta} \, g^{a}_\beta, \tag{4.28}$$

valid only for $\beta \neq \alpha$.

The direct inversion of Hamiltonian matrix scales as $O(N^3 m^3)$ in computational time and as $O(N^2 m^2)$ in memory load, where N represents the number of layers, and m is the layer size. On the other hand, the iterative scheme scales as $O(Nm^3)$ in computational time and as $O(Nm^2)$ in memory load. For calculations of nanowire, the iterative algorithm scales linearly with the wire length and cubically with the wire diameter both in computational time and memory load.

4.4.1. **Test case**

In order to test whether numerical calculations recover the theoretical expectations, the band structure of bulk copper has been calculated using the gDFTB simulator,[2] as demonstrated in Fig. 4.2a. The lowest energy level has a minimum at Γ point. The Fermi energy has been normalized to zero like the case presented in Fig. 4.2b, which describes the band structure of bulk copper calculated by two different theoretical approaches and compared with that of the experimental data (circles).
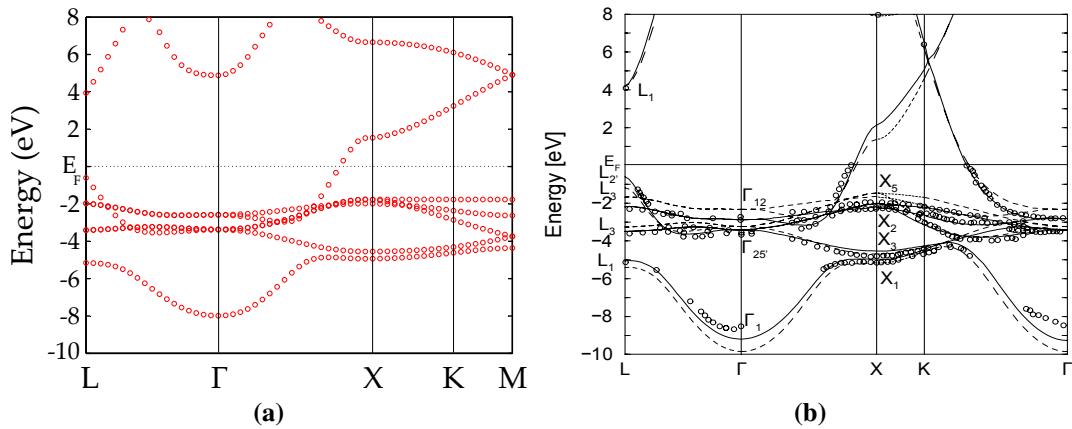
Figure 4.2.: (a) Bulk copper band structure calculated by gDFTB tool[2] and (b) Solid line: presents GW results for the bulk copper band structure compared with the DFT-LDA results (dashed line) and with the experimental data (circles) [99].

Following the energy levels through L–K directions in Fig. 4.2a and comparing to the corresponding levels in Fig. 4.2b denote a good agreement between the various approaches. In the band structure plotted in Fig. 4.2b, Marini et al. [99] have employed the *GW method* to compute self-energy corrections on top of ab-initio density functional theory, which has become a quite well-established technique giving energy levels generally in good agreement with experiments.

More examples of various applications of the gDFTB compared to experimental and theoretical results are presented in App. A.

Chapter 5.

Electronic Transport Properties of Metal Atomic Wires

5.1. Introduction

Metallic nanostructures generated with different techniques have received a great attention as building blocks for nanoelectronic devices because of wide variety of new phenomena that these tiny systems manifest. Two classes of metal nanostructures are considered in this work: atomic-sized nanowires (atomic wires) and single point contacts, upon the electron transport calculations governed by the geometry structure effects are based.

Although copper is the most commonly material used in electronics, less efforts both experimentally and theoretically have been dedicated to shed light on its electronic transport properties in mesoscopic range and especially at atomic scale. In the present chapter, theoretical analyses are performed on copper atomic wires to study the dependency of electronic transport properties on the geometry of structure. The same calculations are taken into account for gold atomic wires, as a well-studied structure due to the simplicity of conductance measurements, in order to compare the results with those of copper.

As mentioned in previous chapters, the used computational method is the non-equilibrium Green's function density functional tight-binding formalism by means of the gDFTB tool, where the idea of considering external bias voltage is taken into account by the non-equilibrium concept, and the DFTB formalism via empirical TB parameterization gives an efficient solution to handle the transport problem in metals with a huge number of carriers.

The chapter is outlined as follows: an introduction to atomic wire characteristics, possible fabrication techniques, and modeling for theoretical analyses is presented at the beginning. Sec. 5.3 proceeds with the geometry effects on the electron transport, including effects of atomic wire orientation, length, width, and non-mirrored electrodes,

individually. Furthermore, the results are compared with those of experimental and other theoretical techniques. Current-voltage characteristics of atomic contacts behave non-linearly in a certain range of the applied bias voltage, which is discussed widely in Sec. 5.4. The influence of temperature is studied in Sec. 5.5.

5.2. Concept of the atomic wire

The ultimate in miniaturization of computer circuitry would be to make circuit elements out of small assemblages of atoms or molecules. The first step on this road is to study the properties of atomic wires (i.e., short chains of atoms that conduct electricity between two contacts). Recent advances in the experimental techniques, such as *scanning tunneling microscopy* (STM) [5, 6], *mechanically controllable break junctions* (MCBJ) [7–9], and *transmission electron microscopy* (TEM) [10–12], make possible to fabricate wires with atomic scale. The scheme of atomic wires is modeled in analogy to experimental observations. In the following, fabrication techniques and modeling of atomic wires are presented.

5.2.1. Fabrication techniques

Although the fundamental application of the STM is the study of surface topography in the non-contact scanning mode, very thin metal wires are produced by the tip retracting from nanoindentation in STM. Recently, RODRIGUES et al. [11] have generated gold nanowires at atomic scale in situ in a *high resolution transmission electron microscopy* (HRTEM) to determine the structure by mechanical stretching. The procedure has been carried out by focusing the electron beam (current density 120 A/cm^2) on different sites of a self-supported metal thin film until the formation of a nanometric neck inside or between grains and then reducing the electron beam intensity (30 A/cm^2) to perform the image acquisition. They have used a polycrystalline gold film (5 nm thick, average grain size 50–100 nm) in order to generate nanowires with different elongation directions or formed between grains with different orientations.

Their observations indicate that during the final stretching steps just before rupture, gold nanowires are crystalline and free of defects at room temperature, and three possible atomic configurations of [100], [110], and [111] are merely observed for these structures. In [110] direction, atomic wires have a rod-like shape. In contrast, when the elongation is parallel to the [111] or [100] directions, constructions with bipyramidal shapes are distinguished. The recording of atomic resolution images is possible due to their slow elongation and long lifetime (the evolution from a few-atom-thick neck to rupture takes 1:30 min).
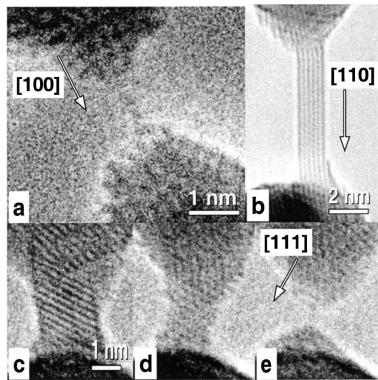
Figure 5.1: HRTEM images of gold atomic-sized nanowires: (a) [100] atom-chain nanowire; (b) rod-like [110] nanowire; (c)–(e) temporal evolution of a nanowire formed when the apexes are sliding: 0, 17:12, and 24:15 min, respectively. The atomic positions appear dark. [11].

The HRTEM images shown in Fig. 5.1 illustrate the atomic configuration of generated gold structures. The minimal cross-section of [110] nanowires is reported to be always larger than the one-atom-thick contacts allowed by [111] or [100], which is the subject of the next chapter.

In agreement with other reports, the gold contacts along [111] and [100] crystalline directions adopt chain structures with a length of two- to four-atoms and a bond distance of ~ 0.36 nm [10].

Several works have been done on metal atomic wires, while copper has not been studied in detail yet. One experimental study, which provides clear indication for the existence of pentagonal copper atomic wire with equilibrium conductance of $\sim 4.5 G_0$, has been reported by GONZÁLES et al. [13]. Their analysis based on a time resolved HRTEM of the copper atomic wire reveals that the wire structure adopts three configurations as reported for gold. The formation of rod-like wires has been observed for [100] and [110] directions, in contrast to [111] orientation, which exhibits a bipyramidal shape. The HRTEM images during the generation of copper atomic wires are shown in Fig. 5.2.
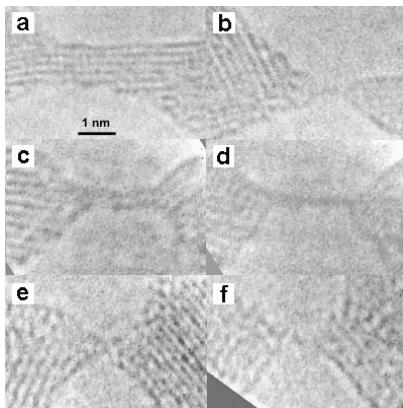
Figure 5.2: HRTEM images of the formation of copper atomic-sized nanowires along different crystallographic directions: (a) and (b) [100]; (c) and (d) [110]; (e) and (f) [111]. Note that suspended atom chains are formed just before rupturing for all three directions (b), (d), and (f) [13].

5.2.2. Geometry structure modeling

In this section, the modeled geometry structures of copper and gold atomic wires are explained in detail on the basis of the crystallographic properties of materials as well as the HRTEM observations. Note that *no attempt is made to optimize the geometries*.

As demonstrated in Fig. 3.1, geometries are considered growing from a central atom along a given crystallographic axis in the fcc lattice. After a certain number of layers (depending on the wire length) from the central atom, this structure, which plays role of the device region, is connected to the perfect fcc semi-infinite crystals acting as metallic electrodes (i.e., the device region is made from the same material as contacts). All lattice constants are assumed to be equal to the bulk constant obtained from experiments, which is 3.1469 Å for copper and 4.0782 Å for gold.

Fig. 5.3 illustrates the setup of a typical atomic wire split into the device region and contacts in [110] elongation direction. Some extra atoms are considered in the device region to reproduce the pyramidal shape at the connections found in the reality.
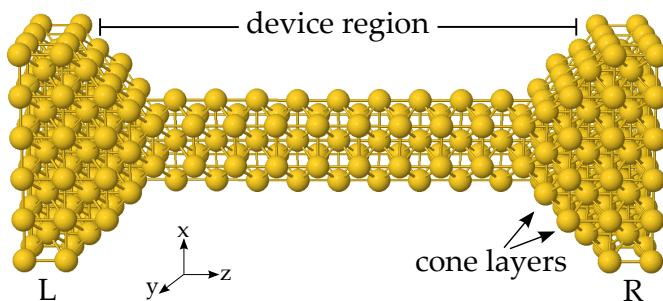
Figure 5.3.: Scheme of a typical atomic wire along [110] direction. L and R denote the left and right electrodes, respectively. The device region is connected to electrodes via two extra atomic layers forming a conical structures at the interfaces.

In [001] direction, the $5/4$ rod is modeled, in which the notation of the structure comes from the number of atoms contained in each atomic plane of the wire, as shown in detail in Fig. 5.4. Moreover, electrodes are mirrored in most models, except one non-mirrored case with electrodes shifted against each other to mimic the tension of metallic surface during experiment via STM technique, which is discussed in an individual section.

The HRTEM results show that compared to the other kinds of structures, the [110] atomic wires are rather brittle (i.e., they break when they are two- to three-atom-thick without forming atomic contacts). Therefore, [110] atomic wires with $2/2$, $4/3$, and $8/6$ rod-like configurations are considered. Due to their large aspect ratio, only the cross-sections of the rods are shown, and the side-views are left out, as illustrated in
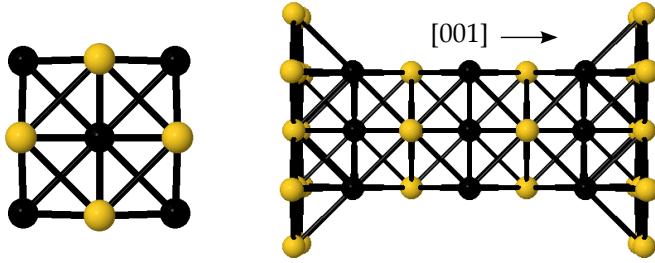
Figure 5.4.: Snapshot of an atomic configuration along the [001] direction showing the cross section (Left) and the side view (Right) of $5/4$ rod. Arrangement of atoms in two nearest neighbor faces shown in different colors determines the associated $5/4$ notation.

Fig. 5.5. The $4/3$ atomic wire is obtained by removing seven lines of atoms from the largest $8/6$ rod. In this manner, the $2/2$ is obtained by removing three lines of atoms from the $4/3$ rod. The distance between atomic layers is $a/2$ and $a\sqrt{2}/2$ in [001] and [110], respectively.
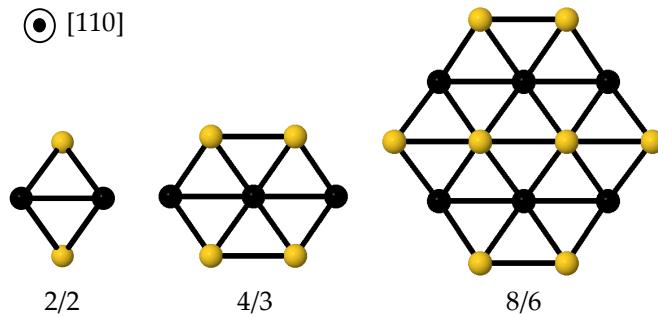
Figure 5.5.: The cross-section of [110] atomic wire with $2/2$, $4/3$, and $8/6$ rod-like configurations.

5.3. Geometry-dependent electron transport

Geometrical effects on metal resistivity have been studied extensively considering different scattering sources. For instance, ZHANG et al. [100] suggested a linear dependence of resistivity on $1/$width or $1/$(cross-sectional area) for copper nanowires with varying heights of 100, 150, and 200 nm. Questions, such as whether the linear relationship of resistivity and geometry characteristics can be generalized at all rise, again when the nanowires scale down to the atomic ranges, where the concept of resistivity is replaced by resistance (see Sec. 2.3.6). To answer such a question, various geometric features of the structures introduced before are analyzed individually.

5.3.1. Effect of atomic wire crystalline direction

The role of copper and gold atomic wires orientation on their electron transport behavior is studied for two preferred [001] $5/4$ and [110] $4/3$ rods. To rule out the contribution of other features, rods of almost the same lengths and widths are chosen. The $5/4$ [001] structure consists of 148 atoms at the device region and 116 atoms at the contacts. The $4/3$ [110] rod includes 117 atoms at the device region and 156 atoms at the contacts.

Employing the non-equilibrium based technique allows to carry out the transport out of zero bias limitation, in which at small bias voltages the Landauer formalism is employed. In this respect, electron transmission through each atomic wire is obtained via non-equilibrium Green's functions (see Sec. 3.6.1), and current is dependent on the external bias voltage via the transmission coefficient. Rewriting Eq. 3.49 yields:

$$I = \frac{2e}{h} \int T(E, V_b) \left(f_L(E) - f_R(E) \right) \, dE, \tag{5.1}$$

where $T(E, V_b)$ stands for the transmission coefficient at energy E, and bias voltage V_b, and $f_{L(R)}$ represent the Fermi distribution functions of the left and right electrodes.

(a) $V_b = 0.0$ (V)
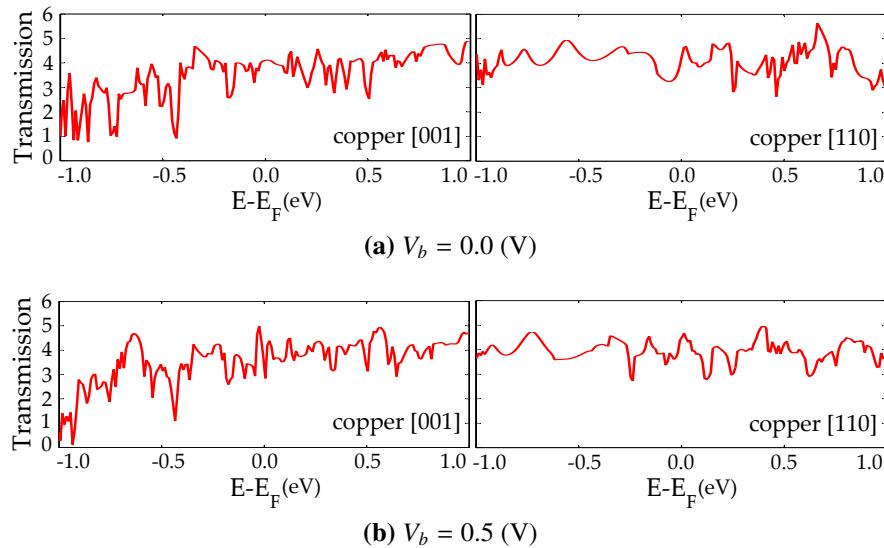
(b) $V_b = 0.5$ (V)

Figure 5.6.: Total transmission spectrum in terms of incident electron energy for copper atomic wire of [001] (Left) and [110] (Right) orientations calculated under (a) zero bias limitation and (b) an external bias voltage of $V_b = 0.5$ V. The Fermi energy is set to zero in all cases.

The total transmission spectrum for each orientation is presented in terms of incident electron energy calculated in presence of the bias voltage in order to ensure the energy and voltage functional nature of transmission. Fig. 5.6 illustrates transmission spectra at two bias voltages of 0.0 and 0.5 V. The influence of an external small voltage shifts the transmission peaks or produces new peaks.
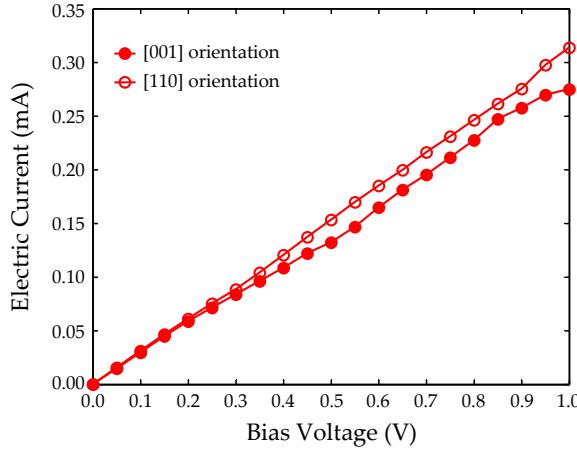
Figure 5.7.: Current-voltage curves of copper [001] (filled circles) and [110] (blank circles) rods.

Since the applied voltage across the leads is small compared to the Fermi energy of each structure, a small energy window is chosen to manifest this value. To simplify the comparison, the Fermi level of all structures is normalized to zero, and the transmission spectrum is plotted in an energy window ranging from -1 to 1 eV. The transmission peak is interpreted as the conducting channel: the higher peak around the Fermi level, the greater conduction value, and the more transmission peaks within the bias window, the higher the current. From transmission coefficients, the current-voltage characteristics are obtained, as shown in Fig. 5.7. The dependencies show that changing the growth orientation from [001] into [110] do not result to strong changes in the net current, especially at bias voltages smaller than 0.2 V the curves are coincident. In other words, the influence of the copper atomic wire orientation on the the transmission and current-voltage characteristics is very weak.

Table 5.1.: Comparison of conductance with respect to the atomic wire orientation.

Atomic wire	Orientation	Rod	Conductance (G_0)
copper	[001]	5/4	4.07
copper	[110]	4/3	4.06
gold	[001]	5/4	3.11
gold	[110]	4/3	4.70

The same height of transmission peaks in the visinity of the E_F at $V_b = 0$ V shown in Fig. 5.6a suggests the same equilibrium conductance for copper atomic wires of different orientations. Table 5.1 indicates the calculated conductance at the limit of zero bias voltage and at room temperature for each atomic wire.

(a) V_b = 0.0 (V)
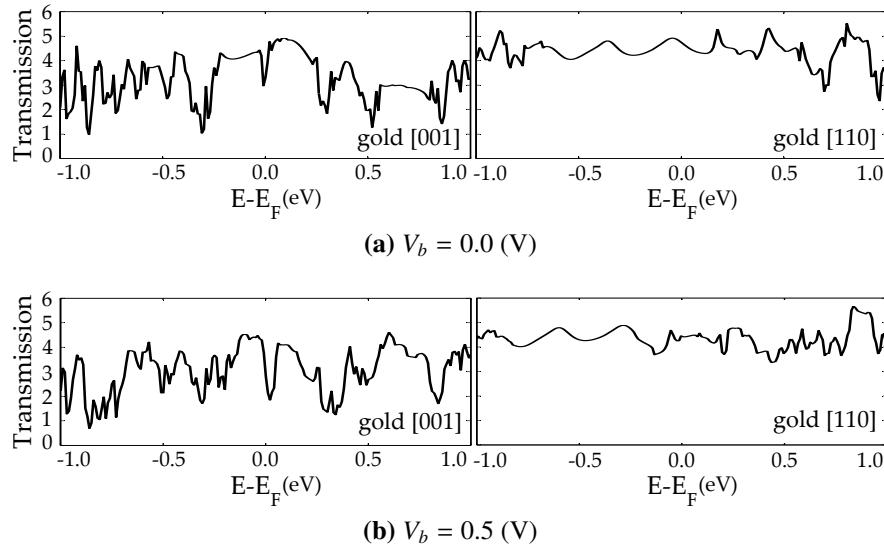
(b) V_b = 0.5 (V)

Figure 5.8.: Transmission coefficient in terms of the electron energy for gold atomic wire along [001] (Left) and [110] (Right) under (a) zero bias limitation and (b) external bias voltage of V_b = 0.5 V.

The orientation effect on the transmission of gold with similar geometries as in the case of copper is also tested. From the inspection of Fig. 5.8, it can be seen that resonance variations in the $5/4$ [001] rod occur abruptly, whereas in the case of $4/3$ [110] rod the dependence is much smoother around the E_F. Thus, a rather deviation of the current-voltage curves between these two cases is expected, as confirmed by Fig. 5.9.
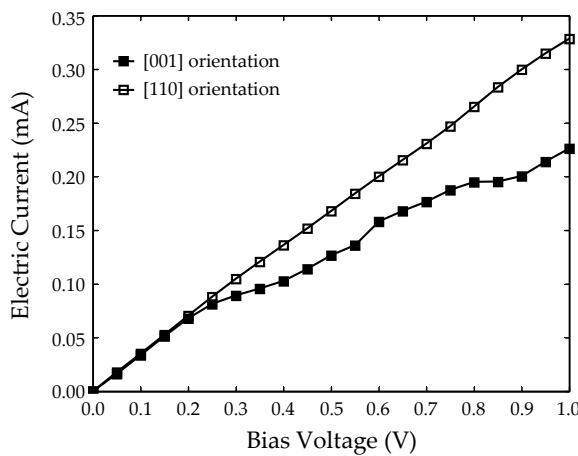
Figure 5.9.: Current-voltage characteristics of gold [001] (filled squares) and [110] (blank squares) rods.

Reduction in the number of peaks in case of the [001] geometry compared to the corresponding copper results in a decrease of the current-voltage characteristic at higher bias voltages, but coincidence of curves up to a bias voltage of 0.2 V is still preserved.

At the limit of zero bias voltage, the transmission spectrum of [110] shown in Fig. 5.8a (Right) has a peak higher than 4.5 at the Fermi energy, which implies the equilibrium conductance to take the value of $G(E_F) > 4.5G_0$, whereas in case of [001] shown in Fig. 5.8a (Left), the peak appears about 3. Accordingly, the conductance difference between the two orientations of gold atomic wires would be more than $1G_0$, as represented in Table. 5.1. The electron transport in copper atomic wire is influenced by turning the wire elongation direction from [001] into [110] weaker than in gold atomic wire. The gold $5/4$ [001] rod shows a non-linear current-voltage characteristic in contrast with the other structures, which is treated further individually.

5.3.2. Length effect

The length effect at atomic-scale wires is investigated considering the [001] $5/4$ rod. The configuration of the shortest atomic wire is formed by three (001) atomic planes. Hence, the device region length (i.e., the distance between electrodes) becomes $4a/2$, where a denotes the fcc lattice constant, and $a/2$ is chosen as the length step. The further wire is formed by adding one atomic plane to the previous geometry. In this regard, the lengths of the shortest and the longest atomic wires for copper become 0.72 and 2.17 nm, and for gold are 0.87 and 2.44 nm, respectively.
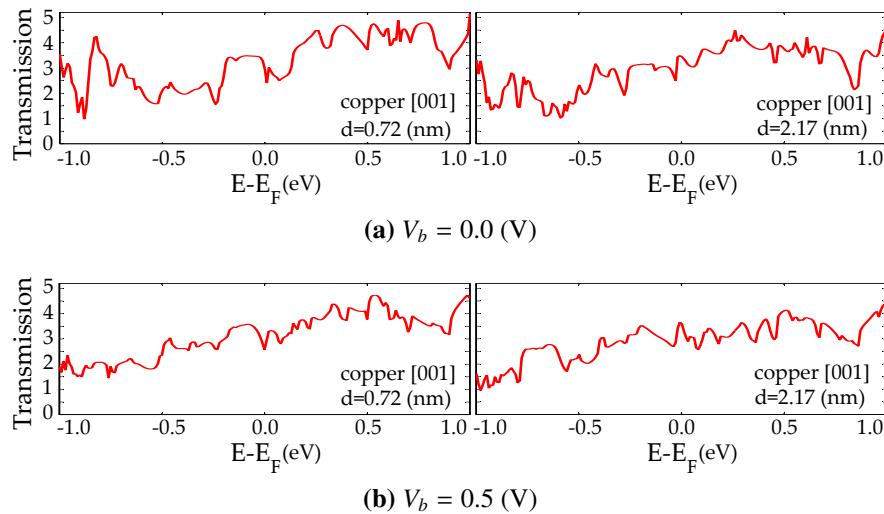
(a) $V_b = 0.0$ (V)

(b) $V_b = 0.5$ (V)

Figure 5.10.: Energy dependent total transmission of the shortest copper atomic wire (Left) and the longest one (Right) at (a) $V_b = 0.0$ V and (b) $V_b = 0.5$ V.

The total transmission spectra are demonstrated in Fig. 5.10 for the shortest and the longest copper atomic wires. The shortest wire shows the same transmission spectrum around the normalized Fermi energy as the longest wire. This behavior is not only special of zero bias limit, but it also occurs in presence of an external voltage, as shown
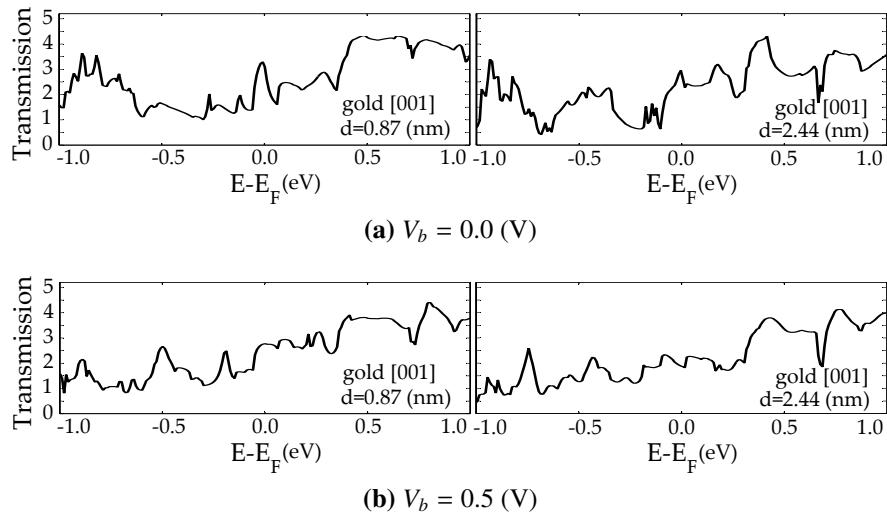
(a) $V_b = 0.0$ (V)

(b) $V_b = 0.5$ (V)

Figure 5.11.: Dependence of the total transmission of gold atomic wire on electron energy for the shortest (Left) and the longest (Right) $5/4$ [001] rod calculated at (a) $V_b = 0.0$ V and (b) $V_b = 0.5$ V.

in Fig. 5.10b. The total transmission spectra of gold atomic wires are presented in Fig. 5.11. A similar length effect is found for gold wires, for which the number of transmission peaks stays almost constant for different lengths. In comparison, the transmission coefficients of gold [001] rod are lower than those of copper, proving the higher conduction in copper $5/4$ [001].
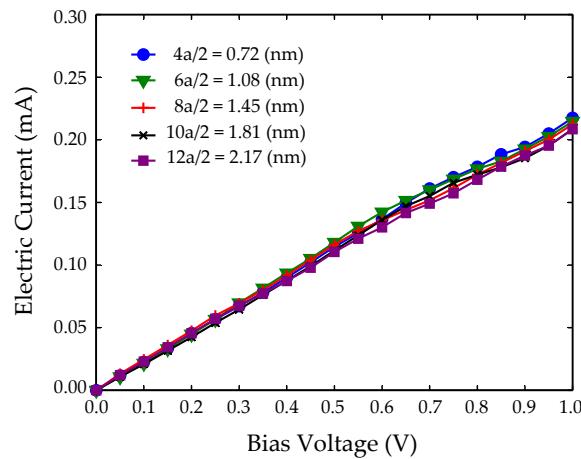
Figure 5.12.: Current-voltage characteristic of copper [001] rod for various lengths.

The current-voltage characteristic is determined based on the transmission probability for five lengths of 4, 6, 8, 10, and 12$a/2$ up to a bias voltage of 1.0 V, as shown in Fig. 5.12. From the same number of transmission peaks at each voltage, it is supposed to obtain the similar current curves. It is clearly seen that the deviation of current curves

from each other is very weak. This means that the current-voltage characteristic is length-independent in the ballistic transport regime.

The same calculations for gold are done to obtain the current-voltage characteristic, as shown in Fig. 5.13.
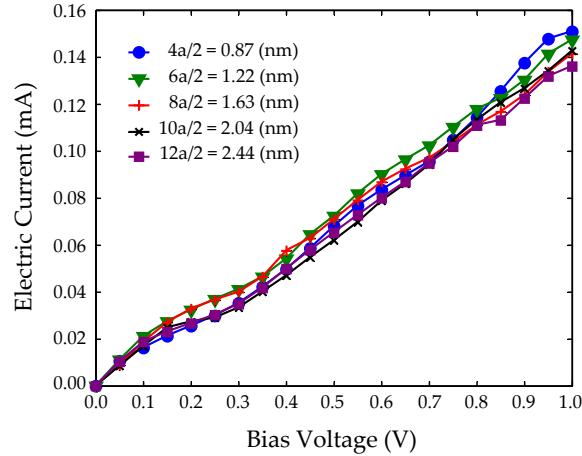
Figure 5.13.: Calculated current-voltage characteristic of gold [001] rod for various lengths.

To take a careful comparison, current-voltage characteristics of the longest copper and gold atomic wires are presented in Fig. 5.14.
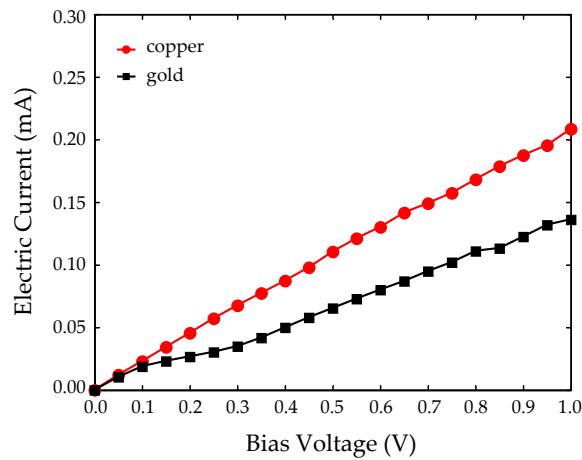
Figure 5.14.: Current-voltage characteristics of the longest copper and gold $5/4$ [001] rods.

The copper $5/4$ [001] structure shows higher values of current than gold, as predicted by the total transmission dependencies. For both elements, the length effect is very weak as far as the considered length is much smaller than the corresponding electron mean

free path. In other words, until ballistic transport regime is conserved, the length does not play significant role. Further circumstance justifying the length-independent characteristic could be the defect-free assumption of the proposed structures. The presence of defects makes a tunneling barrier and by affecting the potential drop profile causes a non-linear current-voltage curve. In the present study, due to the limitations of the employed TB model all the geometries are supposed to be defect-free.

5.3.3. Conductance oscillation

As discussed in the previous section, height of the transmission peaks around the E_F for the shortest and the longest wires (i.e., lengths of 4 and $12a/2$, respectively) keeps the same range. Surprisingly, the height of transmission peaks close to the Fermi level decreases for the lengths of 5, 7, 9, and $11a/2$. This behavior is displayed in Fig. 5.15 by plotting the total transmission spectra of copper and gold for the $5a/2$ length at $V_b = 0$ V in order to compare with Figs. 5.10a and 5.11a, respectively.
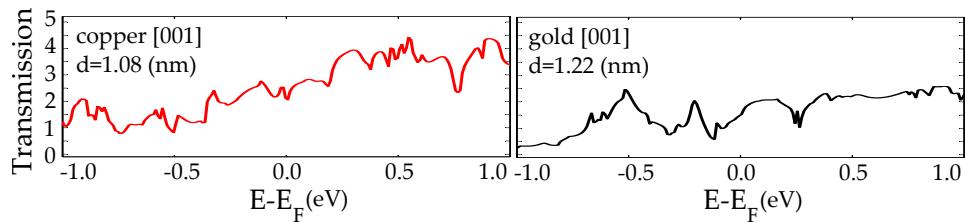
Figure 5.15.: Transmission spectrum for length of $d = 5a/2$ along the [001] for copper (Left) and gold (Right) at the limit of zero bias voltage.

It can be easily recognized how the height of peaks reduces at the Fermi energy by changing the length from $4a/2$ into the $5a/2$, leading to a lowering in respective equilibrium conductance. The difference in conductance values is related to the odd or even number of atomic layers in formation of the wires. The wire with $4a/2$ length consists of three (001) planes within the 5–4–5 atomic arrangement. Regularly, the $5a/2$ is built of four (001) planes within the 5–4–5–4 atomic configuration. The generation of further lengths follows this simple formation manner. Therefore, the conductance is expected to oscillate as a function of the number of atomic layers (wire length), which is known as the *even-odd effect*. To clarify this effect, the equilibrium conductance versus the wire length is plotted in Fig. 5.16 for copper and gold.

CZERNER et al. [101] have studied the parity oscillation of the conductance for relaxed monatomic copper wires with (001) leads in framework of the density functional approach within the KKR Green's function method, where the higher values of conductance are associated to the odd number of atoms in copper chain. An anomalous oscillation of equilibrium conductance has been found for atomic chains composed of
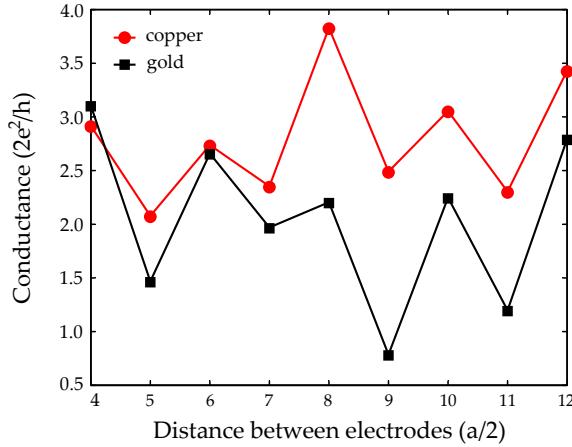
Figure 5.16.: Conductance as a function of atomic wire length calculated for copper (circles) and gold (squares) at $V_b = 0.0$ V.

alkali-metal atoms and aluminum [102–105]. On the experimental side, the conductance oscillation has been observed for atomic wires formed by gold, platinum, and iridium atoms [54]. The origin of this behavior is related to the quantum interference of electron waves, which propagate through the atomic construction and reflect at the interfaces between the wire and the electrodes.

SMIT et al. [54] have given a simple explanation of the even-odd effect reason in frame of the one-dimensional free-electron model. It is assumed that the atomic chain of length $L = na$ is bridged to one-dimensional reservoirs, where n is the number of atoms, and a denotes the interatomic distance. Electron transmission at the Fermi level adapting wave functions passing from left to right and vice versa is obtained as:

$$T = \frac{16\gamma^2}{(1+\gamma)^4 + (1-\gamma)^4 - 2(1+\gamma)^2(1-\gamma)^2 \cos(2k_2 L)}, \tag{5.2}$$

where $\gamma = k_2/k_1$, k_1 and k_2 stand for the Fermi wave vectors of the reservoirs and the atomic chain, respectively. k_2 is supposed to be fixed inside the chain due to the charge neutrality assumption. The coupling of wire and reservoirs appears as a mismatch in the Fermi wave vector, and the interference of waves scattered from the two junctions causes an oscillatory term in the output. The number of available states in the finite chain is limited to:

$$k_2 = \frac{\pi}{a}\frac{i}{n} \qquad i = 1, \dots, n. \tag{5.3}$$

In monovalent metal chain $k_2 = \frac{\pi}{2a}(n+1)/n$, leading to the electron transmission $T = 1$ for an odd number of atoms and $T = 4\gamma^4/(1+\gamma^2)^2$ for an even number of atoms. Thus, an oscillatory behavior of conductance is obtained based on the transmission

probability, in which the odd number chain shows greater value of conduction than the even number chain.

The even-odd effect is not just a peculiarity of the equilibrium condition, it is still conserved in the presence of a bias voltage. This fact is illustrated in Fig. 5.17 at bias voltage of 0.4 V. Meanwhile, the conductance oscillation under an external voltage has not been reported in previous works yet.
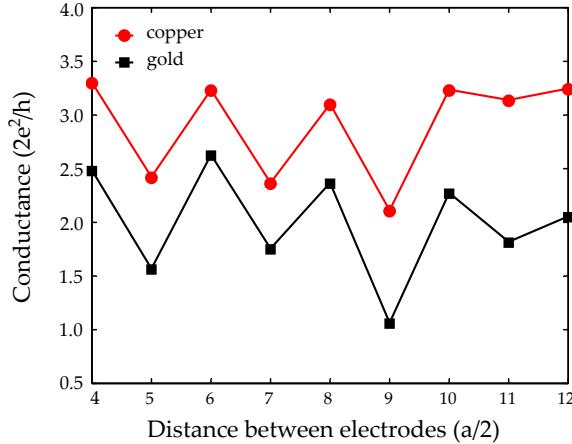
Figure 5.17.: Oscillation of conductance with respect to the atomic wire length calculated for copper (circles) and gold (squares) at $V_b = 0.4$ V.

The origin of the non-perfect oscillation may relate to the interference of coupling atomic layers, because the structure is not an ideal monovalent atomic chain. In addition, comparing the conductance of copper and gold confirms again the higher conduction of copper.

5.3.4. Width effect

In order to examine the influence of wire width, the electron transport of copper and gold atomic wires along [110] direction with $2/2$, $4/3$, and $8/6$ rod-like cross-sections (see Fig. 5.5) are analyzed. In Table 5.2, the equilibrium conductance is presented for copper and gold [110] rods.
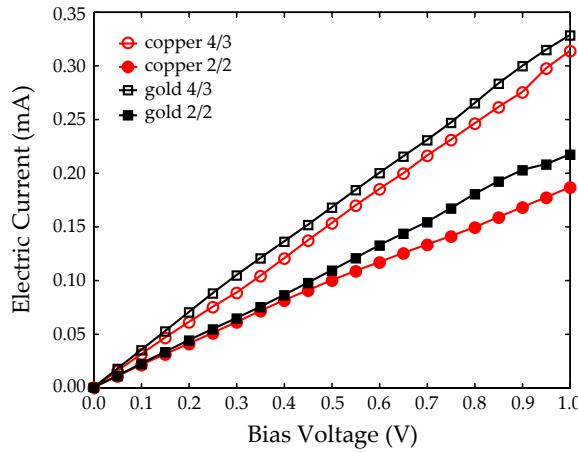
Depending on the width, the equilibrium conductance shows remarkable differences: decreasing for small cross-sections and increasing for larger ones. In case of gold, some studies have been reported recently. The present results show a good agreement with a theoretical report, which calculates the equilibrium conductance for $2/2$ and $4/3$ gold rods based on the *extended Hückel theory* [19]. The other theoretical study done for magic structures of [110] silver nanowires justifies the relation between the

Table 5.2.: Width effect on the equilibrium conductance of copper and gold [110] rods.

Atomic wire	Rod	Conductance (G_0)	
		Calculated	Literature
copper	2/2	2.71	
copper	4/3	4.06	
copper	8/6	9.07	
gold	2/2	2.81	2.8 [19]
gold	4/3	4.70	> 4.5 [19]
gold	8/6	7.13	

conductance and width of nanowires, in which increasing the width of from $2/2$ to $11/8$ configurations enhances the calculated conductance [106]. Their results agree well with the HRTEM and conductance measurements [107].

The current-voltage characteristics up to 1.0 V also represent the influence of wire width. As demonstrated in Fig. 5.18, the current-voltage curve of copper $4/3$ rod (blank circles) is located higher than that of $2/2$ rod (filled circles). The similar respect is obtained for the current-voltage characteristic of gold with $4/3$ (blank squares) and $2/2$ (filled squares) rods. Consequently, wider rods allow much more current to pass through.

Figure 5.18.: Current-voltage characteristic of copper and gold [110] rods. Wider rods of $4/3$ configuration imply higher values for current.

Another idea is proposed to test the width effect considering atomic wires of the same widths, but with different contacting surfaces to the electrodes. In the first case, copper and gold rods of $5/4$ [001] are attached to the contacts directly without cone layers.

In the second case, they are connected to the electrodes through the wide cones. The calculated equilibrium conductance confirms higher value for geometries with cones, as given in Table 5.3.

Table 5.3.: Influence of cone layers located at interfaces of the device region and the electrodes. The notation 6 indicates the number of atoms at cone layer.

Atomic wire	Rod	Cone layer	Conductance (G_0)	
			Calculated	Literature
copper	5/4	no cone	3.43	
copper	5/4	6	4.28	4.5 [13]
gold	5/4	no cone	2.47	
gold	5/4	6	2.60	

The results for copper $5/4$ connected through cones are in good agreement with experimental observations [13], where the formation of an unusual and highly stable pentagonal atomic-sized copper nanowire with a diameter of ~ 0.45 nm and conductance of $\sim 4.5 G_0$ is reported. Moreover, on the theoretical side, their simulations based on the tight-binding molecular dynamics using the second-moment approximation gives the same value of equilibrium conductance.

Similar results are obtained for both [110] and [001] rods by increasing the connection width, which enhances the conductance. Consequently, faces of the device region binding to the electrodes have a crucial role in the magnitude of conductance by determining the number of transmission channels: the more atoms on faces, the higher transmission peaks and higher values of conductance.

5.3.5. Effect of the non-mirrored electrodes

In order to emulate the atomic wire structure formed by STM, the electrodes are supposed to shift against each other, as illustrated in Fig. 5.19. In this regard, two copper atomic wires of the same length characteristics but with different locations of the contacts are proposed.

The energy dependent total transmission at $V_b = 0.5$ V for mirrored and non-mirrored structures is shown in Fig. 5.20. The similar transmission spectra suggest the equivalent electron transport properties in both cases. Thus, it is not necessary to present all other electronic features.

However, it is worth to compare the voltage drop profiles (i.e., the change in total potential between the cases of zero and finite bias voltages). Fig. 5.21 shows these
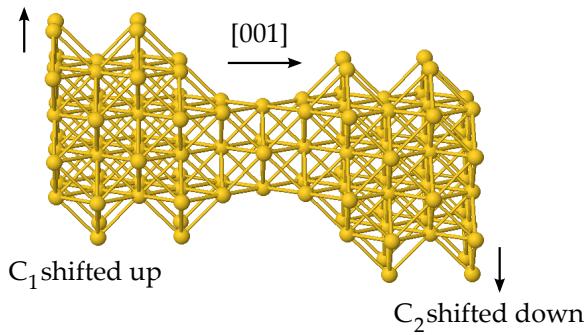
Figure 5.19.: Schematic view of the geometric modeling of an atomic wire with [001] non-mirrored electrodes; C_1 denotes the left electrode shifted up, and C_2 stands for the right electrode shifted down.
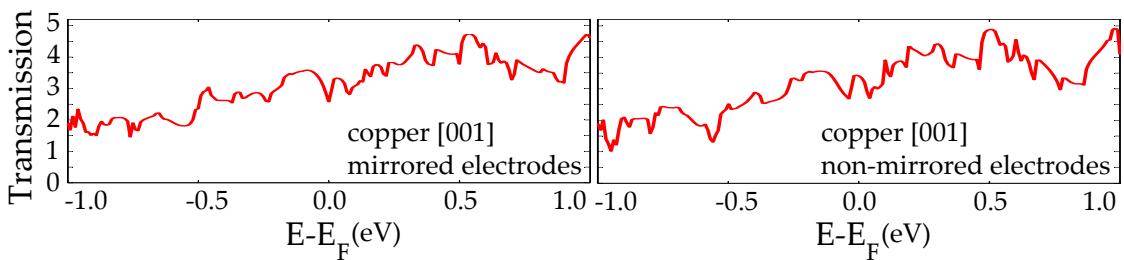
Figure 5.20.: Energy dependent total transmission of copper atomic wire with mirrored (Left) and non-mirrored electrodes (Right) calculated at $V_b = 0.5$ V.

profiles for both copper structures in the longitudinal section along the axis of the rods in the x-z plane for a potential difference of 0.5 V.
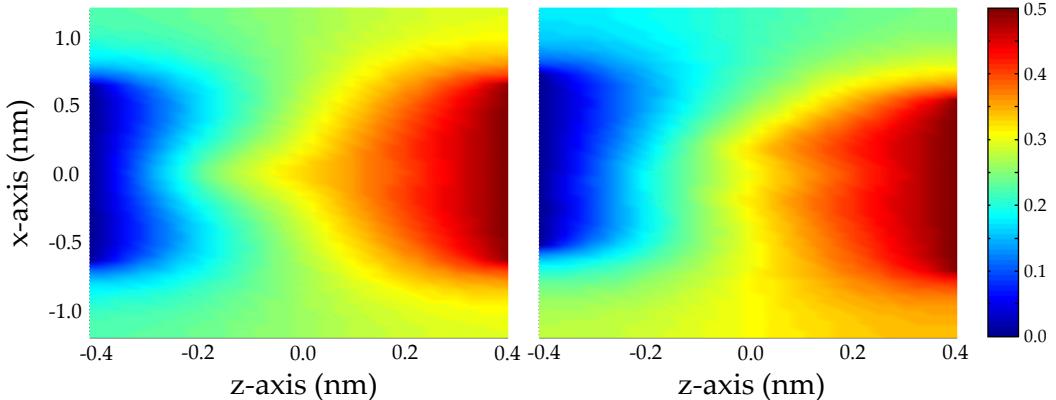
Figure 5.21.: Voltage drop in a plane along the axis of copper atomic wire sandwiched between mirrored (Left) and non-mirrored electrodes (Right) calculated at a potential difference of 0.5 V. The z-axis is the transport direction.

The main change in potential takes place at the junctions shown at the edges of the profile. It drops at the zero biased contact (left contact) and connects to the positive contact (right contact) of $\Delta V = 0.5$ V smoothly. Comparing the two diagrams in Fig. 5.21 proves that the relative position of contacts does not affect the general behavior of voltage drop profile, since their distance is too long to cause any interaction.

5.4. Non-linearity of current-voltage characteristics

A great attention has been attributed to the effect of finite bias on the transport and the non-linear current-voltage characteristic [108–111].

The different metal atomic wires considered in this work show a different magnitude of non-linearity. In the limit of small bias voltages, up to a value of about 0.3 V, all characteristics remain almost perfectly linear. Both for copper and gold, the [110] structures preserve a good linearity of the current-voltage curves in the whole investigated interval of the applied bias voltage, as illustrated in Figs. 5.7 and 5.9. Regarding the [001] structure, in case of copper the deviation from linearity is quite small, whereas in case of gold a pronounced non-linearity can be seen. The non-linearity of the current-voltage curves is given by the dependence of the transmission coefficient on the bias voltage.

The non-linear current-voltage characteristic can be associated to the charge transfer at different bias voltages, and the weak transmission functional has a secondary effect in this aspect. To shed light on, the electron charge distribution of gold $5/4$ [001] rod at 0.0 and 0.3 V is plotted in Fig. 5.22a. In fact, the charge neutrality of each atom in gold $5/4$ [001] rod may not be fulfilled at various voltages as supposed in the self-consistent calculations for the device region (see Sec. 3.7.1). Therefore, minor change of charge neutrality at 0.3 V with respect to 0.0 V modifies the linear current-voltage curve. The charge distribution is also plotted for copper $5/4$ [001] rod in Fig. 5.22b, which causes linear current-voltage curve due to the almost achieved charge neutrality condition.

The difference of charge neutrality accomplishments for copper and gold is interpreted based on the employed method in this study. As discussed in Sec. 4.3, Slater-Koster parameters used for gold in the TB model were fitted against the bulk structure calculations. Thus, it is doubtful whether these parameters are transferable to the atomic-scale structures under non-equilibrium conditions or not.

In this respect, the results do not correspond to the experimental studies, which provide non-linear current-voltage characteristics for metal atomic contacts. In earlier reports, the non-linearity has been attributed to the presence of contaminants in air [111]. To rule out the impurity effect, Costa-Krämer et al. [109] have repeated experiments in an ultrahigh vacuum using STM, where the high-stability features of formed metal nanowires make the possibility of measuring current-voltage characteristics. They have
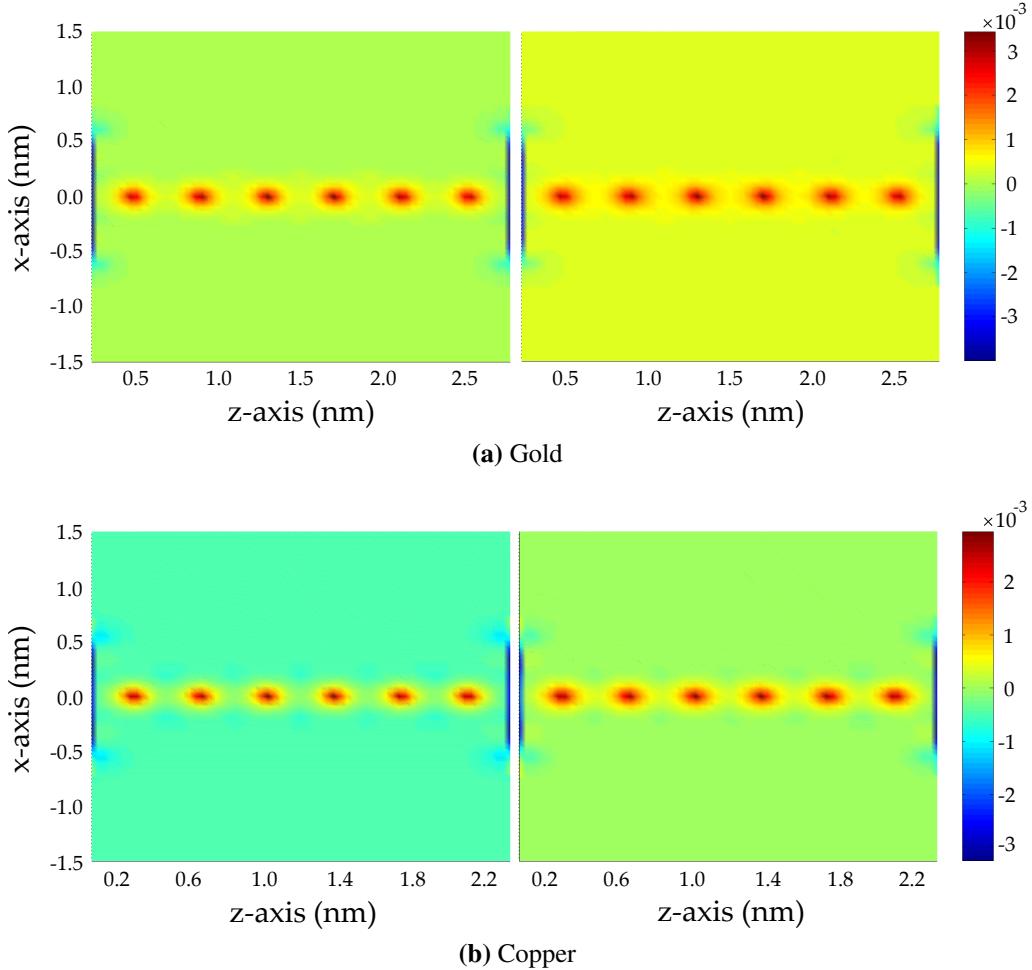
(a) Gold

(b) Copper

Figure 5.22.: Charge density distribution in a plane along the transmission of (a) gold [001] rod at equilibrium (Left), and under bias voltage of 0.3 V (Right) (b) copper [001] rod at V_b = 0.0 V (Left) and V_b = 0.3 V (Right). Dark points are the atomic layer positions. A small charge transfer between atomic faces appears in case of biased gold rod, while the charge neutrality is reserved for that of copper.

related the origin of the observed non-linearity to the strong electron-electron interaction effects. Further, YOSHIDA et al. [112] have found a non-linear current-voltage curve for a short gold nanowire, while a long nanowire produces a linear current-voltage curve under ultra high vacuum using a TEM-STM system. They have related the non-linearity to the thickening of the nanowire during increasing current. A well done study in this regard by MEHREZ et al. [113] suggestes that existence of sulfur impurities at the junction of stable gold acting as a tunneling barrier causes the non-linear current-voltage curve. A linear behavior is obtained for bias voltages of V_b < 0.5 V. The impurity effect is not considered in the present study due to the restriction from the Slater-Koster parameters. Other effects such as heating and charging can contribute to the non-linearity

either. However, to achieve a clearer picture of the origin of this property, additional theoretical and experimental investigations would be necessary.

5.5. Temperature effect

Investigating temperature dependent transport is essential for the device design in mesoscopic range in future applications. In the present study, it is expected that electron transport properties are influenced negligibly by temperature because only the coherent transport is employed, and the electron-phonon inelastic scattering is left out.

The current-voltage characteristic for copper and gold $2/2$ [110] rods is calculated for liquid helium temperature (i.e., T=4.2 K) as well as for room temperature. As plotted in Fig. 5.23, results show analogous behavior for different temperatures. The reason
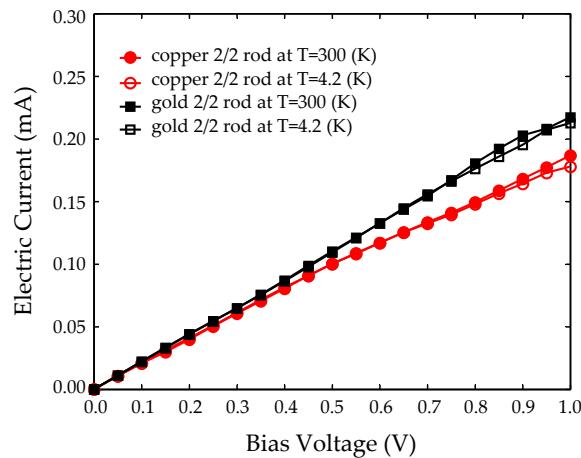
Figure 5.23.: Current-voltage characteristic of copper and gold $2/2$ [110] rods calculated at different temperatures.

justifying the assumption of ignoring the electron-phonon interaction could be attributed to the scale of modeled geometries. Since even at room temperature, the length scale characteristics of the system are still much smaller than that can be affected by inelastic mean free path, and the influence of various temperatures would appear in the Fermi distribution function. In Table 5.4, the Fermi energy and equilibrium conductance under various temperatures are given, in which the differences due to the temperature are not remarkable.

At the end of this chapter, it is necessary to mention that the theoretical results deal with some restrictions when compared to those of experiments. In all experimental techniques, individual results are not reproducible: conductance curves measured during the nanowire breaking are different due to the different dynamical evolution for

Table 5.4.: Temperature effect on the conductance of copper and gold $2/2$ [110] rods.

Atomic wire	Temperature (K)	Fermi energy (eV)	Conductance (G_0)
copper	300	-4.15	2.71
copper	4.2	-4.10	2.64
gold	300	-7.07	2.81
gold	4.2	-7.05	2.80

every process. Therefore, a usual method to overcome these constrictions is to perform a statistical analysis involving many individual measurements. However, due to the limited control on the formation of the contacts, the information is obtained mostly by a statistical analysis of the conductance data (e.g., building a histogram of conductance curves).

Chapter 6.

Electron Transport in Single Point Contacts

6.1. Introduction

The second part of the present study belongs to single point contacts. Several theoretical and experimental works have actually been carried out to study the electron transport properties of atomic-scale contacts, but this study allocates the calculations to the smallest possible contact: single atom contact, in which their formation and manipulation have been reported widely [8, 16, 17]. A similar attempt as in the previous chapter is done to analyze the electron transport in copper and gold point contacts, based upon the observation of bipyramidal shapes during elongation of nanocontacts.

The further motivation of studying metallic single point contacts is to get deep insight into the transmission channel concept, which gives a more detailed description of the conductance and is useful for the interpretation of the results, in which decomposition of transmission channels is not feasible in case of the atomic wires. The results of transmission channels decomposition, conductance value, and linear current-voltage curve agree well with those of theoretical and experimental reports.

The outline of this chapter is as follows: a short explanation of point contacts formation is represented in Sec. 6.2, as well as proposed geometric models. Then, the transmission eigenchannels and the contribution of each orbital are analyzed for copper and gold single atom contacts with electrodes along [001] and [111] directions. The conductance is evaluated as a function of the bias voltage, in addition to the equilibrium conductance in Sec. 6.3.2. In Sec. 6.3.3, the current-voltage characteristic is interpreted based on the conduction channels and the charge neutrality circumstance.

6.2. Concept of the single point contact

According to the previous discussion, the HRTEM images predict three possible contacts, in which the [001] and [111] show bipyramidal shapes, forming either atomic suspended chains or single atom contact [11, 13]. In the following, the single atom contact of both elongation, the measuring setup, and modeled geometries are introduced.

6.2.1. Realization of one atom contacts

The contacts produced by the STM technique have been explained in Sec. 5.2.1. It is worth introducing the related MCBJ method, originally introduced by MORELAND [114]. Within the MCBJ technique, it is possible to generate electric contacts of the width of only one atom via pulling free-standing metallic bridges and breaking the junctions. The mechanism of MCBJ technique is illustrated schematically in Fig. 6.1. The bending of the substrate due to the movement or expansion of the piezo over a distance Δ, causes the epoxy droplets to move apart by δ, leading to breaking the junctions.
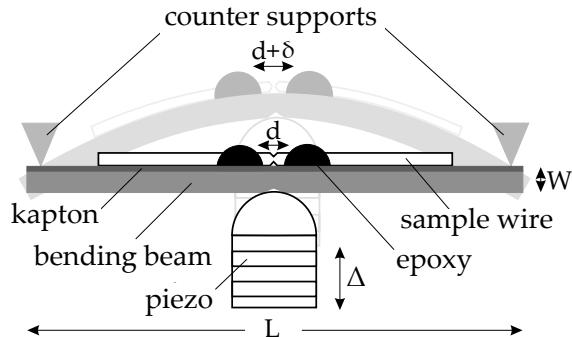
Figure 6.1: Setup of MCBJ technique monitoring a substrate with a sample mounted in a three-point-bending configuration. The amount of bending is exaggerated [15].

The conventional MCBJ method takes advantage of the fact that most metals (i.e., solid at room temperature) are available in the form of a thin polycrystalline wire. The process starts with mounting a macroscopic notched wire or nanofabricated bridge of such metal on a flexible substrate, cooled down to the liquid helium temperatures in vacuum, and then broken in order to expose clean fracture surfaces. These clean surfaces can be brought in and out of the contact, using a piezoelectric element for fine positioning control. By pulling out a contact into a thin bridge, or a nanowire, and simultaneously measuring the conductance, it is feasible to monitor the evolution all the way down to the point when it consists of just a few atoms, and finally breaks completely. By pressing the electrodes back together, a new contact can be made, and the whole process can be repeated over and over again [15].

6.2.2. Modeling of single point contacts

The modeling of single point contacts is based on the predicted forms by HRTEM images. The modeling procedure follows the same rule as in the atomic wires. In this regard, it starts from a central single atom, and then enough cone layers must be considered around to avoid the interaction between electrodes. The growth orientation of copper and gold single point contacts is proposed to adopt [001] and [111] directions. No relaxation is done, and the atomic distances lie on the experimental reports.
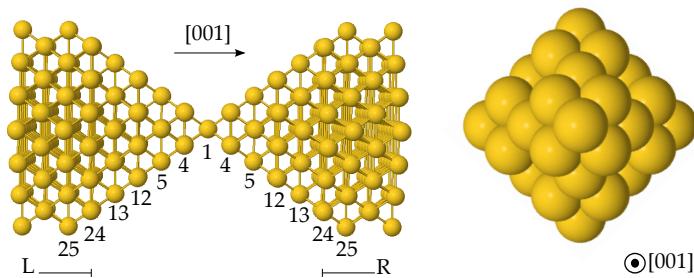
Figure 6.2.: Schematic view of the modeled [001] single point contact. In the side view (Left), labels cite the number of atoms on each layer. In the top view (Right), the tip consists of the central atom in addition to the cone layers as pyramidal construction.

The scheme of the modeled point contacts in [001] direction is predicted in Fig. 6.2 in detail. The atomic configuration on cone planes obeys the 4–5–12–13 arrangement connecting to the wide electrode layers of 24–25 arrangement, so that a bipyramidal shape is designed. The number of atoms at the device region is 69 and at the mirrored contacts is 196.
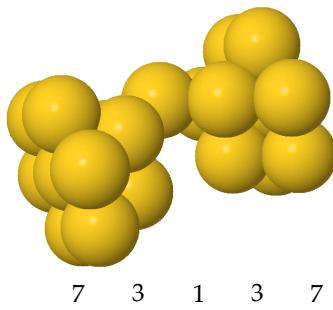
Figure 6.3: Atomic arrangement of [111] single point contact. Only the central part of the device region is shown.

Fig. 6.3 shows the modeled single point contact in [111] orientation with cone layers consisting of 3–7–16–25 atomic configuration. To consider the ABC ABC $\cdots$ symmetry of [111] hexagonal planes, three layers made of 25–25–25 arrangement are modeled by the separation distance of $a\sqrt{3}/3$.

6.3. Copper and gold single atom contacts

In this section, the electron transport characteristics of copper and gold single point contacts, such as total and partial transmission spectra, conductance, current-voltage curves, density of states, and charge density distribution profile are presented.

6.3.1. Transmission eigenchannels

The concept of eigenchannels addressing the Landauer-Büttiker formalism for conduction has been described in Sec. 2.4.2. The dimension of transmission matrix in $G = G_0 \sum T_i$ can be arbitrary large depending on the size of the central region, but the actual number of conducting channels (i.e., channel with a non-vanishing transmission eigenvalue) is limited by the number of orbitals in the narrowest section of the neck. In fact, each conducting channel can be classified according to the angular momentum contribution, when the channel wave function is projected on the contact atom of the construction. Thus, the transmission channel is related to states of the contact atom [115]. In order to calculate the number of transmission eigenchannels, considering a neck with one-atom-thick instead of an atomic wire with a rod-like neck is required.

For the first time, the transmission coefficients along each conducting channel have been obtained in experiments by determining the eigenchannels of aluminum quantum point contacts up to six conduction channels reported by SCHEER et al. [17], confirming that eigenchannels concept could not be a theoretical abstract. In addition, further analyses via MCBJ experiments and the TB model prove the relation between the number of conducting channels and the number of valence orbitals of a contact atom [16, 115].

For copper with electron configuration of [Ar] $3d^{10}4s^1$ in [001] elongation direction, the transmission probability at liquid helium temperature for each conduction channel is depicted in Fig. 6.4 as a function of electron energy.

The transmission decomposition up to four eigenchannels is calculated. According to the report from AGRAÏT et al. [116], a single atom can carry many channels up to five or six for *sd* metals, which may only be partially open.

The channel decomposition in Fig. 6.4a shows that the transmission at zero bias voltage is mainly made from three considerable conducting channels. The first channel has the main portion in conduction. In contrast, the forth channel contribution is negligible. The interesting aspect is appearing the twofold degenerate channels composed of the second and the third channels. The degeneracy has been reported also by BAGRETS et al. [117] for copper single point contact with [001] character using the ab-initio KKR Green's function formalism.
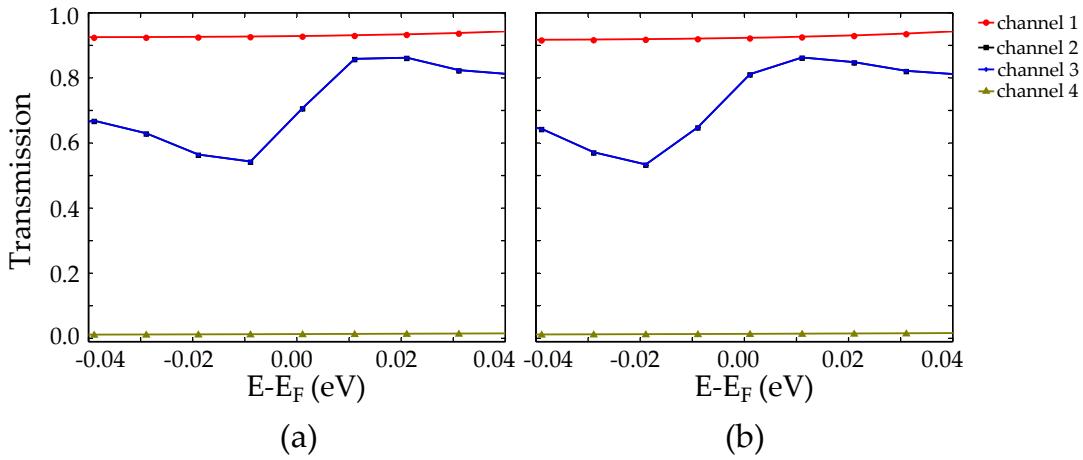
Figure 6.4.: Transmission probability of each conduction channel of copper single point contact calculated at liquid helium temperature under (a) the limit of zero bias voltage and (b) an external bias voltage of $V_b = 10$ mV. The Fermi level is set to zero.

The same effort is done to obtain the channel decomposition at $V_b = 10$ mV plotted in Fig. 6.4b. Comparing two panels shows that the portion of channels is not affected significantly by the applied bias voltage, and the transmission decomposition is reserved as previous.
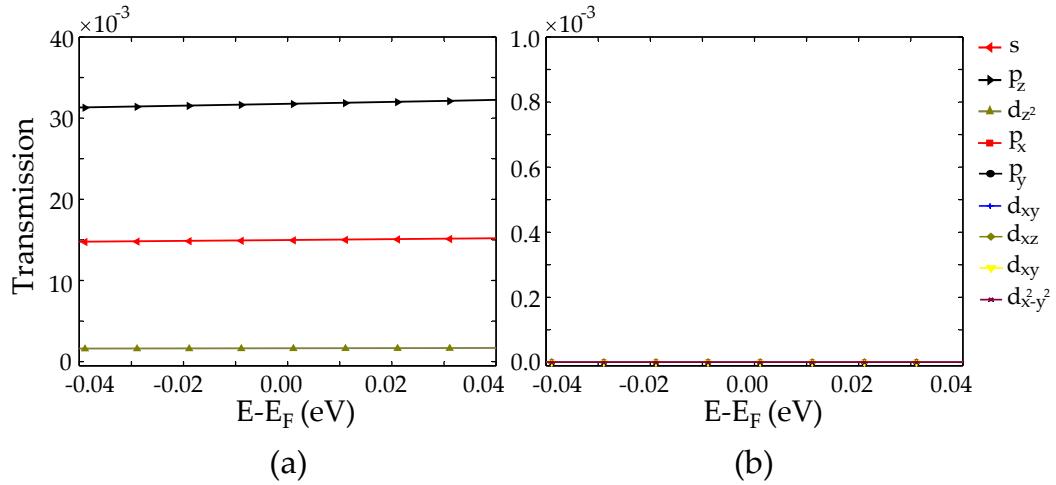
Figure 6.5.: Contribution of atomic orbitals in the first conduction channel consists of (a) the s, p_z, and d_{z^2} orbitals having the main portion in conductance and (b) the p_x, p_y, d_{xz}, d_{yz}, d_{xy}, and $d_{x^2-y^2}$ states.

In the next step, the contribution of each angular momentum in the conducting channels at equilibrium condition is calculated. Fig. 6.5 shows the contribution of $s, p_z, d_{z^2}, p_x, p_y, d_{xz}, d_{yz}, d_{xy}$, and $d_{x^2-y^2}$ states in the first conduction channel. It can be seen easily, s, p_z, and d_{z^2} orbitals attribute the main portion of the first channel, espe-

cially s and p_z states are combined to form the propagating conductance channel (σ character channel). Note that, the z-axis as the transport direction passes through the central atom. Meanwhile, the contribution of other orbitals in the first channel around the Fermi energy is zero. As shown in Fig. 6.5, $p_x, p_y, d_{xz}, d_{yz}, d_{xy}$, and $d_{x^2-y^2}$ states are completely reflected close to the Fermi energy.

Decomposition of the twofold degenerate channels illustrated in Fig. 6.6 shows that, in contrast to the first conduction channel, the minor contribution belongs to the s, p_z, and d_{z^2} states. Further, copper single point contact of [111] character with atomic con-
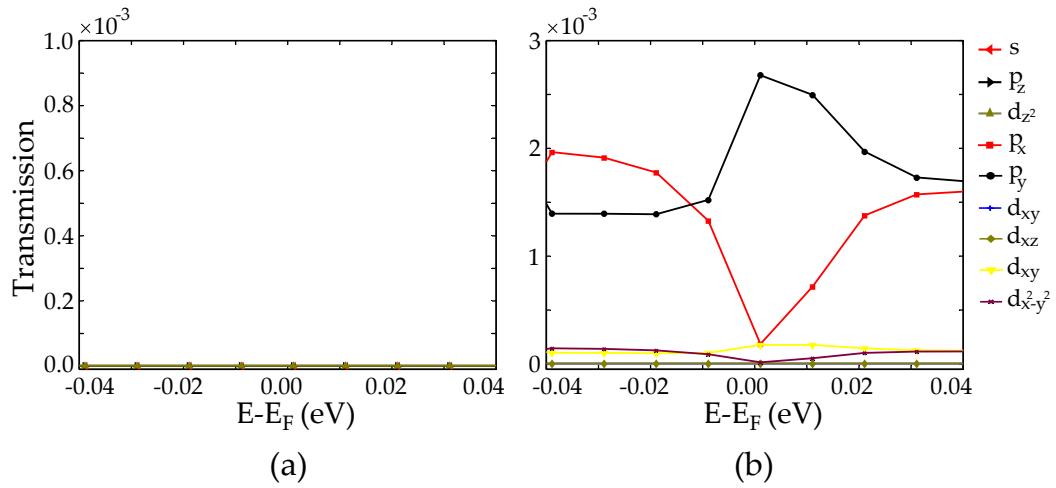
Figure 6.6.: Decomposition of the twofold degenerate channels to (a) the s, p_z, and d_{z^2} orbitals and (b) the $p_x, p_y, d_{xz}, d_{yz}, d_{xy}$, and $d_{x^2-y^2}$ states.
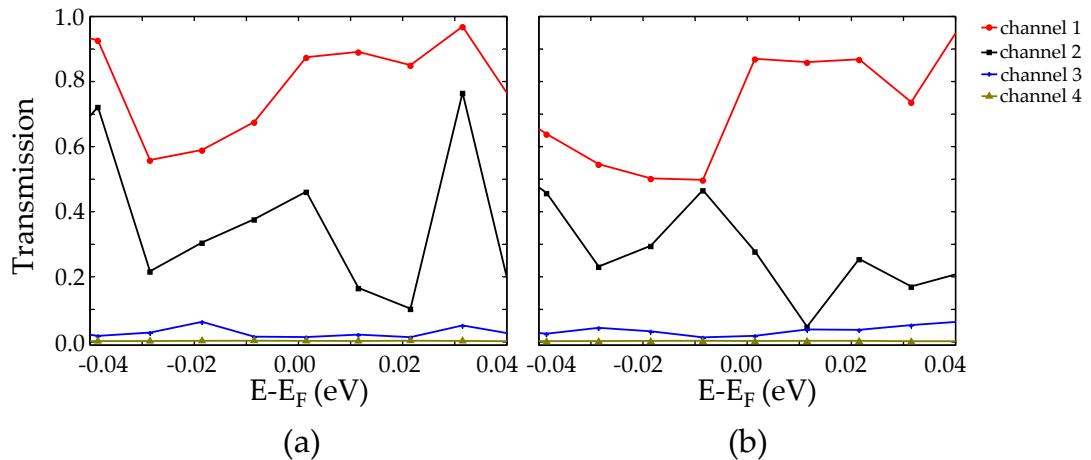
Figure 6.7.: Energy-dependent transmission and its decomposition to the conduction eigenchannels of copper single atom contact with [111] electrodes at (a) zero bias voltage and (b) $V_b = 10$ mV.

figuration demonstrated in Fig. 6.3 is proposed. The transmission considered for four channels is plotted in Fig. 6.7 at the limit of zero bias voltage. Only three channels are transmitted, and the forth channel does not take part in the conductance. In comparison to Fig. 6.5a, the transmission eigenchannels spectra show more fluctuations, and the degeneracy of the second and the third channels is destroyed by gliding down the third channel. Moreover, a reduction in spectrum appears.

Decomposition of the first conduction channel is plotted in Fig. 6.8. The combination of s, p_z, and less portion of d_{z^2} states forms the first channel. Although the contribution of p_x, p_y, d_{xz}, d_{yz}, d_{xy}, and $d_{x^2-y^2}$ states is rather small, it is not zero in contrary with [001] case due to the remarkable role of p_x and p_y orbitals (π character channel) around the Fermi level.
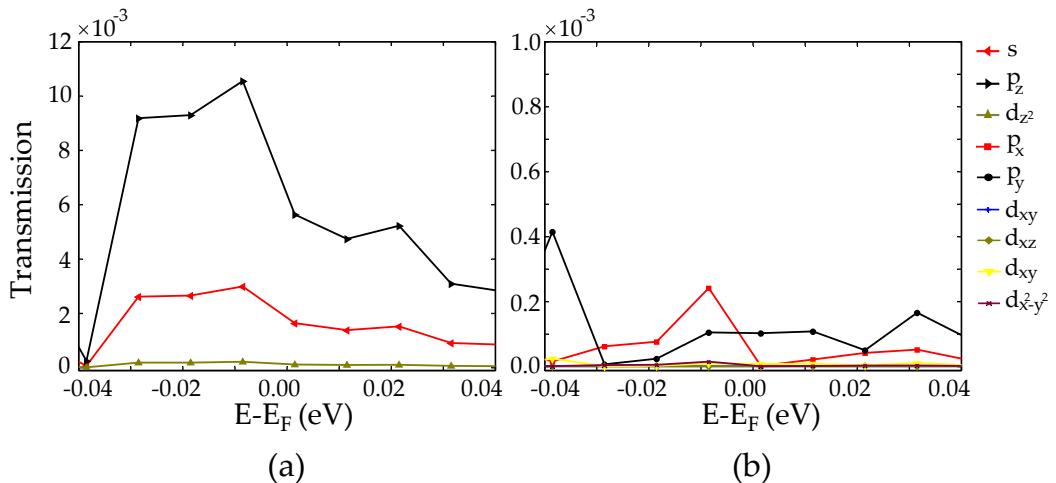
Figure 6.8.: The first conduction channel decomposition of copper single point contact with [111] character to (a) the s, p_z, and d_{z^2} states and (b) the p_x, p_y, d_{xz}, d_{yz}, d_{xy}, and $d_{x^2-y^2}$ orbitals.

The second conduction channel analyzed at the equilibrium is shown in Fig. 6.9. The contribution of s, p_z, and d_{z^2} states is greater than the portion of other orbitals in the same channel.

Decomposition of the third conduction channel is not shown because of its negligible role in the transmission. The splitting of twofold degenerate channels in [111] point contact can be related to the difference of geometric symmetry. As depicted in Figs. 6.2 and 6.3, the single atom at the center is located quite symmetrically on the z-axis in case of [001] direction, but it makes an angle in the x-y plane in [111] direction, which leads to the contribution of p_x and p_y orbitals in the first channel.

Furthermore, the geometric symmetry affects the available density of states in the structure. In the used method, considering the segment of a single atom from the total density of states is not feasible, and it is required to propose some atomic faces around
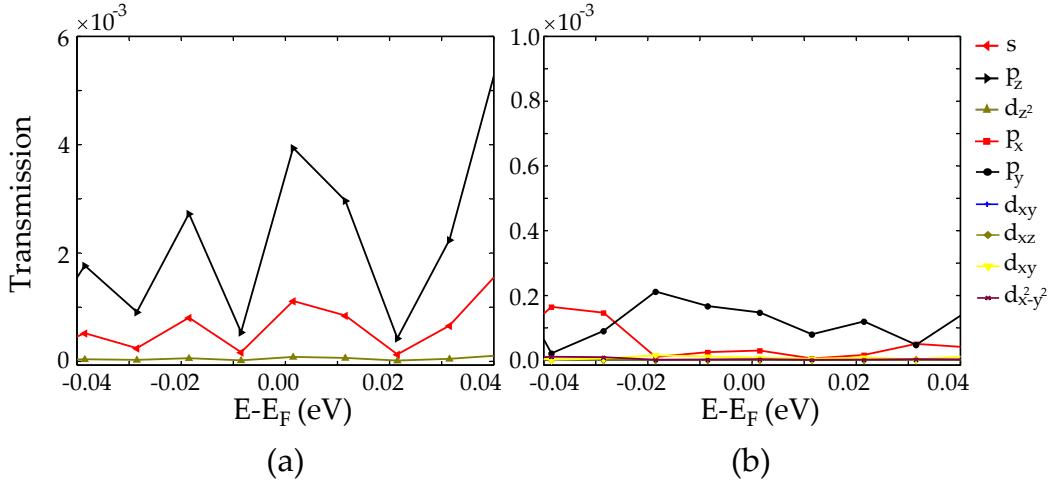
Figure 6.9.: Analyzing the second conduction channel of copper [111] point contact, (a) the contribution of s, p_z and d_{z^2} orbitals and (b) the portion of p_x, p_y, d_{xz}, d_{yz}, d_{xy}, and $d_{x^2-y^2}$ states.
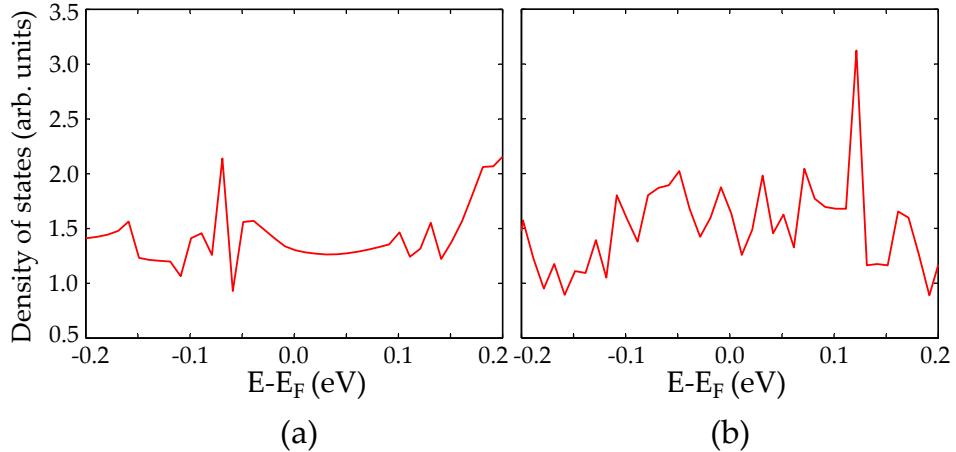

Figure 6.10.: The density of states with respect to the electron energy for copper single point contact for (a) the [001] symmetry and (b) the [111] symmetry.

(i.e., in order to avoid the interaction between electrodes). In case of [001] contact, the density of states is calculated for the central atom and two neighbor planes with (4×4) atomic configuration, where the distance between planes is set to $a/2$. In [111] direction, the single atom together with neighbor faces with (3×3) atomic arrangement and separation distance of $a\sqrt{3}/3$ are considered in density of states calculations. Fig. 6.10 displays the density of states at zero bias voltage under mentioned conditions. The density of states forms very sharp resonances close to the Fermi energy as localized states in [111] character due to the weak coupling with the orbitals of the neighboring sites. The plot shows a slow variation in visinity of the E_F in [001] direction as a result of a strong interaction.

The same calculations for the gold with electronic configuration of [Xe] $4f^{14}5d^{10}6s^1$ are presented. The transmission eigenchannels of [001] direction at liquid helium temperature and for zero bias voltage are shown in Fig. 6.11. The transmission decomposition indicates existence of three channels, where a twofold degeneracy of the second and the third channels is observed. The presence of degenerate channels for single gold atom contact sandwiched by [001] electrodes has been reported by several authors [20, 118, 119]. The effect of the applied bias voltage is negligible in the transmission spectrum as seen in Fig. 6.11.
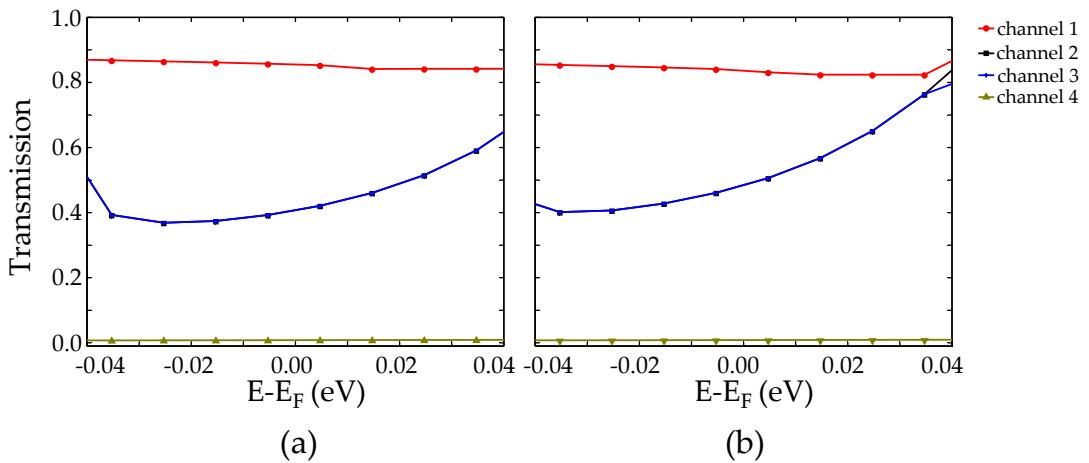
Figure 6.11.: Transmission decomposition to the conduction channels in gold with [001] electrodes at (a) zero bias voltage and (b) $V_b = 10$ mV.

The contribution of states in the first channel at the limit of zero bias voltage is illustrated in Fig. 6.12. The first channel is dominated by states of s, p_z, and d_{z^2}, where the portion of other orbitals is negligible.

As demonstrated in Fig. 6.13, the double degenerate channel is build up by main combination of the degenerated p_x and p_y states and minor participation of degenerated d_{yz} and $d_{x^2-y^2}$ orbitals. The twofold degenerate d_{xy} and d_{yz} do not play any role in transmission.

Similar effort is done to analyze the conduction channels of single gold atom bridged to the [111] electrodes. As depicted in Fig. 6.14, turning from [001] into [111] destroys the degeneracy. The third channel contribution is quite negligible as the forth channel. In addition, the eigenchannels are not that robust to the external bias voltage of 10 mV. Due to the main role of the first channel in transmission, only the first eigenchannel is decomposed into its components as illustrated in Fig. 6.15. According to the channel decomposition, the combination of s, p_z, and d_{z^2}, with more pronounced portion of p_z, forms the first conduction channel, and the portion of other states is in secondary.
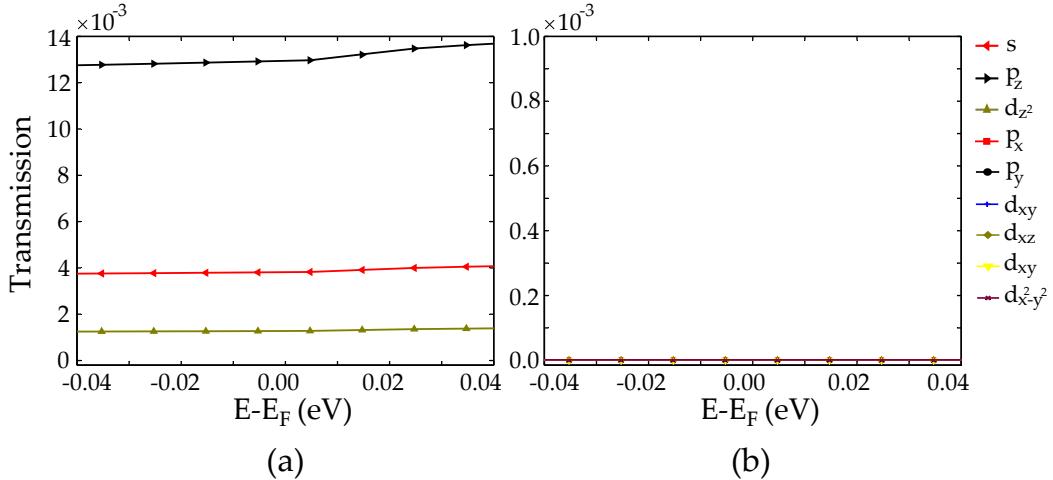
Figure 6.12.: Decomposition of the first conduction channel at equilibrium for gold single point contact with [001] character to (a) the s, p_z, and d_{z^2} orbitals and (b) the p_x, p_y, d_{xz}, d_{yz}, d_{xy}, and $d_{x^2-y^2}$ states.
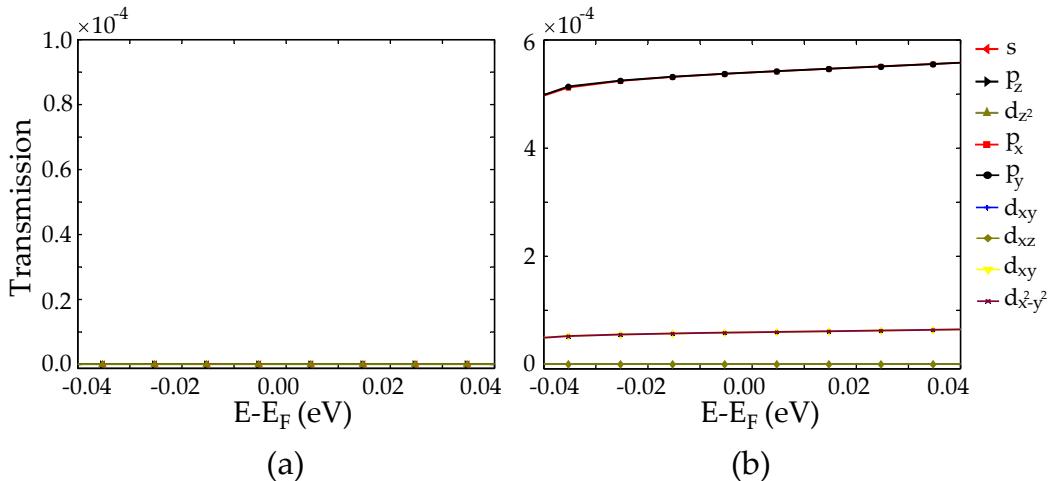

Figure 6.13.: The double degenerate channel decomposition to the atomic orbitals, (a) s, p_z, and d_{z^2} states having negligible role and (b) the main contribution of degenerate conduction channel made by p_x and p_y orbitals.

The identical reasoning used in the case of copper is applicable to gold in order to explain transmission eigenchannels differences of the [001] and [111] structures. However, it is worth considering the role of [001] and [111] symmetries in the density of states. As illustrated in Fig. 6.16, the density of states of [001] geometry changes slowly in vicinity of the Fermi energy, in contrast with [111] case displaying more localized states raised from the weak interactions.
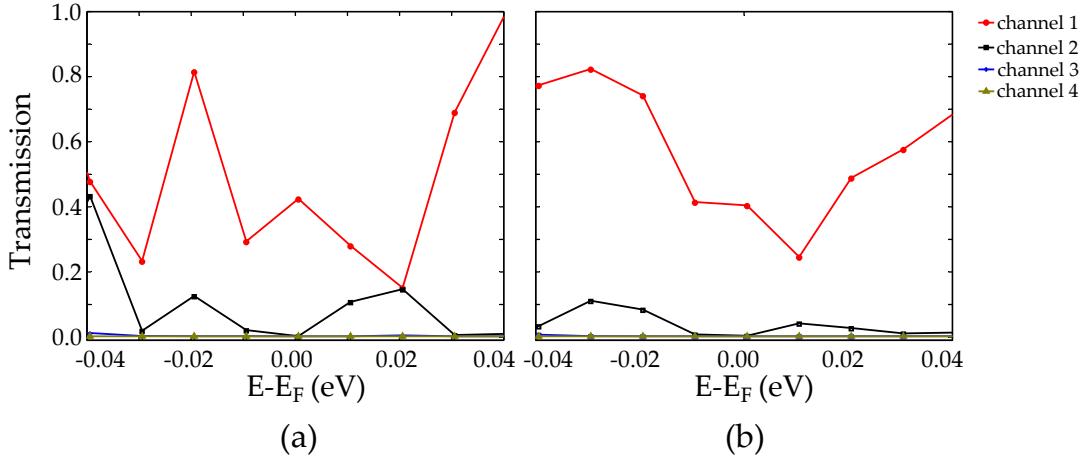
Figure 6.14.: Transmission eigenchannels of gold single point contact with [111] character at (a) the limit of zero bias voltage and (b) $V_b = 10$ mV.
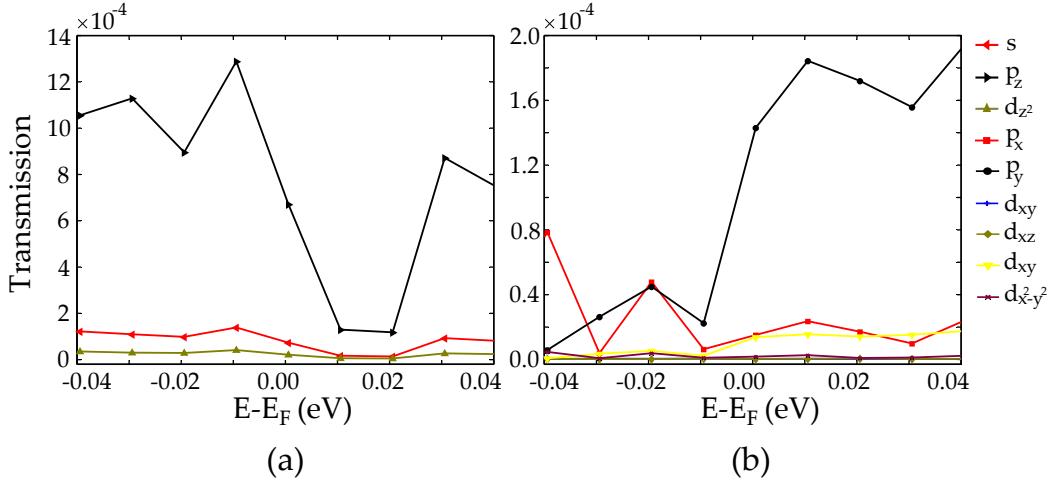
Figure 6.15.: Decomposition of the first conduction channel of gold [111] at equilibrium, contribution of (a) the s, p_z, and d_{z^2} orbitals and (b) the p_x, p_y, d_{xz}, d_{yz}, d_{xy}, and $d_{x^2-y^2}$ orbitals.

The transmission eigenchannels, their components, and the density of states in gold single atom contact with [001] and [111] symmetries compared to the respective copper point contacts participate identically in the electron transmission.

6.3.2. Conductance

Transmission coefficients in Figs. 6.4 and 6.7 show a broad channel mainly *sp*-like below one, meaning that no conductance quantization is found. In other words, conduction channels are only partially open in contrary to the case of quantum point contacts
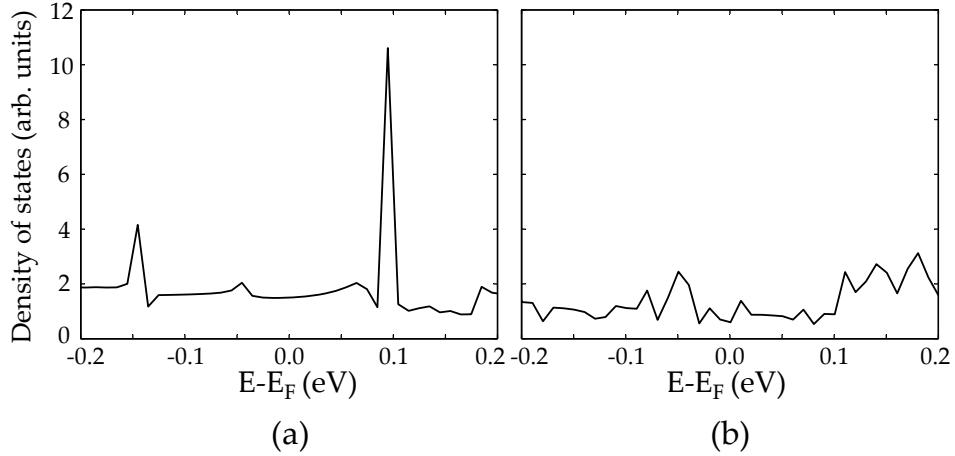
Figure 6.16.: Calculated density of states for gold point contact at equilibrium for (a) the [001] symmetry and (b) the [111] symmetry.

realized in the two-dimensional electron gas, where a clear conductance quantization has been observed [120].

The equilibrium conductance is calculated as a sum over all contributed transmission eigenchannels close to the Fermi energy as expressed in Table. 6.1.

Table 6.1.: The equilibrium conductance of copper and gold single point contacts with respect to the electrodes orientation calculated at liquid helium temperature.

Element	Orientation	Conductance (G_0)	
		Calculated	Literature
copper	[001]	0.93	0.96 [18]
copper	[111]	0.84	
gold	[001]	0.85	~ 1 [19]
gold	[111]	0.42	< 1 [19]

The result for copper is in good agreement with experiments in addition to the theoretical reports presented in the Table. 6.1. YANSON [15] has reported the value of conductance as $\sim 1G_0$, and the measurements of BAKKER et al. [121] have obtained the conductance of $\sim 1G_0$ for pure copper.

In case of gold, the results generally agree well with many experiments, which measure the conductance value below $1G_0$ [15, 115]. In other experiments by SCHEER et al. [16], the conductance value at the last stage of fabrication via the MCBJ technique has been measured between $0.3G_0$ and $0.8G_0$, which is generally in agreement with the considered orientations.
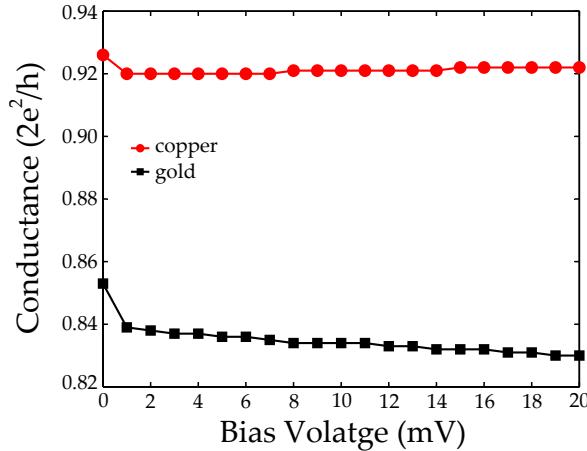
Figure 6.17.: Conductance as a function of bias voltage in copper (circles) and gold (squares) single point contacts with [001] characters.

Further, the conductance as a function of bias voltage up to 20 mV is calculated for copper and gold with [001] characters shown in Fig. 6.17. As the transmission spectra are rather robust to the applied bias voltage, no significant change of conductance with bias voltage is expected. In the considered bias voltage interval, copper single point contact shows higher value of conductance than gold.

6.3.3. Current-voltage characteristics

The voltage range applied in experiments is typically of the order of a few tenth of mV. For this bias range, the ohmic behavior is supposed in the normal metal system.
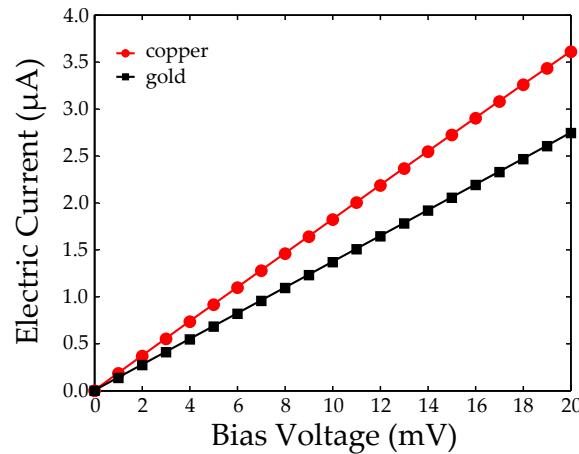
Figure 6.18.: Linear current-voltage characteristics of copper (circles) and gold (squares).
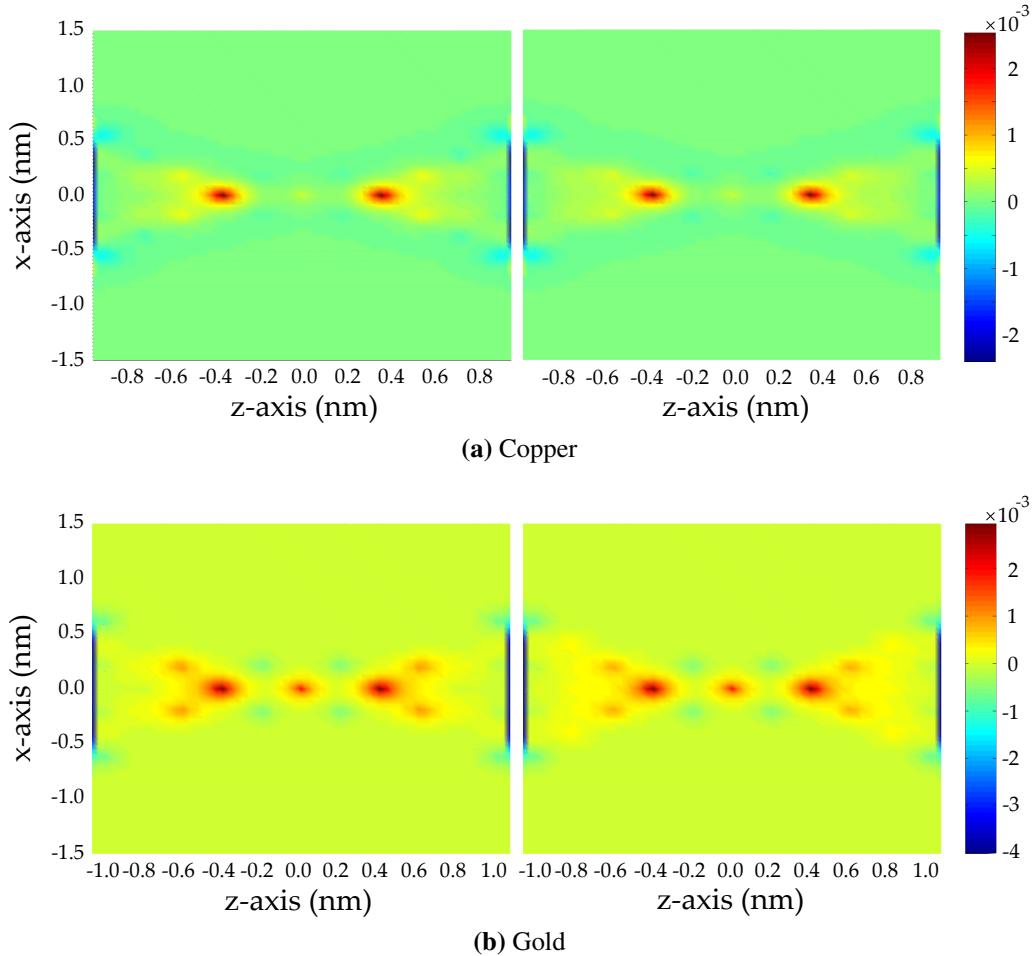
**(a)** Copper

(b) Gold

Figure 6.19.: Charge density distribution in a plane along the single point contact with [001] character at the limit of zero bias voltage (Left) and an external bias voltage of $V_b = 10$ mV (Right) for (a) copper and (b) gold. Atoms positions appear as dark points.

In case of the [001] orientation for both elements, the d_{xy} and $d_{x^2-y^2}$ orbitals do not support current, since they are oriented perpendicular to the current direction. In addition, the slow variation of the channel transmissions with energy at both zero and finite bias voltages depicted in Fig. 6.4 results in a very linear current-voltage curves. The same conclusion could be obtained for gold [001] contact from Fig. 6.11.

The calculated current-voltage characteristic for copper and gold with [001] orientations at liquid helium temperature and up to 20 mV is shown in Fig. 6.18. The biased copper represents 3.6 μA at 20 mV, whereas the respective value for gold is assessed to be 2.7 μA. The linear behavior of current-voltage characteristic is in agreement with an investigation included both theory and experiment, where linear current-voltage curves at small bias voltages are obtained for gold contacts [20].

According to the discussion in Sec. 5.4, the supplementary condition leading to the linearity is the charge neutrality at finite bias voltage. To ensure, the charge density distribution is plotted in terms of the atomic position in Fig. 6.19 at zero bias limitation and at a finit bias voltage of $V_b = 10$ mV. The right panels corresponding to the biased copper and gold structures confirm that even at a finite bias voltage the charge transfer is more negligible than tends to influence on current, and the charge neutrality condition is reserved for both equilibrium and biased conditions.

Chapter 7.

Conclusions and Perspectives

7.1. Conclusions

According to the discussion in Chap. 2, the electron transport at atomic scale was attributed to the ballistic transport regime, requiring new simulation tools to treat appropriately the quantum mechanical aspects. Among several techniques, the *non-equilibrium Green's function density functional tight-binding model* via the gDFTB code has been preferred to implement the transport computations in *copper and gold atomic contacts*. The formalism has bridged the gap between empirical tight-binding and ab-initio methods. Moreover, exploiting the non-equilibrium Green's function has ensured the *electron transport in biased devices*, which has been often ignored in previous simple formalisms. The theoretical method has described in detail, in which the electron transport characteristics have been deduced through the Landauer theory.

The geometry structure modeling has been based on the recent experimental observations, capturing the fact that during fabrication, atomic wires were crystalline and defect-free, and adopted three orientations, in which the smallest contacts of one-atom-thick could be formed within [100] or [111] elongation direction. The two-terminal conductor has been modeled considering semi-infinite crystalline leads and the atomic wire or single point contact as device region sandwiched in between. Furthermore, assuming an equilibrium thermodynamic potential for semi-infinite electrodes, keeping them far away to avoid any interaction, and placing some atomic layers of cone-shape at interfaces of construction has made it possible to simulate structures close to the reality.

Special attention has been given to clear the **relation between the geometry of atomic-scale structures and their electronic transport properties**. In Chap. 5, the role of geometric characteristics of copper and gold atomic wires of [001] and [110] orientations has been analyzed.

According to the presented results, *electron transport properties* including total transmission, current-voltage curves, and conductance of *atomic wires have been affected*

weakly by the crystalline orientation, especially in vicinity of small bias voltages (i.e, $V_b < 0.2$ V), current-voltage curves of two elongation directions have been coincident.

The effect of wire length has modified the transport by producing the conductance oscillation within the *even-odd effect*, originated from the quantum interference phenomenon. It has been shown that the *conductance oscillation could appear in biased systems* as well as under equilibrium conditions. Nevertheless, the mean value of conductance has been preserved with respect to the various lengths in ballistic transport regime.

The *faint role of crystalline orientation and length* have been related to the respective electron transport class: until ballistic transport regime has been conserved, the insignificant relation would be established between geometry structure and electron transport properties.

The *width of the structure has had remarkable influence on conductance*. Even though the scale of width has satisfied the ballistic transport condition, it has been become a considerable factor in governing the transport behavior in metal atomic contacts. It has been shown, wider atomic wires allow much current to pass through. The origin has been related to the fact that interfaces between electrodes and atomic wire have a highlight role in determining the number of transmission channels: wider connections let more available states for electrons and enhance the transmission probability. Consistency of calculated equilibrium conductance for copper [001] rod with experimental data has predicted the existence of wide interfaces in the atomic wire structure.

To emulate the tension of electrodes during fabrication process by STM technique, the non-mirrored electrodes have been modeled by shifting electrodes against each other. Comparing electron transport results to those of mirrored electrodes has confirmed quite *negligible influence of electrodes mirroring*. Since one of the fundamental assumptions in transport calculations was to keep electrodes within distance longer than the interaction length, their mirrored or non-mirrored facing would suggest equivalent results for electron transport.

In addition to geometrical components, the temperature effect has been investigated. An *insignificant effect of temperature* has been expected on the electron transport due to the ignored role of the electron-phonon interaction. The reason justifying this assumption has been associated to the scale of modeled geometries, where the length scale characteristics of system have been much small to let the transport regime to be influenced by inelastic scattering due to the temperature.

In spite of the observed *non-linear current-voltage characteristic* of atomic contacts reported in experimental studies, linear behavior has been obtained in most cases, excluding current-voltage curves of gold [110] rods which have shown small deviation in high bias voltages. Extensive discussion has been presented to interpret the non-linearity from various studies, and the common reasons have been related to the pres-

ence of impurities over measurements. Therefore, a linear current-voltage curve is expected for defect-free structures, and the non-linearity of current in gold rods has been explained based on the tight-binding model, which has employed the Slater-Koster parameterization fitted against gold bulk structure calculations. This idea has been justified by comparing the charge distribution along the atomic wires at both equilibrium and non-equilibrium states. Minor charge transfer at biased gold rod has been seen, which was able to modify the linear current-voltage curve. In contrary, the charge neutrality of biased copper rod has ensured the linear characteristic. The common feature of almost all results has been the *better electron transport of copper rather than gold atomic contacts*, by introducing higher value of conductance.

To shed light on the conduction process and make a useful interpretation for experimental phenomena, **conduction channels** and their decomposition have been calculated in Chap. 6 by considering copper and gold single point contacts with [001] and [111] characters.

The energy dependent transmission of [001] bipyramidal shape contacts has proved the presence of *three conduction channels* with a twofold degeneracy for both copper and gold. Turning the electrodes orientation into [111] has destroyed the degeneracy by shifting down the third channel. Consequently, it has reduced the number of mainly transmitted channels to two. The different behavior, which has been also repeated in presence of external bias voltage, has been associated to the difference of *geometric symmetry* as a certain factor in determining the respective position of single atom and consequently varying the participated density of states.

One step forward has been taken by classifying each conduction channel according to the *angular momentum contribution* of single atom contact. In both copper and gold contacts of [001] character, s and p_z orbitals, and faintly d_{z^2} state have captured the main contribution of the first channel. Note that, the z-axis has been supposed to be the transport direction. Meanwhile, the contribution of $p_x, p_y, d_{xz}, d_{yz}, d_{xy}$, and $d_{x^2-y^2}$ states in the first channel was negligible, but rather remarkable in constructing the second and the third degenerate channels. In case of [111] contacts, the role of s and p_z states has been more pronounced in the first and the second channels. In addition, p_x and p_y orbitals have come into play. Transmission eigenchannels of copper and gold contacts have behaved similar generally, resulting to classify them as the *sp*-like metals.

Unlike many previous investigations, the present study has involved more electronic transport properties of copper and gold atomic-scale contacts, as well as more geometrical factors governing the conduction mechanism and new analysis of eigenchannels decomposition to the atomic orbitals. Consequently, some new features, such as conductance oscillation in biased atomic wire, or orbital contributions in conductance of single point contacts, were obtained. Great agreement of the calculated electron transport characteristics (e.g., equilibrium conductance, degenerate channels, and linear

current-voltage curves of single point contacts) with available experimental and theoretical results has found as another success of the simulation tool used for the first time for metals.

7.2. Suggestions for future works

A number of open issues that have not been addressed in this dissertation demand further researches. In this regard, some suggestions are proposed as follows:

- It has been assumed, atomic distances were equal to experimental data measured for bulk structures. The more reasonable value of atomic distance could be achieved within geometry optimizing calculations. The attempt to optimize the geometry through density functional tight-binding method was not successful. Therefore, a molecular dynamic technique is suggested to handle the problem. In addition, analyzing the bond strength in atomic-sized contacts and comparing to the bulk metallic bond is worthwhile.

- To refine the transport results, it would be constructive to consider the electron-phonon interaction.

- It would be of interest to study the influence of defects in atomic contacts by overcoming restrictions in the used tight-binding model.

- Newer experiments have shown the impressive conductivity of carbon nanotubes, graphene, and organic molecules making them promising materials that could be one day replaced copper as primary interconnect material. Hence, it would be beneficial to perform the presented calculations in these materials (e.g., molecular wires bridging metal contacts or carbon nanotubes as electrodes).

Schlussfolgerungen und Perspektiven

Schlussfolgerungen

Entsprechend der Diskussion in Kap. 2 findet der Elektronentransport auf atomarer Skala im ballistischen Transport-Regime statt. Um die quantenmechanischen Aspekte berücksichtigen zu können, sind neue Simulationswerkzeuge erforderlich. Unter den verschiedenen Techniken wurde das *Nicht-Gleichgewichts-Green-Funktionen-Dichtefunktional-Tight-Binding-Modell*, das im gDFTB-Code implementiert ist, für die Transportberechnungen in *atomaren Kupfer- und Goldkontakten* ausgewählt. Dieser Formalismus überbrückt die Lücke zwischen empirischen Tight-Binding-Methoden und ab-initio-Methoden. Darüber hinaus erlaubt die Methode der Nicht-Gleichgewichts-Green-Funktionen auch, den *Elektronentransport in Bauelementen bei angelegter Spannung* zu beschreiben, was in vorangegangenen einfachen Formalismen nicht möglich war. Die Theorie zur Berechnung der elektronischen Transporteigenschaften ausgehend von der Landauer Theorie wird ausführlich dargestellt.

Die Modellierung der geometrischen Struktur beruht auf jüngsten experimentellen Beobachtungen, die zeigen, dass die gefertigten atomaren Drähte kristallin und defektfrei sind, in drei Orientierungen auftreten können und die kleinsten Kontakte aus einem Atom bestehen, angeordnet in der Verlängerung der [100]- bzw. [111]- Richtungen. Das Modell des beidseitig kontaktierten Leiters besteht aus einer Anordnung von zwei halbunendlichen Elektroden und einem atomaren Draht oder Ein-Atom-Kontakt zwischen diesen. Um eine realitätsnahe Simulation zu ermöglichen, wird ein thermodynamisches Gleichgewichtspotential für die halbunendlichen Elektroden angenommen und der Abstand zu den Elektroden durch Einfügen einiger weiterer Atomlagen hinreichend groß gehalten, um Wechselwirkungen zwischen Punktkontakt und Elektroden zu vermeiden.

Besonderes Augenmerk wurde auf die **Beziehung zwischen der Geometrie atomarer Strukturen und ihren elektronischen Transporteigenschaften** gerichtet. In Kap. 5 wird der Geometrieeinfluss der atomaren Kupfer- und Golddrähte mit den Orientierungen [001] und [110] analysiert.

Die Berechnungen ergeben, dass die *elektronischen Transporteigenschaften* atomarer Drähte einschließlich der totalen Transmission, der Strom-Spannungs-Kennlinien und

der Leitfähigkeit in nur sehr geringem Maße durch die Kristallorientierung, *beeinflusst* werden. Die Strom-Spannungs-Kennlinien beider Orientierungen stimmen insbesondere im Bereich kleiner Bias-Spannungen (d. h. $V_b < 0.2$ V) gut überein.

Der durch das Quanteninterferenz-Phänomen verursachte *even-odd-Effekt* bewirkt Leitfähigkeitsoszillationen, womit eine Längenabhängigkeit des Transports im Draht vorliegt. Es wurde gezeigt, dass die *Leitfähigkeitsoszillationen sowohl in Systemen mit angelegter Spannung* als auch unter Gleichgewichtsbedingungen auftreten. Der *schwache Einfluss der Kristallorientierung und der Länge* ist eine Folge des ballistischen Elektronentransports: solange das ballistische Transportregime gilt, sind auch die Beziehungen zwischen Struktur und Elektronen-Transporteigenschaften unbedeutend.

Die Breite der Struktur hingegen hat auch dann deutlichen Einfluss auf die Leitfähigkeit, wenn die Größenordnung der Breitenabmessungen die ballistische Transportbedingung erfüllt. Sie ist ein wichtiger Faktor bei der Beeinflussung des Transportverhaltens in atomaren Metallkontakten. Es wurde gezeigt, dass breitere atomare Drähte höhere Ströme erlauben. Die Ursache dafür liegt in der herausragenden Rolle der Grenzflächen bei der Festlegung der Transmissionskanäle: breitere Verbindungen haben mehr verfügbare Zustände für Elektronen und erhöhen die Transmissionswahrscheinlichkeit. Die Übereinstimmung der berechneten Gleichgewichtsleitfähigkeit von Kupfer-[001]-Stäbchen mit experimentellen Daten legt die Existenz von breiten Grenzflächen in der experimentellen Drahtstruktur nahe.

Um die Verspannung der Elektroden während des Fertigungsprozesses durch die STM-Technik nachzubilden, wurden nicht -gespiegelte Elektroden durch Verschiebung der Elektroden gegeneinander modelliert. Der Vergleich der Elektronen-Transportergebnisse mit denen von gespiegelten Elektroden hat den *vernachlässigbaren Einfluss der Elektrodenspiegelung* bestätigt. Da eine der grundlegenden Annahmen bei den Transportberechnungen darin besteht, dass der Elektrodenabstand größer als die Wechselwirkungslänge ist, sind gleiche Ergebnisse für den Elektronentransport für den gespiegelten bzw. nicht -gespiegelten Fall naheliegend.

Zusätzlich zu den geometrischen Aspekten wurde der Temperatureinfluss untersucht. Auf Grund der vernachlässigten Elektronen-Phononen Wechselwirkung wurde *keine signifikante Auswirkung der Temperatur* auf den Elektronentransport erwartet. Diese Annahme wird dadurch gerechtfertigt, dass die Dimensionen der modellierten Geometrien zu klein sind, um den Transport durch inelastische Streuungen auf Grund der Temperatur beeinflussen zu können.

Trotz der *nicht-linearen Strom-Spannungs-Beziehung* bei atomaren Kontakten, über die in experimentellen Studien berichtet wird, wurde in den meisten Fällen lineares Verhalten berechnet, ausgenommen die Strom-Spannungs-Kurven von Goldstäbchen [110], die leichte Abweichungen von der Linearität bei hohen Bias-Spannungen zeigen. Eine ausführliche Diskussion zur Interpretation der in verschiedenen Studien beobachteten

Nichtlinearitäten wird vorgestellt und mit Verunreinigungen in Verbindung gebracht. Dementsprechend wird ein linearer Stromverlauf für defektfreie Strukturen erwartet.

Die Nichtlinearität des Stromes in Goldstäbchen wurde mit Hilfe eines Tight-Binding-Modell erklärt, welches die Slater-Koster Parametrierung, angepasst an Gold-Bulk-Strukturberechnungen, verwendet. Diese Annahme wird durch den Vergleich der Ladungsverteilung entlang des atomaren Drahtes im Gleichgewichts- und Nichtgleichgewichtszustand gerechtfertigt. Geringer Ladungstransfer bei Goldstäbchen mit angelegter Spannung wurde beobachtet, was ausreichte, um die lineare Strom-Spannungs-Beziehung zu modifizieren. Im Gegensatz dazu sichert die Ladungsneutralität von Kupferstäbchen unter Spannung die lineare Kennlinie. Eine allgemeine Eigenschaft fast aller Ergebnisse sind die *besseren Transporteigenschaften von Kupfer- gegenüber Goldkontakten* durch höhere Werte der Leitfähigkeit.

Um den Leitungsprozess genauer zu untersuchen und eine verwertbare Interpretation der experimentellen Phänomene machen zu können, wurden in Kap. 6 **Leitungskanäle** und ihre Aufspaltung für Kupfer- und Gold-Ein-Atom-Kontakte mit [001]- und [111]-Charakter berechnet.

Die energieabhängige Transmission bei [100]-bi-pyramidalen Kontakten belegt das Vorhandensein von *drei Leitungskanälen* mit doppelter Entartung für Kupfer und für Gold. Eine Drehung der Elektroden-Orientierung in [111] Richtung zerstört die Entartung durch die Verschiebung des dritten Kanals. Infolge dessen besitzt diese Struktur eine auf zwei reduzierte Zahl von Hauptübertragungskanälen. Diese Unterschiede im Verhalten, die sich auch bei angelegter Bias-Spannung zeigen, werden mit der geänderten *geometrischen Symmetrie* als entscheidenden Faktor bei der Bestimmung der entsprechenden Position des Einzelatoms und damit auch unterschiedlichen am Transport teilhabenden Zustandsdichten in Verbindung gebracht.

Ein wesentlicher Schritt konnte bei der Leitungskanal-Klassifizierung hinsichtlich des Drehimpulsbeitrags des Ein-Atom-Kontakts getan werden. Sowohl in Kupfer- als auch in Goldkontakten mit [001]-Charakter stellen s und p_z Orbitale und schwache d_{z^2} Zustände den Hauptbeitrag des ersten Kanals dar. Zu beachten ist, dass die z-Achse als Transportrichtung angenommen wird. Während der Beitrag der $p_x, p_y, d_{xz}, d_{yz}, d_{xy}$, und $d_{x^2-y^2}$ Zustände im ersten Kanal vernachlässigbar ist, ist er bei der Zusammensetzung des zweiten und dritten entarteten Kanals umso wichtiger. Im Falle des [111]-Kontakts war die Rolle der s und p_z Zustände im ersten und zweiten Kanal deutlicher ausgeprägt. Zusätzlich kommen hier die p_x und p_y Orbitale ins Spiel. Die Transmissions-Eigenkanäle von Kupfer und Goldkontakten verhalten sich prinzipiell ähnlich, was zu ihrer Klassifizierung als sp-Metalle führt.

Im Vergleich zu vorangegangenen Untersuchungen enthält die vorliegende Arbeit deutlich weitergehendere Untersuchungen zu elektronischen Transporteigenschaften von atomaren Kupfer- und Goldkontakten. Zusätzlich werden geometrische Faktoren

berücksichtigt, die den Leitungsmechanismus beeinflussen. Die Aufspaltung der Eigenkanäle in Atomorbitale stellt eine neue Analyseform dar. Folglich wurden neue Ergebnisse erhalten, wie die Leitfähigkeitsoszillationen in unter Spannung stehenden atomaren Drähten oder auch die orbitalen Anteile an der Leitfähigkeit von Ein-Atom-Kontakten. Die gute Übereinstimmung der berechneten elektronischen Transporteigenschaften mit den wenigen bisher verfügbaren experimentellen und theoretischen Daten spricht für die Qualität des genutzten Simulationswerkzeugs bei seiner erstmaligen Anwendung für Metalle.

Vorschläge für zukünftige Arbeiten

Eine Reihe von offenen Fragen, die in dieser Dissertation nicht behandelt werden konnten, erfordern weitere Untersuchungen, die im Folgenden kurz skizziert werden:

- Es ist angenommen worden, dass die atomaren Abstände denen entsprechen, die experimentell für Bulk-Materialien bestimmt wurden. Bessere Werte können durch Geometrieoptimierungsrechnungen erhalten werden. Der Versuch, die Geometrie mittels der Dichtefunktional-Tight-Binding-Methode zu optimieren, war nicht erfolgreich. Deshalb werden zur Lösung des Problems Molekular-Dynamik-Simulationen vorgeschlagen. Erstrebenswert wäre auch, die Bindungskräfte der Kontaktstrukturen mit denen im Bulk-Material zu vergleichen.

- Zur Verbesserung der Transport-Ergebnisse wäre es sinnvoll, die Elektronen-Phononen-Wechselwirkungen zu berücksichtigen.

- Interessant wäre es weiterhin, den Einfluss von Defekten in atomaren Kontakten zu untersuchen, wobei die Einschränkungen des Tight-Binding-Modells überwunden werden müssen.

- Neuere Experimente haben die beeindruckende Leitfähigkeit von CNTs, Graphen und organischen Molekülen gezeigt, die sie zu aussichtsreichen Materialien machen, um zukünftig Kupfer als primäres Leitbahnmaterial zu ersetzen. Deshalb wäre es vorteilhaft, die vorgestellten Berechnungen auch für diese Materialien durchzuführen (z. B. Molekulardrähte zwischen Metallkontakten oder CNTs als Elektroden).

Appendix A.

Application of gDFTB

It has been shown that the gDFTB method provides a realistic quantitative description of elastic and inelastic (e.g., if electron-phonon scattering is considered) charge transport through the molecular-scale devices. One of the gDFTB applications could be the description of tunneling through molecules in between metal electrodes. A particular example is a donor-acceptor-type molecule, TTF-EDT-BQD, bridged to the Au [110] leads in a three-terminal device used as a field effect transistor [36]. In other work, transport properties of silicon nanowire based nanoMOSFET have been investigated using gDFTB, where the nanowire extends along the [110] direction while the section has a rhomboid shape [39].
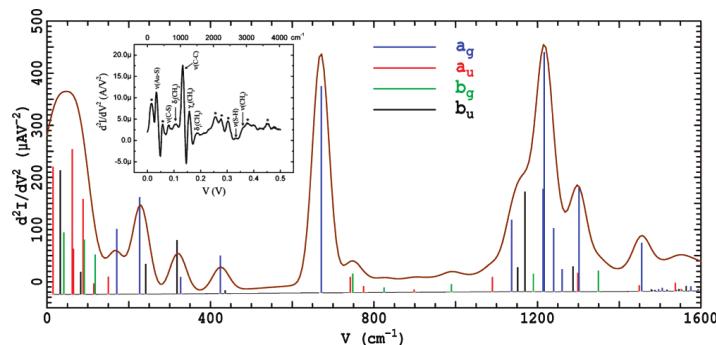
Figure A.1.: Low-resolution and high-resolution IETS of octanedithiol chemisorbed on the gold electrodes. The inset is the observed IETS of WANG et al. [122] for comparison [123].

Successful application of the gDFTB method has also been demonstrated for interpretation and assignment of the experimental *inelastic electron tunneling spectroscopy* (IETS) results and the identification of the role of *molecular symmetric* in determining conductance, in which the spectrum of octanedithiol on gold [111] has been calculated, as shown in Fig. A.1 [122–124].

A large number of theoretical investigations is devoted to CNTs, due to their broad use in nanoelectronics. Transport properties of CNTs have been investigated both with
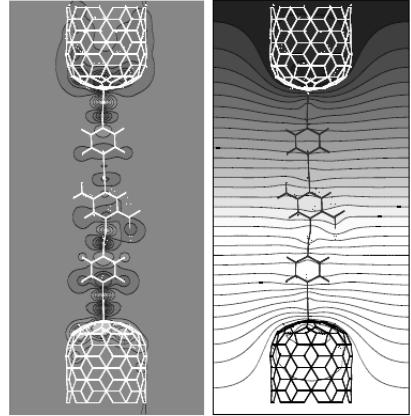
Figure A.2: Self-consistent charge (Left) and potential (Right) for a CNT-wire-CNT system at 1.0 V of bias [38].

empirical tight-binding methods and with ab-initio approaches. Recently, the gDFTB simulator has been applied to a model device, in which a CNT(10,0) is coaxially gated by an ultra-small gate modulating the carrier transmission through the channel. The self-consistent calculation of the gate-induced energy barrier is obtained solving a three-dimensional Poisson equation including a cylindrical gate contact [125].

Another report in this field deals with a system comprising of two CNT tips bridged by a molecular wire (i.e., 2-amino-4-ethynylphenyl-4-ethynylphenyl-5-nitro-1-benzene). This work is relevant to investigate the nature of bistable states mechanism in such molecular wire by the application of a high forward (reverse) bias. Fig. A.2 (Left) shows the self-consistent excess charge accumulated on the system when a bias voltage of 1.0 V is subjected, and corresponding equipotential lines are shown in Fig. A.2 [38].

Bibliography

[1] C. P. Enz, *A Course on Many-Body Theory Applied to Solid-State Physics*, World Scientific Publishing Company, 1993. (Cited on pages 17 and 21.)

[2] A. F. Mayadas and M. Shatzkes, "Electrical-resistivity model for polycrystalline films: the case of arbitrary reflection at external surfaces," *Phys. Rev. B* **1**, p. 1382, 1970. (Cited on pages 17 and 21.)

[3] N. W. Ashcroft and N. D. Mermin, *Solid State Physics*, Brooks Cole, 1976. (Cited on pages 17, 21, 28, 29, 46, and 51.)

[4] R. Landauer, "Spatial variation of currents and fields due to localized scatterers in metallic conduction," *IBM J. Res. Dev.* **32**, p. 306, 1988. (Cited on pages 17, 21, and 35.)

[5] N. Agraït, J. G. Rodrigo, and S. Vieira, "Conductance steps and quantization in atomic-size contacts," *Phys. Rev. B* **47**, p. 12345, 1993. (Cited on pages 18, 22, and 70.)

[6] J. I. Pascual, J. Méndez, J. Gómez-Herrero, A. M. Baró, N. García, and V. T. Binh, "Quantum contact in gold nanostructures by scanning tunneling microscopy," *Phys. Rev. Lett.* **71**, p. 1852, 1993. (Cited on pages 18, 22, and 70.)

[7] J. M. Krans, J. M. van Ruitenbeek, V. V. Fisun, I. K. Yanson, and L. J. de Jongh, "The signature of conductance quantization in metallic point contacts," *Nature* **375**, p. 767, 1995. (Cited on pages 18, 22, and 70.)

[8] A. I. Yanson, G. R. Bollinger, H. E. van den Brom, N. Agraït, and J. M. van Ruitenbeek, "Formation and manipulation of a metallic wire of single gold atoms," *Nature* **395**, p. 783, 1998. (Cited on pages 18, 23, and 91.)

[9] A. I. Mares, A. F. Otte, L. G. Soukiassian, R. H. M. Smit, and J. M. van Ruitenbeek, "Observation of electronic and atomic shell effects in gold nanowires," *Phys. Rev. B* **70**, p. 073401, 2004. (Cited on pages 18, 22, and 70.)

[10] H. Ohnishi, Y. Kondo, and K. Takayanagi, "Quantized conductance through individual rows of suspended gold atoms," *Nature* **395**, p. 780, 1998. (Cited on pages 18, 22, 70, and 71.)

[11] V. Rodrigues, T. Fuhrer, and D. Ugarte, "Signature of atomic structure in the quantum conductance of gold nanowires," *Phys. Rev. Lett.* **85**, p. 4124, 2000. (Cited on pages 18, 22, 70, 71, 92, and 129.)

[12] Y. Takai, T. Kawasaki, Y. Kimura, T. Ikuta, and R. Shimizu, "Dynamic obervation of an atom-sized gold wire by phase electron microscopy," *Phys. Rev. Lett.* **87**, p. 106105, 2001. (Cited on pages 18, 22, and 70.)

[13] J. C. González, V. Rodrigues, J. Bettini, L. G. C. Rego, A. R. Rocha, P. Z. Coura, S. O. Dantas, F. Sato, D. S. Galvão, and D. Ugarte, "Indication of unusual pentagonal structures in atomic-size cu nanowires," *Phys. Rev. Lett.* **93**, p. 126103, 2004. (Cited on pages 18, 22, 71, 84, 92, and 129.)

[14] S. Datta, *Electronic Transport in Mesoscopic Systems*, Cambridge University Press, 1997. (Cited on pages 18, 19, 23, 28, 51, 52, and 56.)

[15] A. I. Yanson, *Atomic chains and electronic shells: quantum mechanisms for the formation of nanowires*. PhD thesis, Universiteit Leiden, 2001. (Cited on pages 18, 23, 92, and 102.)

[16] E. Scheer, N. Agraït, J. C. Cuevas, A. L. Yeyati, B. Ludoph, A. Martín-Rodero, G. R. Bollinger, J. M. van Ruitenbeek, and C. Urbina, "The signature of chemical valence in the electrical conduction through a single-atom contact," *Nature* **394**, p. 154, 1998. (Cited on pages 18, 23, 91, 94, and 102.)

[17] E. Scheer, P. Joyez, D. Esteve, C. Urbina, and M. H. Devoret, "Conduction channel transmissions of atomic-size aluminum contacts," *Phys. Rev. Lett.* **78**, p. 3535, 1997. (Cited on pages 19, 23, 38, 91, and 94.)

[18] A. Bagrets, N. Papanikolaou, and I. Mertig, "Ab initio approach to the ballistic transport through single atoms," *Phys. Rev. B* **73**, p. 045428, 2006. (Cited on pages 19, 23, and 102.)

[19] L. G. C. Rego, A. R. Rocha, V. Rodrigues, and D. Ugarte, "Role of structural evolution in the quantum conductance behavior of gold nanowires during stretching," *Phys. Rev. B* **67**, p. 045412, 2003. (Cited on pages 82, 83, and 102.)

[20] S. K. Nielsen, M. Brandbyge, K. Hansen, K. Stokbro, J. M. van Ruitenbeek, and F. Besenbacher, "Current-voltage curves of atomic-sized transition metal contacts: an explanation of why Au is ohmic and Pt is not," *Phys. Rev. Lett.* **89**, p. 066804, 2002. (Cited on pages 19, 23, 99, and 104.)

[21] E. H. Lieb, "Thomas-fermi and related theories of atoms and molecules," *Rev. Mod. Phys.* **53**, p. 603, 1981. (Cited on pages 19, 23, and 41.)

[22] M. C. Payne, M. P. Teter, D. C. Allan, T. A. Arias, and J. D. Joannopoulos, "Iterative minimization techniques for ab initio total-energy calculations: molecular dynamics and conjugate gradients," *Rev. Mod. Phys.* **64**, p. 1045, 1992. (Cited on pages 41 and 46.)

[23] R. O. Jones and O. Gunnarsson, "The density functional formalism, its applications and prospects," *Rev. Mod. Phys.* **61**, p. 689, 1989. (Cited on pages 41 and 46.)

[24] P. Hohenberg and W. Kohn, "Inhomogeneous electron gas," *Phys. Rev.* **136**, p. B864, 1964. (Cited on page 42.)

[25] W. Kohn and L. J. Sham, "Self-consistent equations including exchange and correlation effects," *Phys. Rev.* **140**, p. A1133, 1965. (Cited on pages 19, 23, 42, and 44.)

[26] A. P. Sutton, M. W. Finnis, D. G. Pettifor, and Y. Ohta, "The tight-binding bond model," *Journal of Physics C: Solid State Physics* **21**, p. 35, 1988. (Cited on pages 19, 23, and 47.)

[27] G. Seifert, D. Porezag, and T. Frauenheim, "Calculations of molecules, clusters, and solids with a simplified LCAO-DFT-LDA scheme," *International Journal of Quantum Chemistry* **58**, p. 185, 1996. (Not cited.)

[28] M. Elstner, D. Porezag, G. Jungnickel, J. Elsner, M. Haugk, T. Frauenheim, S. Suhai, and G. Seifert, "Self-consistent-charge density-functional tight-binding method for simulations of complex materials properties," *Phys. Rev. B* **58**, p. 7260, 1998. (Cited on pages 49 and 63.)

[29] T. Frauenheim, G. Seifert, M. Elstner, T. Niehaus, C. Köhler, M. Amkreutz, M. Sternberg, Z. Hajnal, A. Di Carlo, and S. Suhai, "Atomistic simulations of complex materials: ground-state and excited-state properties," *Journal of Physics: Condensed Matter* **14**, p. 3015, 2002. (Cited on pages 19, 23, 47, and 62.)

[30] A. R. Williams, P. J. Feibelman, and N. D. Lang, "Green's-function methods for electronic-structure calculations," *Phys. Rev. B* **26**, p. 5433, 1982. (Cited on pages 19, 23, and 51.)

[31] F. Guinea, C. Tejedor, F. Flores, and E. Louis, "Effective two-dimensional hamiltonian at surfaces," *Phys. Rev. B* **28**, p. 4397, 1983. (Cited on pages 19, 23, and 52.)

[32] L. V. Keldysh, "Diagram technique for nonequilibrium processes," *Sov. Phys. JETP* **20**, p. 1018, 1965. (Cited on pages 19, 24, and 55.)

[33] C. Caroli, R. Combescot, P. Nozieres, and D. Saint-James, "A direct calculation of the tunnelling current: IV. Electron-phonon interaction effects," *Journal of Physics C: Solid State Physics* **5**, p. 21, 1972. (Cited on pages 55 and 56.)

[34] R. Lake and S. Datta, "Nonequilibrium Green's-function method applied to double-barrier resonant-tunneling diodes," *Phys. Rev. B* **45**, p. 6670, 1992. (Cited on page 55.)

[35] A. Pecchia and A. Di Carlo, "Atomistic theory of transport in organic and inorganic nanostructures," *Reports on Progress in Physics* **67**, p. 1497, 2004. (Cited on pages 19, 24, 39, 55, 59, 60, and 129.)

[36] A. Pecchia, G. Penazzi, L. Salvucci, and A. Di Carlo, "Non-equilibrium Green's functions in density functional tight binding: method and applications," *New Journal of Physics* **10**, p. 065022, 2008. (Cited on pages 19, 24, 62, 65, and 115.)

[37] J. C. Slater and G. F. Koster, "Simplified LCAO method for the periodic potential problem," *Phys. Rev.* **94**, p. 1498, 1954. (Cited on pages 19, 24, 46, and 61.)

[38] A. Di Carlo, A. Pecchia, L. Latessa, T. Frauenheim, and G. Seifert, "Tight-binding DFT for molecular electronics (gdftb)," *Introducing Molecular Electronics* **680**, p. 153, 2005. (Cited on pages 19, 24, 116, and 130.)

[39] F. Sacconi, M. Persson, M. Povolotskyi, L. Latessa, A. Pecchia, A. Gagliardi, A. Balint, T. Fraunheim, and A. Di Carlo, "Electronic and transport properties of silicon nanowires," *Journal of Computational Electronics* **6**, p. 329, 2007. (Cited on pages 19, 24, and 115.)

[40] D. K. Ferry and S. M. Goodnick, *Transport in Nanostructures*, Cambridge University Press, 1997. (Cited on page 28.)

[41] J. J. Thomson, "On the theory of electrical conduction through thin metallic films," *Proc. Camb. Phil. Soc.* **11**, p. 120, 1901. (Cited on page 28.)

[42] K. Fuchs and N. F. Mott, "The conductivity of thin metallic films according to the electron theory of metals," *Mathematical Proceedings of the Cambridge Philosophical Society* **34**, p. 100, 1938. (Cited on page 28.)

[43] E. H. Sondheimer, "The mean free path of electrons in metals," *Advances in Physics* **1**, p. 1, 1952. (Cited on page 28.)

[44] R. B. Dingle, "The electrical conductivity of thin wires," *Royal Society of London Proceedings Series A* **201**, p. 545, 1950. (Cited on page 28.)

[45] D. K. C. McDonald and K. Sarginson, "Size effect variation of the electrical conductivity of metals," *Proceedings of the Royal Society of London. Series A. Mathematical and Physical Sciences* **203**, p. 223, 1950. (Cited on page 28.)

[46] E. Ditlefsen and J. Lothe, "Theory of size effects in electrical conductivity," *Philosophical Magazine* **14**, p. 759, 1966. (Cited on page 28.)

[47] T. Hainzel, *Mesoscopic Electronics in Solid State Nanostructures*, Wiley-VCH, 2003. (Cited on page 28.)

[48] P. A. Mello and N. Kumar, *Quantum Transport in Mesoscopic Systems: Complexity and Statisticacl Flactuations*, Oxford University Press, 2004. (Cited on page 28.)

[49] T. E. Huber, P. Trottman, and J. B. Halpern, "Influence of quantum-mechanical boundary roughness resistance on copper nanolines," *arXiv:0906.3747v1* , 2009. (Cited on page 29.)

[50] P. W. Anderson, "Absence of diffusion in certain random lattices," *Phys. Rev.* **109**, p. 1492, 1958. (Cited on page 30.)

[51] M. del Valle, *Atomistic description of transport at the molecular scale*. PhD thesis, Universidad Autónoma de Madrid, 2006. (Cited on pages 30 and 131.)

[52] L. van Hove, "The occurrence of singularities in the elastic frequency distribution of a crystal," *Phys. Rev.* **89**, p. 1189, 1953. (Cited on page 32.)

[53] M. Büttiker, "Four-terminal phase-coherent conductance," *Phys. Rev. Lett.* **57**, p. 1761, 1986. (Cited on page 37.)

[54] R. H. M. Smit, C. Untiedt, G. Rubio-Bollinger, R. C. Segers, and J. M. van Ruitenbeek, "Observation of a parity oscillation in the conductance of atomic wires," *Phys. Rev. Lett.* **91**, p. 076805, 2003. (Cited on pages 38 and 81.)

[55] C. Møller and M. S. Plesset, "Note on an approximation treatment for many-electron systems," *Phys. Rev.* **46**, p. 618, 1934. (Cited on page 41.)

[56] P. W. Payne, "The Hartree-Fock theory of local regions in molecules," *Journal of the American Chemical Society* **99**, p. 3787, 1977. (Cited on pages 41, 44, and 46.)

[57] C. J. Cramer, *Essentials of Computational Chemistry: Theories and Models*, Wiley, 2004. (Cited on page 41.)

[58] V. H. Crespi, "Relations between global and local topology in multiple nanotube junctions," *Phys. Rev. B* **58**, p. 12671, 1998. (Cited on page 43.)

[59] J. P. Perdew and A. Zunger, "Self-interaction correction to density-functional approximations for many-electron systems," *Phys. Rev. B* **23**, p. 5048, 1981. (Cited on page 44.)

[60] D. M. Ceperley and B. J. Alder, "Ground state of the electron gas by a stochastic method," *Phys. Rev. Lett.* **45**, p. 566, 1980. (Cited on page 44.)

[61] A. E. Mohammed and V. Sahni, "Density-functional-theory gradient expansion approximation for the screened-coulomb exchange energy," *Phys. Rev. B* **29**, p. 3687, 1984. (Cited on page 44.)

[62] D. C. Langreth and J. P. Perdew, "Theory of nonuniform electronic systems: I. Analysis of the gradient approximation and a generalization that works," *Phys. Rev. B* **21**, p. 5469, 1980. (Cited on page 44.)

[63] D. C. Langreth and M. J. Mehl, "Beyond the local-density approximation in calculations of ground-state electronic properties," *Phys. Rev. B* **28**, p. 1809, 1983. (Cited on page 45.)

[64] J. P. Perdew, "Density-functional approximation for the correlation energy of the inhomogeneous electron gas," *Phys. Rev. B* **33**, p. 8822, 1986. (Cited on page 45.)

[65] A. D. Becke, "Density-functional exchange-energy approximation with correct asymptotic behavior," *Phys. Rev. A* **38**, p. 3098, 1988. (Cited on page 45.)

[66] J. P. Perdew and W. Yue, "Accurate and simple density functional for the electronic exchange energy: generalized gradient approximation," *Phys. Rev. B* **33**, p. 8800, 1986. (Cited on page 45.)

[67] J. P. Perdew, J. A. Chevary, S. H. Vosko, K. A. Jackson, M. R. Pederson, D. J. Singh, and C. Fiolhais, "Atoms, molecules, solids, and surfaces: applications of the generalized gradient approximation for exchange and correlation," *Phys. Rev. B* **46**, p. 6671, 1992. (Cited on page 45.)

[68] M. J. Mehl and D. A. Papaconstantopoulos, "Applications of a tight-binding total-energy method for transition and noble metals: elastic constants, vacancies, and surfaces of monatomic metals," *Phys. Rev. B* **54**, p. 4519, 1996. (Cited on page 46.)

[69] P. Löwdin, "A note on the quantum-mechanical perturbation theory," *The Journal of Chemical Physics* **19**, p. 1396, 1951. (Cited on page 46.)

[70] C. M. Goringe, D. R. Bowler, and E. Hernandez, "Tight-binding modelling of materials," *Reports on Progress in Physics* **60**, p. 1447, 1997. (Cited on page 46.)

[71] A. Di Carlo, "Microscopic theory of nanostructured semiconductor devices: beyond the envelope-function approximation," *Semiconductor Science and Technology* **18**, p. R1, 2003. (Cited on page 46.)

[72] M. W. Finnis, A. T. Paxton, M. Methfessel, and M. van Schilfgaarde, "Crystal structures of zirconia from first principles and self-consistent tight binding," *Phys. Rev. Lett.* **81**, p. 5149, 1998. (Cited on page 47.)

[73] S. Fabris, A. T. Paxton, and M. W. Finnis, "Free energy and molecular dynamics calculations for the cubic-tetragonal phase transition in zirconia," *Phys. Rev. B* **63**, p. 094101, 2001. (Cited on page 47.)

[74] X. P. Li, R. W. Nunes, and D. Vanderbilt, "Density-matrix electronic-structure method with linear system-size scaling," *Phys. Rev. B* **47**, p. 10891, 1993. (Cited on page 47.)

[75] J. Kim, F. Mauri, and G. Galli, "Total-energy global optimizations using nonorthogonal localized orbitals," *Phys. Rev. B* **52**, p. 1640, 1995. (Not cited.)

[76] W. Yang, "Direct calculation of electron density in density-functional theory," *Phys. Rev. Lett.* **66**, p. 1438, 1991. (Cited on page 47.)

[77] R. S. Mulliken, "Electronic population analysis on LCAO-MO molecular wave functions," *The Journal of Chemical Physics* **23**, p. 1833, 1955. (Cited on pages 47, 48, and 62.)

[78] T. Frauenheim, G. Seifert, M. Elsterner, Z. Hajnal, G. Jungnickel, D. Porezag, S. Suhai, and R. Scholz, "A self-consistent charge density-functional based tight-binding method for predictive materials simulations in physics, chemistry and biology," *Physica Status Solidi (b)* **217**, p. 41, 2000. (Cited on page 48.)

[79] D. Z. Y. Ting, "Multiband and multidimensional quantum transport," *Microelectronics Journal* **30**, p. 985, 1999. (Cited on page 51.)

[80] S. Mukherjee, "Lippmann-schwinger equation," *Pramana* **16**, p. 81, 1981. (Cited on page 51.)

[81] Y. Meir and N. S. Wingreen, "Landauer formula for the current through an interacting electron region," *Phys. Rev. Lett.* **68**, p. 2512, 1992. (Cited on pages 54 and 56.)

[82] G. D. Mahan, *Many-Particle Physics*, Plenum Publishing, 1995. (Cited on page 55.)

[83] A. L. Fetter and J. D. Walecka, *Quantum Theory of Many-Particle Systems*, Dover Publications, 2003. (Cited on page 55.)

[84] L. P. Kadanoff and G. Baym, *Quantum Statistical Mechanics*, Westview Press, 1994. (Cited on page 56.)

[85] Y. Xue, S. Datta, and M. A. Ratner, "Charge transfer and band lineup in molecular electronic devices: a chemicaland numeriac interpretation," *Chem. Phys* **151**, p. 4292, 2001. (Cited on pages 56 and 58.)

[86] N. D. Lang, "Resistance of atomic wires," *Phys. Rev. B* **52**, p. 5335, 1995. (Not cited.)

[87] J. Taylor, H. Guo, and J. Wang, "Ab initio modeling of quantum transport properties of molecular electronic devices," *Phys. Rev. B* **63**, p. 245407, 2001. (Cited on page 58.)

[88] M. Brandbyge, J. L. Mozos, P. Ordejón, J. Taylor, and K. Stokbro, "Density-functional method for nonequilibrium electron transport," *Phys. Rev. B* **65**, p. 165401, 2002. (Cited on pages 58 and 59.)

[89] A. Di Carlo, "Tight-binding methods for transport and optical properties in realistic nanostructures," *Physica B: Condensed Matter* **314**, p. 211, 2002. (Cited on page 61.)

[90] B. Larade and A. M. Bratkovsky, "Current rectification by simple molecular quantum dots: an ab initio study," *Phys. Rev. B* **68**, p. 235305, 2003. (Not cited.)

[91] E. Louis, J. A. Vergés, J. J. Palacios, A. J. Pérez-Jiménez, and E. SanFabián, "Implementing the Keldysh formalism into ab initio methods for the calculation of quantum transport: application to metallic nanocontacts," *Phys. Rev. B* **67**, p. 155321, 2003. (Cited on page 58.)

[92] R. Zeller, J. Deutz, and P. H. Dederichs, "Application of complex energy integration to selfconsistent electronic structure calculations," *Solid State Communications* **44**, p. 993, 1982. (Cited on page 58.)

[93] K. Wildberger, P. Lang, R. Zeller, and P. H. Dederichs, "Fermi-Dirac distribution in ab initio Green's-function calculations," *Phys. Rev. B* **52**, p. 11502, 1995. (Cited on page 59.)

[94] A. Pecchia, L. Latessa, A. Di Carlo, P. Lugli, and T. Niehaus, "Electronic transport properties of molecular devices," *Physica E: Low-dimensional Systems and Nanostructures* **19**, p. 139, 2003. (Cited on page 61.)

[95] G. Seifert, "Tight-binding density functional theory: an approximate kohn-sham DFT scheme," *The Journal of Physical Chemistry A* **111**, p. 5609, 2007. (Cited on page 62.)

[96] Q. Han and F. Lin, *Elliptic Partial Differential Equations*, AMS Bookstore, 2000. (Cited on page 63.)

[97] F. Jona, X. Z. Ji, and P. M. Marcus, "Hexagonal close-packed copper: theory and experiment," *Phys. Rev. B* **68**, p. 172101, 2003. (Cited on page 64.)

[98] P. Koskinen, H. Hakkinen, G. Seifert, S. Sanna, T. Frauenheim, and M. Moseler, "Density-functional based tight-binding study of small gold clusters," *New Journal of Physics* **8**, p. 9, 2006. (Cited on page 64.)

[99] A. Marini, G. Onida, and R. del Sole, "Quasiparticle electronic structure of copper in the *GW* approximation," *Phys. Rev. Lett.* **88**, p. 016403, 2001. (Cited on page 68.)

[100] W. Zhang, S. H. Brongersma, Z. Li, D. Li, O. Richard, and K. Maex, "Analysis of the size effect in electroplated fine copper wires and a realistic assessment to model copper resistivity," *J. Appl. Phys.* **101**, p. 063703, 2007. (Cited on page 73.)

[101] M. Czerner, A. Bagrets, V. S. Stepanyuk, A. L. Klavsyuk, and I. Mertig, "Parity oscillation and relaxation in monatomic copper wires," *Phys. Rev. B* **74**, p. 115108, 2006. (Cited on page 80.)

[102] N. D. Lang, "Anomalous dependence of resistance on length in atomic wires," *Phys. Rev. Lett.* **79**, p. 1357, 1997. (Cited on page 81.)

[103] P. Havu, T. Torsti, M. J. Puska, and R. M. Nieminen, "Conductance oscillations in metallic nanocontacts," *Phys. Rev. B* **66**, p. 075401, 2002. (Not cited.)

[104] Y. Asai and H. Fukuyama, "Theory of length-dependent conductance in one-dimensional chains," *Phys. Rev. B* **72**, p. 085431, 2005. (Not cited.)

[105] Y. Xu, X. Shi, Z. Zeng, Z. Y. Zeng, and B. Li, "Conductance oscillation and quantization in monatomic Al wires," *Journal of Physics: Condensed Matter* **19**, p. 056010, 2007. (Cited on page 81.)

[106] D. Cheng, W. Y. Kim, S. K. Min, T. Nautiyal, and K. S. Kim, "Magic structures and quantum conductance of [110] silver nanowires," *Phys. Rev. Lett.* **96**, p. 096104, 2006. (Cited on page 83.)

[107] V. Rodrigues, J. Bettini, A. R. Rocha, L. G. C. Rego, and D. Ugarte, "Quantum conductance in silver nanowires: Correlation between atomic structure and transport properties," *Phys. Rev. B* **65**, p. 153402, 2002. (Cited on page 83.)

[108] J. I. Pascual, J. Méndez, J. Gómez-Herrero, A. M. Barø, N. Garcia, U. Landman, W. D. Luedtke, E. N. Bogachek, and H. P. Cheng, "Properties of metallic nanowires: from conductance quantization to localization," *Science* **267**, p. 1793, 1995. (Cited on page 86.)

[109] J. L. Costa-Krämer, N. García, P. García-Mochales, P. A. Serena, M. I. Marqués, and A. Correia, "Conductance quantization in nanowires formed between micro and macroscopic metallic electrodes," *Phys. Rev. B* **55**, p. 5416, 1997. (Cited on page 86.)

[110] H. Yasuda and A. Sakai, "Conductance of atomic-scale gold contacts under high-bias voltages," *Phys. Rev. B* **56**, p. 1069, 1997. (Not cited.)

[111] K. Hansen, S. K. Nielsen, M. Brandbyge, E. Lægsgaard, I. Stensgaard, and F. Besenbacher, "Current-voltage curves of gold quantum point contacts revisited," *Applied Physics Letters* **77**, p. 708, 2000. (Cited on page 86.)

[112] M. Yoshida, Y. Oshima, and K. Takayanagi, "Nonlinear current-voltage curves of gold quantum point contacts," *Applied Physics Letters* **87**, p. 103104, 2005. (Cited on page 87.)

[113] H. Mehrez, A. Wlasenko, B. Larade, J. Taylor, P. Grütter, and H. Guo, "I-V characteristics and differential conductance fluctuations of Au nanowires," *Phys. Rev. B* **65**, p. 195419, 2002. (Cited on page 87.)

[114] J. Moreland and J. W. Ekin, "Electron tunneling experiments using Nb-Sn break junctions," *Journal of Applied Physics* **58**, p. 3888, 1985. (Cited on page 92.)

[115] J. C. Cuevas, A. L. Yeyati, and A. Martín-Rodero, "Microscopic origin of conducting channels in metallic atomic-size contacts," *Phys. Rev. Lett.* **80**, p. 1066, 1998. (Cited on pages 94 and 102.)

[116] N. Agraït, A. L. Yeyati, and J. M. van Ruitenbeek, "Quantum properties of atomic-sized conductors," *Physics Reports* **377**, p. 81, 2003. (Cited on page 94.)

[117] A. Bagrets, N. Papanikolaou, and I. Mertig, "Conduction eigenchannels of atomic-sized contacts: ab initio KKR Green's function formalism," *Phys. Rev. B* **75**, p. 235448, 2007. (Cited on page 94.)

[118] M. Brandbyge, N. Kobayashi, and M. Tsukada, "Conduction channels at finite bias in single-atom gold contacts," *Phys. Rev. B* **60**, p. 17064, 1999. (Cited on page 99.)

[119] O. Lopez-Acevedo, D. Koudela, and H. Häkkinen, "Conductance through atomic point contacts between fcc(100) electrodes of gold," *European Physical Journal B* **66**, p. 497, 2008. (Cited on page 99.)

[120] B. Ludoph and J. M. van Ruitenbeek, "Conductance fluctuations as a tool for investigating the quantum modes in atomic-size metallic contacts," *Phys. Rev. B* **61**, p. 2273, 2000. (Cited on page 102.)

[121] D. J. Bakker, Y. Noat, A. I. Yanson, and J. M. van Ruitenbeek, "Effect of disorder on the conductance of a Cu atomic point contact," *Phys. Rev. B* **65**, p. 235416, 2002. (Cited on page 102.)

[122] W. Wang, T. Lee, I. Kretzschmar, and M. A. Reed, "Inelastic electron tunneling spectroscopy of an alkanedithiol self-assembled monolayer," *Nano Letters* **4**, p. 643, 2004. (Cited on page 115.)

[123] G. C. Solomon, A. Gagliardi, A. Pecchia, T. Frauenheim, A. Di Carlo, J. R. Reimers, and N. S. Hush, "Understanding the inelastic electron-tunneling spectra of alkanedithiols on gold," *The Journal of Chemical Physics* **124**, p. 094704, 2006. (Cited on pages 115 and 130.)

[124] J. G. Kushmerick, J. Lazorcik, C. H. Patterson, R. Shashidhar, D. S. Seferos, and G. C. Bazan, "Vibronic contributions to charge transport across molecular junctions," *Nano Letters* **4**, p. 639, 2004. (Cited on page 115.)

[125] L. Latessa, A. Pecchia, A. Di Carlo, and P. Lugli, "Quantum capacitance effects in carbon nanotube field-effect devices," *Journal of Computational Electronics* **4**, p. 51, 2005. (Cited on page 116.)

List of Figures

List of Tables

Versicherung

Hiermit versichere ich, dass ich die vorliegende Arbeit ohne unzulässige Hilfe Dritter und ohne Benutzung anderer als der angegebenen Hilfsmittel angefertigt habe; die aus fremden Quellen direkt oder indirekt übernommenen Gedanken sind als solche kenntlich gemacht.

Bei der Auswahl und Auswertung des Materials sowie bei der Herstellung des Manuskripts habe ich Unterstützungsleistungen von folgenden Personen erhalten:

– keine –

Weitere Personen waren an der Abfassung der vorliegenden Arbeit nicht beteiligt. Die Hilfe eines Promotionsberaters habe ich nicht in Anspruch genommen. Weitere Personen haben von mir keine geldwerten Leistungen für Arbeiten erhalten, die im Zusammenhang mit dem Inhalt der vorgelegten Dissertation stehen.

Die Arbeit wurde bisher weder im Inland noch im Ausland in gleicher oder ähnlicher Form einer anderen Prüfungsbehörde vorgelegt.

Chemnitz, 22.04.2010   Saeideh Mohammadzadeh

Theses

of the dissertation

Electronic Transport Properties of Copper and Gold at Atomic Scale

for attainment of the title **Dr.-Ing.** at Chemnitz University of Technology,

Faculty for Electrical Engineering and Information Technology,

presented by M.Sc. Saeideh Mohammadzadeh

Chemnitz, April 22, 2010

1. The present work investigates the role of geometric features in electronic transport properties of copper as a less-studied metal and gold by modeling the structures based on the HRTEM observations predicting three possible configurations of [001], [110], and [111] characters. Atomic wires in [001] and [110] elongation directions and single point contacts with [001] and [111] electrodes as two-terminal systems are proposed.

2. New simulation tools are required to treat appropriately the quantum mechanical aspects of considered systems. Among several techniques, the non-equilibrium Green's function density functional tight-binding model is preferred to follow the purposes in the present study. This technique as a bridge between empirical and fully ab-initio is found to be a suitable candidate to manage the huge number of carriers in copper or gold.

3. The non-equilibrium Green's function formalism allows studying the electronic transport properties for biased cases in addition to the zero bias limitation.

4. The geometric structures are ideal with atomic distances borrowed from experiment, and geometry relaxation is not performed by the density functional tight-binding model, since this technique does not include the states set to the f orbitals.

5. The influence of atomic wire orientation on the conduction in both cases of copper and gold is very weak in the vicinity of small bias voltages, where the current-voltage curves of [001] and [110] elongation directions are coincident.

6. The current-voltage characteristics calculated for various wire lengths in [001] direction behave similar due to the secured ballistic transport regime.

7. The conductance oscillates in terms of length, which grows by adding atomic layers along the [001] direction. The conductance oscillation associated to the quantum interference of propagating waves is named the even-odd effect. The odd number atomic faces show greater conductance rather than even layers due to the higher transmission probability. The even-odd effect is appeared at both equilibrium and non-equilibrium conditions.

8. A perfect oscillation of conductance expected in an ideal atomic chain is not supported by the proposed geometric structures consisting wider cross-section than one-atom-thick.

9. The width of the conductor sandwiched between electrodes is found to be the main factor governing the conduction process by determining the number of transmission channels at the junctions.

10. Coincidence of equilibrium conductance with experimental data in copper atomic wire with wider interface layers suggests more detailed geometric characteristics, which are not observed in experimental study.

11. The non-mirrored electrodes are modeled to mimic the tension of metallic surface during experiments via STM technique. The results reveal quite unimportant influence of the electrodes position with respect to each other.

12. Linear current-voltage characteristics are obtained for copper atomic wires at small bias voltages up to 1.0 V as a result of the defect-free geometry and the charge neutrality assumption. The rather non-linearity of gold current-voltage curves is related to the small charge transfer affecting the current.

13. The transmission eigenchannels calculated for the single point contacts of copper and gold with [001] electrodes show existence of three main channels, where the second and the third channels are degenerate.

14. The first channel as the most contributed conduction channel is mainly composed of s, p_z, and d_{z^2} orbitals, and p_x, p_y, d_{xy}, d_{yz}, d_{xz}, and $d_{x^2-y^2}$ states show zero conduction close to the Fermi level. The twofold degenerate channels are consist of p_x and p_y orbitals, and the portion of the other orbitals are quite worthless.

15. Turning the electrodes orientation from [001] into [111] character destroys the twofold degeneracy by shifting down the third transmission eigenchannel, which reduces the conductance.

16. Two eigenchannels are responsible for the conductance in both copper and gold single point contacts with [111] electrodes. The first conduction channel is combined of s and p_z orbitals, the portion of p_x and p_y orbitals is one order smaller but not zero contribution as obtained in [001] case. The second channel decomposition follows the similar orbital participation as the first conduction channel.

17. Weak dependency of transmission on external bias voltage up to 20 mV and reserving the charge neutrality condition in both copper and gold one atom contacts lead to the linear current-voltage characteristics.

18. In comparison with gold, the higher current-voltage curve and consequently the greater value of conductance are obtained for copper with analogy geometries.

List of Publications

1. S. Mohammadzadeh, R. Streiter, and T. Gessner, *I-V curve, conductance, and potential difference of copper and gold (110) nanowires*, submitted for Journal of Nanoscience and Nanotechnology (2010).

2. S. Mohammadzadeh, R. Streiter, and T. Gessner, *Electronic transport properties of copper atomic wires*, Material Research society (in press).

3. Zh. Zong, S. Mohammadzadeh, Y. Cao, Zh. Qiu, R. Liu, R. Streiter, and T. Gessner, *Electrical resistivity calculations for copper nanointerconnect*, Microelectronic Engineering **87**, 402 (2010). [doi: 10.1016/j.mee.2009.07.012]

4. S. Mohammadzadeh, R. Streiter, and T. Gessner, *Geometry dependent of I-V characteristics of gold atomic-sized contacts*, 9th IEEE Conference on Nanotechnology, IEEE-NANO, 884 (2009). [isbn: 978-1-4244-4832-6]

5. S. Mohammadzadeh, D. Pouladsaz, R. Streiter, T. Gessner, *Electronic transport properties in copper nanowire*, Microelectronic Engineering **85**, 1992 (2008). [doi: 10.1016/j.mee.2008.06.005]